



CrossMark  
click for updates

Cite this: *Energy Environ. Sci.*, 2014, 7, 3223

# Black silicon: fabrication methods, properties and solar energy applications

Xiaogang Liu,<sup>ab</sup> Paul R. Coxon,<sup>c</sup> Marius Peters,<sup>b</sup> Bram Hoex,<sup>b</sup> Jacqueline M. Cole<sup>\*ad</sup> and Derek J. Fray<sup>c</sup>

Black silicon (BSi) represents a very active research area in renewable energy materials. The rise of BSi as a focus of study for its fundamental properties and potentially lucrative practical applications is shown by several recent results ranging from solar cells and light-emitting devices to antibacterial coatings and gas-sensors. In this paper, the common BSi fabrication techniques are first reviewed, including electrochemical HF etching, stain etching, metal-assisted chemical etching, reactive ion etching, laser irradiation and the molten salt Fray-Farthing-Chen-Cambridge (FFC-Cambridge) process. The utilization of BSi as an anti-reflection coating in solar cells is then critically examined and appraised, based upon strategies towards higher efficiency renewable solar energy modules. Methods of incorporating BSi in advanced solar cell architectures and the production of ultra-thin and flexible BSi wafers are also surveyed. Particular attention is given to routes leading to passivated BSi surfaces, which are essential for improving the electrical properties of any devices incorporating BSi, with a special focus on atomic layer deposition of Al<sub>2</sub>O<sub>3</sub>. Finally, three potential research directions worth exploring for practical solar cell applications are highlighted, namely, encapsulation effects, the development of micro-nano dual-scale BSi, and the incorporation of BSi into thin solar cells. It is intended that this paper will serve as a useful introduction to this novel material and its properties, and provide a general overview of recent progress in research currently being undertaken for renewable energy applications.

Received 12th April 2014  
Accepted 1st August 2014

DOI: 10.1039/c4ee01152j

www.rsc.org/ees

## Broader context

The continuous improvement of cost-to-performance ratio for solar cells is essential for the sustained growth of photovoltaic deployment. Reducing silicon wafer thickness is an effective method to decrease the material cost of wafer-based solar cells, the most common type of solar cells available in the market. However, as the wafers become very thin, conventional wet etching methods are no longer applicable for texturing wafer surfaces and reducing the surface reflection of sun light; new methods to develop highly-absorbent textured silicon surfaces are thus required. Black silicon possesses a nanostructured surface layer, which effectively minimizes the reflection of a broadband of light. As a consequence, the silicon wafers appear black, instead of the silver-grey typical of planar silicon wafers. This unique property makes black silicon a promising solution for the anti-reflection coating of silicon solar cells. Black silicon can also be used to produce ultra-thin and flexible wafers and reduce wafer impurity levels, owing to its weak mechanical strength and large and active surface area. Moreover, its applications have been extended to areas, such as H<sub>2</sub> production *via* electrochemically splitting water, lithium ion batteries, and optoelectronic and photonic devices. It is expected that black silicon will play an increasingly important role in energy applications.

## 1 Introduction

Black silicon (BSi) refers to silicon surfaces covered by a layer of nano- or fine micro-structures, which effectively suppresses reflection, while simultaneously enhancing the scattering and absorption of light. As a consequence, the silicon wafers appear

black, instead of the silver-grey typical of planar silicon wafers. BSi possesses many attractive properties, such as low reflectance, a large and chemically active surface area, super-hydrophobicity, and a high luminescence efficiency when surface feature sizes are reduced to a few nanometers. Consequently, BSi has been applied to a wide range of applications,<sup>1–3</sup> such as micro-electro-mechanical systems (MEMS),<sup>4</sup> chemical- and bio-sensors,<sup>5–9</sup> optoelectronic and photonic devices,<sup>10–18</sup> drug delivery,<sup>2,19</sup> lithium-ion batteries,<sup>20–22</sup> H<sub>2</sub> production by photoelectrochemical splitting of water,<sup>23</sup> bactericidal media,<sup>24</sup> and as a “self-cleaning” surface.<sup>25,26</sup> It can also function as a precursor host for the deposition and nano-patterning of other materials to facilitate more versatile applications<sup>27,28</sup> or act as a supporting platform for chemical and physical reactions, such

<sup>a</sup>Cavendish Laboratory, Department of Physics, University of Cambridge, J. J. Thomson Avenue, Cambridge, CB3 0HE, UK. E-mail: jmc61@cam.ac.uk; Fax: +44 (0)1223 373536; Tel: +44 (0)1223 337470

<sup>b</sup>Solar Energy Research Institute of Singapore (SERIS), National University of Singapore, Singapore 117574, Singapore

<sup>c</sup>Department of Materials Science and Metallurgy, University of Cambridge, 27 Charles Babbage Road, Cambridge, CB3 0F3, UK

<sup>d</sup>Argonne National Laboratory, 9700 S Cass Avenue, Argonne, IL 60439, USA



as in desorption-ionization on silicon (DIOS) mass spectroscopy,<sup>29</sup> high speed metal-oxide catalytic growth of carbon nanotubes,<sup>30</sup> and direct-laser writing induced 3D-polymer polymerization.<sup>31</sup>

BSi also features highly in solar cell research, particularly as a highly-absorbent textured front surface. In recent years, the photovoltaic (PV) applications of BSi have been extended into other fields, such as wafer impurity gettering and thin wafer production in a kerfless porous silicon process. To this end, over the past 15 years, many new BSi fabrication techniques have emerged and matured. Important design knowledge of BSi solar cells has been gained and a number of innovative solar cell architectures have been developed with a strong potential to further advance the power conversion efficiency of silicon solar cells at a decreasing cost.<sup>32–36</sup> In parallel, the global photovoltaic industry is experiencing a rapid growth with a global installed capacity of 31.1 GW in 2012 alone and a cumulative installed capacity of 102.2 GW from 2000 to 2012. Additionally, the oversupply of photovoltaic module production capacity to actual global installation of ~150–230% in recent years sends a strong signal for product differentiations and new concepts to improve the cost-to-performance ratios of solar modules.<sup>37</sup>

In this paper, we provide a comprehensive review on the recent progress of BSi research and its application in solar cell technologies. This paper is organized as follows: first, different BSi fabrication techniques are introduced and their pros and cons are critically analyzed. The applications of BSi in solar cells are then examined, summarizing important design knowledge gained through the work of various research groups. Owing to the importance of surface passivation in BSi, we then consider different surface passivation techniques, and present perspectives on three potential research directions on BSi solar cells for the future. It is hoped this paper will systematically organize previous knowledge across the reported literature in an accessible manner and greatly facilitate the new development of BSi research from a photovoltaic perspective.

## 2 Black silicon fabrication techniques

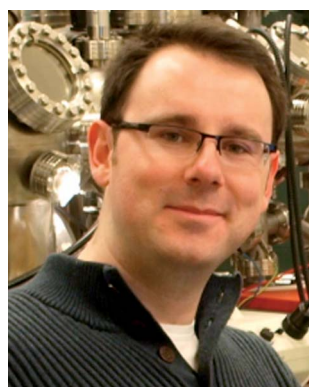
Over recent decades, a range of BSi fabrication processes has been developed. In this section, the major techniques are reviewed. The discussion of electrochemical HF etching and stain etching is relatively brief, since these two techniques are well established and their PV applications have been reviewed



*Xiaogang Liu is a fourth-year PhD student at the University of Cambridge, under the supervision of Dr Jacqueline M. Cole. Xiaogang holds two master degrees in Materials Sciences and Engineering, from the National University of Singapore (NUS) and Massachusetts Institute of Technology (MIT; 2009), respectively. His research focuses on the development of new materials for light harvesting and emission applications.*



*Ian Marius Peters is a research fellow at the Solar Energy Research Institute of Singapore (SERIS) in NUS. At SERIS, he heads the PV simulation and modeling group. He holds a bachelor degree (2006) and a PhD degree (2009) both in Physics from the Albert-Ludwigs University in Freiburg, Germany. Between 2004 and 2011, he worked at the Fraunhofer Institute for Solar Energy Systems (ISE) in Freiburg, Germany and joined NUS in 2011. His research focuses on optics and photonics for solar cells, novel solar cell concepts and PV simulation from fundamentals to systems.*



*Paul Coxon is a postdoctoral research associate in the University of Cambridge. He holds a master degree in Physics (2005) and a PhD degree in nanomaterials (2010) from the University of Newcastle upon Tyne. He worked as Senior Research Associate at the University of East Anglia investigating nanoparticle films for thermoelectrical applications. His current research focuses on electrochemical methods of black silicon production for antireflection coatings in silicon solar cells.*



*Bram Hoex is a Director and Group Leader at SERIS in NUS. He holds a MSc and a PhD degree in Applied Physics from the Eindhoven University of Technology. His research focuses on advanced fabrication and characterization of high-efficiency silicon wafer solar cells. In 2008 he was awarded the Solarworld "Junior Einstein Award" and Leverhulme "Technology Transfer Award".*



elsewhere in the literature.<sup>38–41</sup> Instead, we focus more on the latest developments in the field. More details are given on some recent etching methods, including metal-assisted chemical etching, reactive ion etching, laser irradiation and the Fray-Farthing-Chen-Cambridge (FFC-Cambridge) process (electrochemical reduction of SiO<sub>2</sub> method). However, we will not cover the bottom-up approaches for growing silicon nanostructures, such as the VLS method,<sup>42,43</sup> chemical vapor deposition,<sup>44,45</sup> and the like, owing to their slow growth rate and relatively high costs, which are not feasible for solar cell applications. Although incorporating photolithography and etching masks affords a wide range of periodic micro- and nanostructures,<sup>46</sup> we refrain from detailed discussions for the same reason, only briefly covering their applications where necessary.

## 2.1. Electrochemical etching

Electrochemical HF etching of silicon was first introduced around five decades ago,<sup>47</sup> and has become increasingly popular since the discovery of luminescence from porous silicon,<sup>48–51</sup> serving as a precursor for the production of a new class of silicon nanomaterials.<sup>52–54</sup> During this process, a silicon wafer is tied to the anode of an electrochemical cell, immersed into a solution containing HF, H<sub>2</sub>O and ethanol (Fig. 1). In this solution, HF is responsible for removing silicon oxide produced during the etching reaction by forming a water soluble complex; H<sub>2</sub>O participates in the oxidation reaction, and can be added to control the aqueous concentration of HF, [HF], and the corresponding reaction rate; ethanol is often added to reduce silicon surface tension and improve wettability, allowing the release of H<sub>2</sub> formed during the reaction and the infiltration of HF into the silicon pores.<sup>55</sup>

Applying a voltage bias or current initializes the etching reaction. According to the current density, the etching can be classified into three regions.<sup>57,58</sup> In the low current density

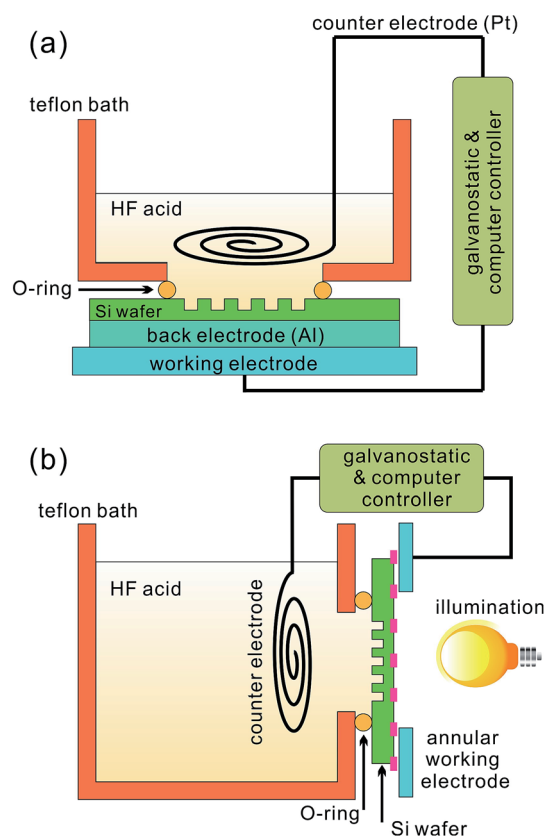


Fig. 1 Typical experimental setups for electrochemical HF etching of: (a) p-Si; and (b) n-Si.<sup>55,56</sup>

region, the etching reaction is limited by silicon oxidation, leading to the formation of porous silicon. In the high current density region, a large number of holes are injected into the bulk material and diffuse over the entire surface of the wafer. In



Jacqueline M. Cole is Head of the Structure & Dynamics group at the Cavendish Laboratory, University of Cambridge, UK. She concurrently works at Argonne National Laboratory, USA, who hosts her Fulbright Award (2013–2014). Jacqueline holds a PhD degree in Chemistry from the University of Durham (1997) and a PhD degree in Physics from the University of Cambridge (2010). She is

primarily engaged in the design and functionalization of new materials for optoelectronic applications, with a specific focus on materials for energy. She has received a number of awards including: the first British Crystallographic Association Chemical Crystallography Prize (2000); the 18th Franco-British Science prize (2006); the Brian Mercer Feasibility Award (2007); and the Royal Society of Chemistry SAC Silver Medal (2009).



Derek Fray is Director of Research and Emeritus Professor of Materials Chemistry in the Department of Materials Science and Metallurgy, University of Cambridge. He has degrees from Imperial College London and has been an Assistant Professor at MIT and a Professor at the University of Leeds. He holds many international awards and was elected as a Fellow of the Royal Academy of Engineering in

1989 and a Fellow of the Royal Society in 2008. His research interests encompass novel methods of materials processing and has spun out several companies.





this case, the etching reaction is limited by the removal of the oxide; consequently, the wafer becomes electrochemically polished. Between these two regions, there exists a transition region, where randomly distributed nano-pillars can be produced without using a mask.<sup>59</sup> The exact current density values defining these three regions depend on the doping types and concentrations of the wafers, [HF], illumination conditions and so forth.<sup>60</sup> For a moderately doped p-Si wafer in 1% HF solution in the dark, the maximum current for porous silicon production amounts to  $\sim 3 \text{ mA cm}^{-2}$ ; electrochemical polishing occurs as the current density exceeds  $\sim 5.5 \text{ mA cm}^{-2}$ .<sup>58</sup>

With a photolithography defined mask, three-dimensional micro- and nano-structures can be fabricated, during which only selected areas are electrochemically polished.<sup>55,59,61</sup> For the sake of BSi, however, our subsequent discussion will only focus on the low current region.

The etching reaction in the low current region is mainly controlled by adjusting the current density, [HF], etching time and illumination. The resulting silicon pore sizes increase as the current density rises, or as [HF] drops. The pore depths propagate as etching time increases. When moderately doped n-Si is used, illumination is often employed, since hole generation is a limiting factor during the etching of this type of wafer in the dark (Fig. 1b).

The resulting pore morphologies also depend on the wafer doping type and dopant concentration. Put simply, for p-Si, the pore size increases with doping concentration, from 1 to 100 nm; for n-Si, it decreases with doping concentration, from 10  $\mu\text{m}$  to 10 nm.<sup>58</sup>

For most typical laboratory-based synthesis methods, the most convenient and flexible control parameters during electrochemical etching are current density and etching time. By applying a constant current, the porosity of a silicon wafer remains the same as its pores grow into the substrate (Fig. 2a). In contrast, changing current density and its related time profile can create structures with gradual variations or step changes in its porosity and refractive index. For example, Striemer and Fauchet continuously varied the etching current during their electrochemical etching from 100 mA to 0 mA over 10 s, and

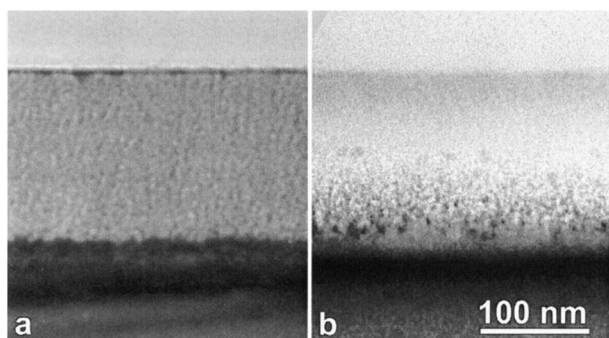


Fig. 2 TEM images of (a) electrochemically and (b) stain etched porous silicon, with a thickness of  $\sim 150 \text{ nm}$ . The porosity is uniform in the electrochemical case, but possesses a gradual transition in the stain etched case.<sup>63</sup> Reproduced by permission of the Electrochemical Society.

produced a gradual change of porosity from  $\sim 99\%$  to  $\sim 33\%$  (Fig. 3). Their porous layer demonstrated better optical performance than the homogeneous porous silicon film, with a weighted reflectance of only 3.7% at a thickness of 107 nm (Fig. 4).<sup>62</sup> In contrast, the homogenous porous silicon often requires a thickness of several  $\mu\text{m}$  to achieve the same level of reflectance. A thick porous layer, however, is incompatible with a thin film solar cell bearing a junction depth of only  $\sim 350 \text{ nm}$ ,<sup>62</sup> since this layer itself may absorb, and thence waste, a substantial amount of light.

By employing a similar strategy, Ma and co-workers used electrochemical etching to form a multi-layer porous silicon structure with gradual change of porosity and refractive index from air to silicon bulk, with a total thickness of  $4.1 \mu\text{m}$ .<sup>64</sup> The resulting structure effectively suppresses the light reflectance to less than 5% in both the visible and IR regions (from  $\sim 350 \text{ nm}$  to  $\sim 3.3 \mu\text{m}$ ). Ariza-Flores *et al.* fabricated 235 nm-thick porous

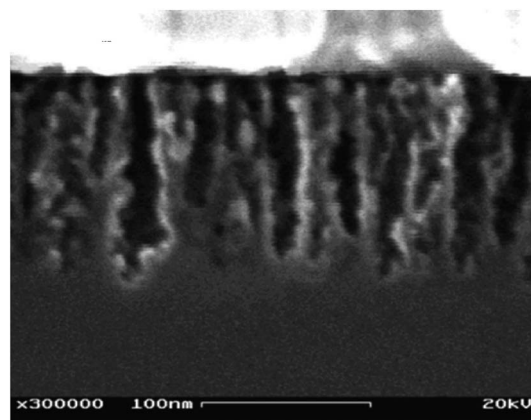


Fig. 3 SEM image of a gradient index porous silicon, with a thickness of  $\sim 100 \text{ nm}$ . Reproduced with permission from ref. 62. Copyright 2002, AIP Publishing LLC.

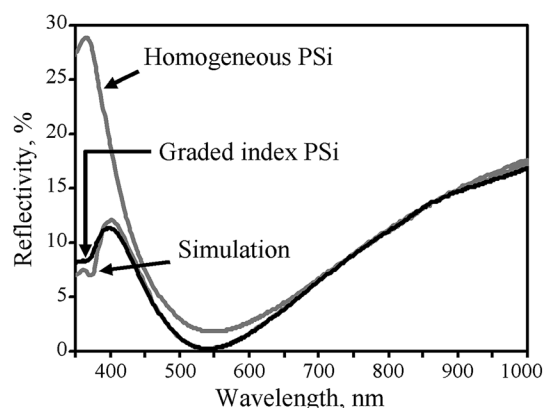


Fig. 4 Reflectance spectra of a homogenous porous silicon layer (80 nm thick, 75% porosity) and a gradient index porous silicon layer (100 nm thick). The later spectrum has an excellent match to the simulated reflectance of a porous layer with porosity gradient from 94% to 33%. Reproduced with permission from ref. 62. Copyright 2002, AIP Publishing LLC.





silicon with a gradual porosity change from 92% to 38%, leading to a low weighted average reflectance of 1.3% from 300 to 1100 nm.<sup>65</sup> By considering only the solar spectrum region, Osorio *et al.* also designed a three-layer porous silicon structure with porosity at 89%, 70% and 41% possessing a corresponding thickness of 75 nm, 56 nm and 39 nm, respectively.<sup>66</sup> Its theoretical optical transmittance of 95.7% has been experimentally verified.<sup>66</sup> Note that Osorio *et al.* took into account light absorption in the porous layer and optimized their structure based on the maximum optical transmittance, instead of the minimal reflectance.

Multi-layer porous silicon is composed of layers with different refractive indices. Interference within these layers can be used to create selective reflectance or transmission by making use of the antireflection and the Bragg effects.<sup>67</sup> Consequently, the etched silicon wafers exhibit different colors under white illumination (Fig. 5).<sup>68</sup> Similarly, the reflection properties of the multi-layer structure, the so-called super-lattice, can be altered for a wide range of photonic and optical devices, such as a distributed Bragg reflector,<sup>10,11</sup> Fabry–Perot interference filter,<sup>12</sup> micro-cavity,<sup>13,14</sup> and Rugate filters.<sup>15</sup>

Electrochemical HF etching is low cost, easy to implement, compatible with standard microelectronic fabrication techniques, and allows the creation of porous silicon with a wide range of structures and applications. It can be applied to both crystalline silicon (c-Si) and multicrystalline silicon (mc-Si).<sup>63</sup> While it has been a concern to apply this technique to handle large surface areas, such as are in demand for industrial applications, owing to the required high current,<sup>69</sup> Semiconductor Systems Corporation (SEMSYSCO) has introduced a semi-automated pilot line (SEMSYSCO PoSi), which is able to

handle up to 216 wafers per run.<sup>70</sup> Nevertheless, maintaining a uniform current density over a large surface area is likely to be a challenging task for applying electrochemical HF etching to a large-scale industry process.

## 2.2. Stain etching

Stain etching employs HF and HNO<sub>3</sub> to perform chemical etching of silicon, leading to the formation of porous silicon.<sup>71</sup> H<sub>2</sub>O and/or acetic acid are often added to dilute [HF] and [HNO<sub>3</sub>], while acetic acid also acts as a wetting agent. The etching action of HF–HNO<sub>3</sub> is based on a successive oxidation–followed-by-dissolution process, in which HNO<sub>3</sub> is responsible for injecting holes and oxidizing silicon, and HF for removing the oxide formed.<sup>72</sup>

By controlling the concentration ratio of HF and HNO<sub>3</sub>, or  $C = [\text{HF}]/[\text{HNO}_3]$ , different silicon surface morphologies can be formed.<sup>73–76</sup> In short, when [HF] is high and [HNO<sub>3</sub>] is low, the etching rate is determined by the oxidation rate, and porous silicon is formed in this region for both n- and p-Si.<sup>49,77</sup> In contrast, when [HNO<sub>3</sub>] far exceeds [HF], the etching reaction is limited by the removal of silicon oxide *via* HF. In this high [HNO<sub>3</sub>] region, HF–HNO<sub>3</sub> is often used for silicon surface cleaning and damage removal, or surface polishing.<sup>39,78,79</sup> By properly adjusting  $C$ , one may also texturize mc-Si, when conventional alkaline chemical etching is not suitable, due to its anisotropic nature and the diverse crystal orientations on a mc-Si wafer.<sup>80</sup> Owing to its similarity to electrochemical HF etching (Section 2.1), stain etching is often considered as a localized electrochemical etching process. It bears some similarity to metal-catalyzed chemical etching methods (Section 2.3), since HNO<sub>3</sub> reduction is autocatalytic, due to the formation of an intermediate compound, HNO<sub>2</sub>.<sup>81</sup>

However, in contrast to the other two techniques, stain etching also removes the top surface of silicon at a relatively high rate. This effect impacts in two ways. First, it produces a gradual transition in porosity, *i.e.*, from silicon bulk to 100% porosity (Fig. 2b).<sup>41</sup> Second, there is an upper limit for the thickness of the porous layer produced by stain etching.<sup>77</sup> This is because the pore propagation rate drops as the porous silicon layer becomes thicker, due to the lower diffusion rate of reactants and reaction products within the deep pores. When this rate matches the etching rate at the top surface of the porous layer, the maximum thickness of the porous layer is achieved.<sup>82</sup> While the exact value of this maximum thickness varies according to experimental conditions, 300–400 nm has been reported for p-Si<sup>77</sup> with a boron doping concentration of  $2 \times 10^{15}$  atom per cm<sup>3</sup>. This maximum thickness, however, increases in line with the silicon doping concentration.<sup>77</sup> For example, 700–800 nm has been reported for a boron doping concentration of  $2 \times 10^{16}$  atom per cm<sup>3</sup>, and infinite for  $10^{18}$  atom per cm<sup>3</sup>. This phenomenon can be explained by the presence of a higher number of active structural defects in highly doped silicon, which can easily be attacked by the etchant and thus boost the rate at which pores propagate.

Another important control parameter of stain etching is represented by  $C \times t$ , where  $C = [\text{HF}]/[\text{HNO}_3]$  and  $t$  is the

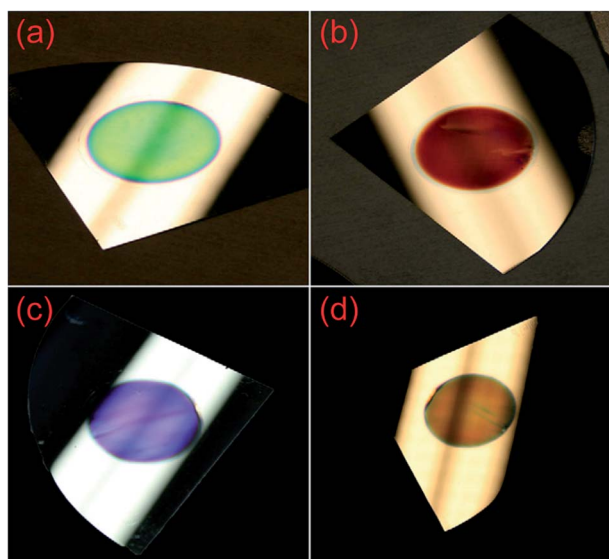


Fig. 5 Multi-layer porous silicon samples under the illumination of a white fluorescent lamp, exhibiting different colors: (a) green; (b) red; (c) purple; and (d) orange. Only a circular area of  $\sim 4 \text{ cm}^2$  has been electrochemically etched for each wafer and displays different colors, while the untreated area reflects white light.<sup>68</sup> Adapted by permission of Elsevier.



etching time. Since stain etching works in the low  $[\text{HNO}_3]$  region and  $\text{HNO}_3$  is a reaction limiting factor, increasing  $[\text{HNO}_3]$  scales up the etching rate. Similarly, extending the etching time affords a thicker porous layer (when the film thickness is less than the maximum achievable thickness). Consequently, a constant  $C \times t$  leads to the formation of a porous silicon layer with an approximately fixed layer thickness; the reflectance of the porous silicon drops, when  $C \times t$  increases.<sup>41</sup> Nevertheless, varying  $t$  changes the wavelength at which the reflectance is at the minimum (Fig. 6);<sup>63</sup> and changing  $C$  has a greater impact on the absolute reflectance value. By tuning these two parameters, one can adjust the effective refractive index of the porous layer from 1.5 to 2.2.<sup>41</sup>

A modified version of stain etching was introduced by Bes-sais *et al.*<sup>83–89</sup> Instead of performing the etching in the solution phase, they used HF and  $\text{HNO}_3$  vapors. It was found that a luminescent white powder made of  $(\text{NH}_4)_2\text{SiF}_6$  is produced when the HF– $\text{HNO}_3$  gas volume ratio is between 2 : 1 and 4 : 1. As this ratio rises above 9 : 1, porous silicon is formed.<sup>87</sup> The resulting structure forms interconnected clusters, containing dot-like silicon particles. In this case, pore propagation is perpendicular to the substrate surface. This feature is similar to that of electrochemical etching, but in contrast to stain etching, which affords curved pore propagation.<sup>83–85</sup> Moreover, the reaction rate of chemical vapor etching is much lower than that of stain etching, causing less damage to other materials, such as metal lines, deposited on the silicon surface. This technique also allows the fabrication of much thicker porous layers, (>100  $\mu\text{m}$ ).<sup>86</sup>

Stain etching is an economic and facile route for scaling up, owing to its wet process character. It is also fast and able to suppress silicon reflectance to below 10% within a short time frame (on the order of 10 s).<sup>63</sup> The resulting surface nano-structures display strong luminescence due to quantum confinement, and can be used for optoelectronic

applications.<sup>49,90</sup> Stain etching also works well on c-Si and mc-Si, and is only slightly grain-dependent.<sup>63</sup> However, it offers less control compared with other techniques, and is not suitable where very thick porous layers are desired. As a result, this technique remains relatively unpopular.

### 2.3. Metal-assisted chemical etching

Silicon can be etched in the presence of HF and an oxidative agent, catalyzed by noble metals, to form micro-/nano-structured surfaces with various morphologies.<sup>91</sup> This technique has been thoroughly reviewed by Huang *et al.* in 2011.<sup>92</sup> Here, we briefly summarize its mechanism and interest from the solar cell perspective, and review recent developments.

In a typical etching process, a silicon substrate is partly covered by noble metal nanoparticles, and immersed in a solution of HF and an oxidative agent.<sup>92–94</sup> For noble metals, gold (Au) and silver (Ag) are the two most popular candidates since they can be deposited onto the surface under vacuum (*i.e.*, *via* thermal evaporation, sputtering and electron beam evaporation) or in solution (*i.e.*, *via* electroless deposition and electrodeposition).<sup>92,94</sup> Vacuum deposition offers a higher degree of control over the metal film morphology, while electroless deposition affords a simpler process and can be adopted when the requirement on silicon surface morphologies is less stringent.<sup>92</sup> Our subsequent discussion will mainly be based on electroless Au or Ag deposition.

During deposition, a compound containing Au or Ag ions, such as  $\text{AgNO}_3$  or  $\text{HAuCl}_4$ , is added to a HF– $\text{H}_2\text{O}_2$  solution. Upon attachment to the silicon substrate, noble metal ions acquire electrons from the silicon valence band and are reduced to form seed nuclei which develop into nanoparticles. Concurrently, these ions inject holes underneath the silicon causing oxidation into  $\text{SiO}$  or  $\text{SiO}_2$ , which are then removed by HF.<sup>92</sup> By the continuous formation of silicon oxide underneath the metal particles and the corresponding removal action by the HF, the metal particles sink into the silicon and create porous

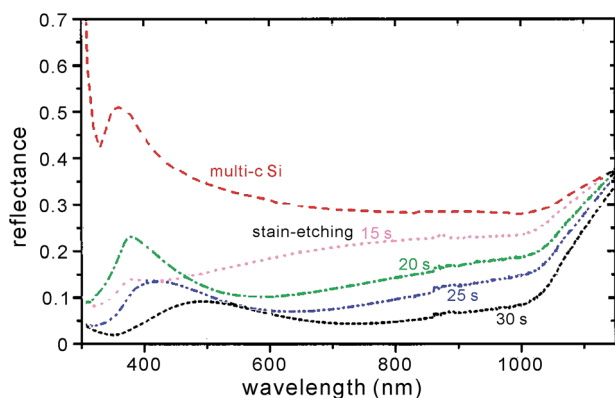


Fig. 6 Reflectance spectra of stain etched porous silicon on a mc-Si wafer. The reflectance over the entire VIS–NIR band is lowered, as the etching time,  $t$ , increases and the porous layer becomes thicker. The AM1.5 weighted reflectance from 300–1000 nm amounts to 32.0% (0 s), 18.9% (15 s), 13.6% (20 s), 9.7% (25 s), and 6.3% (30 s), respectively; the corresponding porous layer thickness is  $\sim 100$  nm (15 s) and  $\sim 150$  nm (30 s), respectively.<sup>63</sup> Reproduced by permission of the Electrochemical Society.

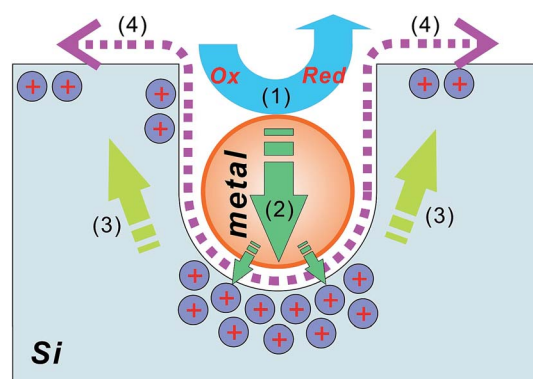


Fig. 7 An illustration of the metal-assisted chemical etch process: (1) the reduction of an oxidative agent (such as  $\text{H}_2\text{O}_2$ ) catalyzed by a noble metal particle; (2) the injection of the holes generated during the reduction reaction, into the silicon substrate, with the highest hole concentration underneath the metal particle; (3) the migration of holes to silicon sidewalls and surfaces; and (4) the removal of oxidized silicon via HF.<sup>92</sup>



structures (Fig. 7).<sup>92</sup> The depth of these pores is proportional to the etching time.<sup>95</sup> Once the desired surface structures are created, the metal nanoparticles are removed by another etchant, such as  $\text{HNO}_3$ , followed by a cleaning process.

Metal catalysis plays a key role during the chemical etching process. Koynov *et al.* showed that without metal catalysis, the etching speed was very low ( $\sim 1 \text{ nm min}^{-1}$ ). In contrast, this speed was greatly increased by the addition of Au;  $\sim 250 \text{ nm}$  high-hillock structures were fabricated within 50–90 s.<sup>96</sup> Consequently, the size and shape of deposited metal particles largely determine the morphologies of the etched surface, since the silicon underneath this metal catalyst is etched much faster. By varying the surface coverage and distance between metal particles, one can create a wide range of surface nanostructures, from BSi layers to nanowires.<sup>96,97</sup>

Several strategies can be employed to produce more sophisticated structures using metal-assisted chemical etching. For example, the etching can be performed *via* a two-step process.<sup>98</sup> During the first step, highly dispersed silver nanoparticles are deposited onto silicon, followed by a long etching step to form deep pores. In the second step, more concentrated silver nanoparticles are employed for a quicker etching in order to increase the porosity in the topmost layer. This two-step process leads to a smoother transition of porosity (and the corresponding refractive index) from air to bulk silicon, affording a lower reflectance compared with single-step etching.<sup>98</sup>

Another strategy to produce gradient refractive indices is to use reactive ion etching (RIE; see Section 2.4) to retouch the nanostructures produced by metal assisted chemical etching. For example, the nanostructures fabricated *via* Ag catalyzed chemical etching are usually columnar, with near vertical side walls and blunt tips [Fig. 8a and b].<sup>99</sup> By applying RIE to such

structures, needle-like structures can be created [Fig. 8c and d], leading to very good anti-reflection results (Fig. 9). Li and co-workers coated silicon wafers with such structures ( $7.1 \mu\text{m}$  in height and 50–150 nm in diameter) causing its reflectance to decrease to less than 2% from 250–1000 nm (Fig. 9).<sup>99</sup>

Furthermore, densely-packed periodic nanostructures can be obtained by applying a mask, which may be defined by interference lithography,<sup>100</sup> colloidal particle deposition,<sup>99</sup> or phase segregation of block-copolymers.<sup>101</sup>

Although metal removal is often performed after the nanostructure formation, it is not always necessary. Recent work by Guo *et al.* made use of the deposited metal to produce a conductive BSi surface.<sup>102</sup> In that work, a dual layer of indium (In) and  $\text{SiO}_x$  was deposited onto a silicon wafer. The deposited In forms islands and the gap between such islands is enlarged *via*  $\text{HNO}_3$  etching when necessary (from tens to more than 100 nm, or 80 nm in the reported case). Using these islands as a mask, Ag was deposited *via* a lift-off process, forming an Ag mesh, instead of individual nanoparticles (Fig. 10). As the Ag catalyzed chemical etching proceeds, the Ag mesh sinks into silicon substrate, in parallel to the nanostructure formation. The resulting structure has a very low reflectance over a broadband (Fig. 11). The weighted reflectance (from 400 to 1000 nm) without any additional antireflection coating was measured at 3.2% and 8.0%, at nanostructure depths of 600 and 200 nm, respectively.<sup>102</sup> In particular, the embedded Ag network effectively minimizes metal shading effects and contributes to the improved reflectance, unlike other exposed metal contacts. While making good contact on nanostructures has been a challenging task, good electrical conductivity ( $\sim 7 \Omega \square^{-1}$ ) has been achieved with an embedded Ag network.<sup>102</sup> Nevertheless, this structural design also introduces an enlarged Si/Ag interface; and the resulting carrier recombination is expected to be high.

In summary, metal-assisted chemical etching is a simple, fast, low cost and versatile process for fabricating a wide range of nanostructures with minimal hardware requirements. The morphologies of the resulting silicon surfaces can be controlled

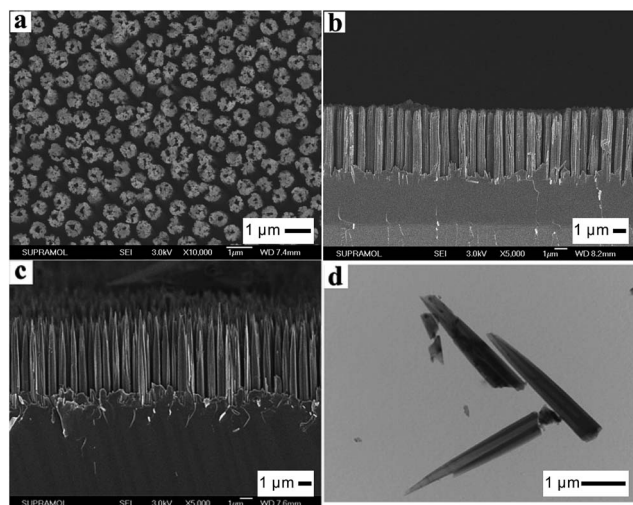


Fig. 8 SEM images of (a) top view and (b) side view of a hollow silicon columnar array, formed *via* Ag-assisted chemical etching; and (c) side view of this array after a quick RIE process, demonstrating hollow needle-like structures, with a height of  $\sim 7.1 \mu\text{m}$ ; (d) TEM image of the hollow-needles isolated from the silicon substrate.<sup>99</sup> Reproduced by permission of the Royal Society of Chemistry.

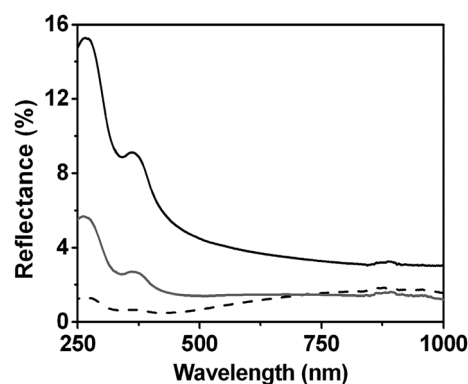


Fig. 9 Reflectance spectrum of hollow-needle arrays of different lengths, *i.e.*,  $2.1 \mu\text{m}$  (black solid line),  $3.4 \mu\text{m}$  (gray solid line), and  $7.1 \mu\text{m}$  (black dash line) in the UV-VIS-NIR region.<sup>99</sup> Reproduced by permission of the Royal Society of Chemistry.





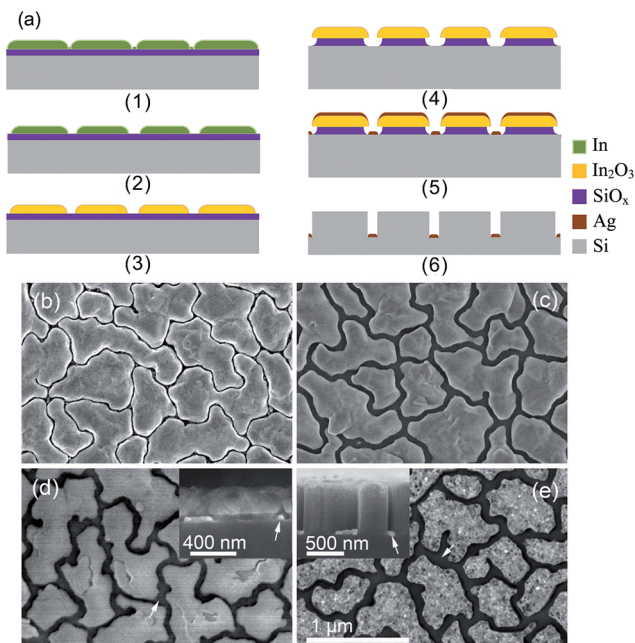


Fig. 10 (a) Schematic illustration of Guo's experimental procedures to fabricate conductive BSi surfaces: (1) deposition of a dual layer (In/SiO<sub>x</sub>) thin film on a silicon wafer; (2) enlargement of the gap size between In islands via dilute HNO<sub>3</sub> etching; (3) oxidation of In islands; (4) HF etching through an In<sub>2</sub>O<sub>3</sub> mask; (5) deposition of Ag film, to form an Ag nanowire mesh on a silicon substrate; (6) Ag-assisted chemical etching, during which the Ag mesh sinks into the silicon wafer and the In<sub>2</sub>O<sub>3</sub> mask is removed. (b)–(e): SEM images corresponding to fabrication steps (1), (2), (5) and (6). In (d) and (e), the Ag nanowire meshes are indicated by arrows.<sup>102</sup> Reproduced by permission of John Wiley & Sons, Inc.

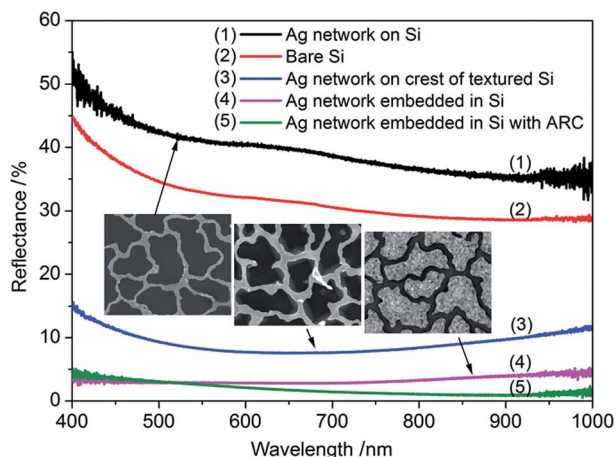


Fig. 11 Reflectance spectra of different BSi samples.<sup>102</sup> Reproduced by permission of John Wiley & Sons, Inc.

by varying the process parameters, such as the size, shape and surface coverage of noble metal nanoparticles, etchant concentration and the etching time.<sup>103</sup> This etching technique can be applied to c-Si, mc-Si, and amorphous Si (a-Si),<sup>104,105</sup> as well as other materials, such as GaAs, GaN, and SiC.<sup>92</sup> It has grown increasingly popular over the last decade, especially in a

research context, and remains as a mainstream etching method. From a solar cell perspective, however, metal contamination is a major concern with this technique, and a thorough metal removal and cleaning process is required to address this problem.

## 2.4. Reactive ion etching

The use of reactive ion etching (RIE) to form grass-like BSi surfaces was first reported by Jansen *et al.* in 1995.<sup>106,107</sup> This method employs SF<sub>6</sub> and O<sub>2</sub> gases to generate F\* and O\* radicals. F\* is responsible for etching silicon, producing volatile products such as SiF<sub>x</sub>. These products, particularly SiF<sub>4</sub>, react with O\* to form a passivation layer of SiO<sub>x</sub>F<sub>y</sub> on a cooled silicon substrate.<sup>108,109</sup> This passivation layer is partly removed by ion bombardment and the exposed silicon is further etched by F\*. The etching reaction is exothermic, and reduces the chance of producing a new passivation layer since SiO<sub>x</sub>F<sub>y</sub> is prone to desorption upon heating. In contrast, there is far less ion bombardment on the side walls of the formed silicon columns; so the passivation layer there is largely preserved, preventing further etching.<sup>110</sup> This etching/passivation competition mechanism leads to the formation of random silicon microstructures with very high aspect ratios in a self-masking fashion (Fig. 12).

The morphology of the BSi made in this manner can be adjusted by changing various RIE parameters, such as gas composition and flow rate, system temperature, substrate bias and RF power.<sup>111–115</sup> By increasing the O<sub>2</sub> flow rate, deposition of the passivation layer is enhanced. Raising the temperature increases the desorption rate of the passivation layer; in fact, SiO<sub>x</sub>F<sub>y</sub> mostly desorbs as the wafer temperature is raised from –100 °C to –60 °C;<sup>113</sup> this effect also indicates that RIE is typically performed at low temperature, *i.e.*, at –110 °C, and is sometimes referred to as cryogenic RIE in the literature. By tuning the coverage of the passivation layer, one gains control of the nanostructure density. Moreover, increasing substrate bias during the RIE process controls the kinetic energy of the ions and the associated ion bombardment effects, thus determining the etching rate.

In addition to conventional RIE systems, a number of improved experimental setups have been introduced. Yoo *et al.* designed a multi-cathode RIE setup,<sup>116</sup> making use of the hollow cathode effect (Fig. 13).<sup>117</sup> In this system, a number of cathodes are placed in parallel, allowing multiple wafers to be processed simultaneously. As the parallel-oriented cathodes are negatively biased, electrons are trapped between the electrode plates and produce a high density plasma, approximately one order of magnitude greater than that generated by a standard parallel plate RIE system. Owing to the high plasma density, the etch rate is greatly enhanced. Moreover, this system is also characterized by its low voltage, which ensures less ion-induced wafer damage. Using this system, Yoo and co-workers successfully fabricated “needles” of BSi with diameters of 50–100 nm and heights of ~500 nm. The reflectance of the resulting BSi was close to zero, over the wavelength range from 200 to 1100 nm.<sup>116</sup>

Xia and co-workers employed plasma immersion ion implantation (PIII) to perform SF<sub>6</sub>/O<sub>2</sub> reactions with silicon

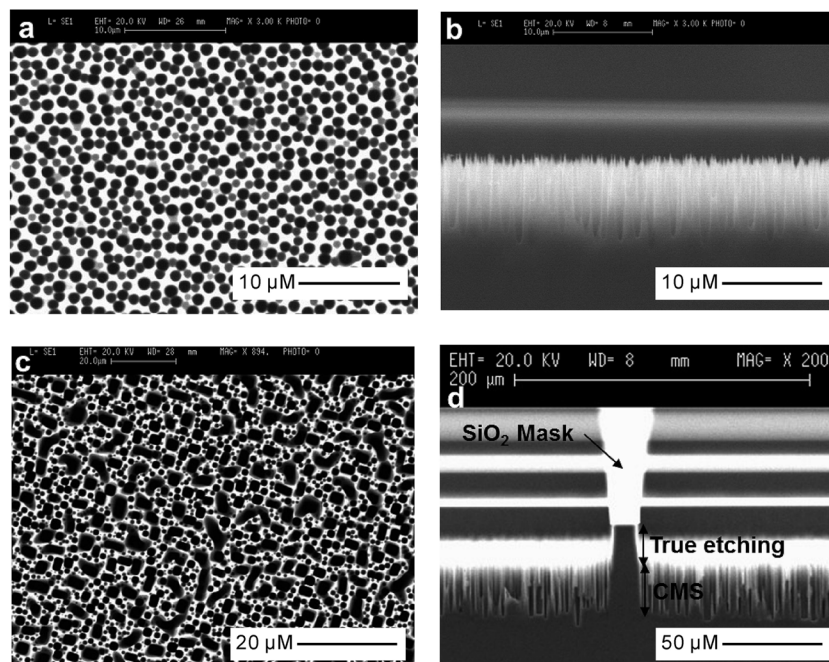


Fig. 12 SEM images of BSi fabricated by RIE under different conditions. (a) and (b) Top and side views of BSi, with RF power = 1500 W, bias = 40 V,  $O_2/SF_6 = 0.09$ , pressure = 10 Pa, time = 10 min. (c) and (d) top and side views of BSi, with RF power = 1500 W, bias = 30 V,  $O_2/SF_6 = 0.07$ , pressure = 3 Pa, time = 30 min.<sup>110</sup> © IOP Publishing. Reproduced by permission of IOP Publishing. All rights reserved.

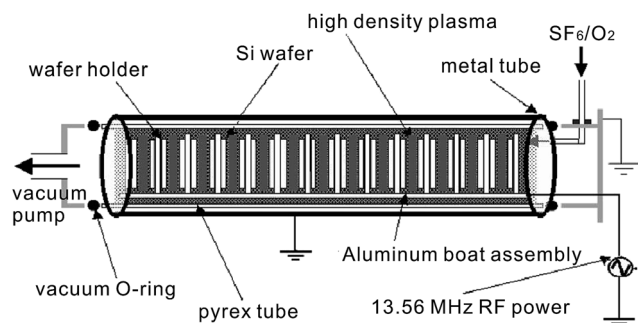


Fig. 13 A multi-cathode RF system for RIE process.<sup>116</sup> Adapted by permission of Elsevier.

substrates.<sup>118,119</sup> In the PIII setup, a strong negative bias ( $\sim -500$  V) is applied to the wafer holder, which is immersed in a plasma cloud. This negative bias repels electrons from the holder, but attracts and accelerates positive ions to the wafer for doping, surface modification, sub-surface chemical reaction and so forth.<sup>120</sup> It affords simpler machine design and maintenance for large-area and high-throughput processing with a uniform dose.<sup>120</sup> By varying the  $SF_6/O_2$  gas composition, a wide range of surface structures have been fabricated (Fig. 14) that exhibit a broadband of low reflectance, with weighted value (from 200–1100 nm) down to  $\sim 1\%$  (Fig. 15).

It is also possible to replace or change the composition of the reaction gases,  $SF_6/O_2$ , which are constrained by a tight composition window to achieve an optimal BSi texture. For example, Murias *et al.* added  $CH_4$  into  $SF_6/O_2$  to enhance the micro-masking effect, due to the formation of polymer on

silicon.<sup>121</sup> Consequently, their RIE produced a high density of pyramid-like structures in the resulting BSi, with average reflectance down to  $\sim 4\%$  in the 400–700 nm region.

Another alternative reactive gas is  $Cl_2$ ,<sup>122–125</sup> which offers a lower etching rate in comparison to  $SF_6/O_2$  but is much easier to manage, owing to the formation of nonvolatile by-products, and thus makes the control over the passivation layer deposition and silicon etching comparatively straightforward.<sup>122–124</sup>  $Cl_2$  can also be added into  $SF_6/O_2$  to enlarge the gas composition working window. Lee *et al.* claimed that in this new system, the *in situ* surface damage removal could be realized by properly adjusting the plasma power density and gas composition.<sup>126</sup>

Several other groups have used  $SiH_4$ ,  $CH_4$ , Ar and  $H_2$  as reactive gases to fabricate sharp grass-like silicon tip structures during high-density electron cyclotron resonance plasma etching.<sup>127–129</sup> In these experiments, the reaction of  $SiH_4$  and  $CH_4$  forms nano-sized SiC which acts as a silicon mask, leaving the uncovered silicon substrate to be etched by argon and hydrogen plasma. The morphologies of the resulting structures can be easily controlled by adjusting system temperature, gas pressure and composition. Increasing the temperature raises the SiC mask formation rate, and boosts the desorption of reactive ions, such as H,  $H^+$ ,  $H_2^+$ ,  $H_3^+$ ,  $Ar^+$ ,  $Ar_2^+$ ,  $ArH^+$ , thus limiting the etching rate. Consequently, the coverage of SiC increases, while the density and length of resulting nanostructures decrease. At a very high temperature, the SiC formation rate becomes so high that the resulting SiC nano-clusters cover the entire wafer surface, preventing further etching.<sup>127,128</sup> Using this approach, Huang *et al.* fabricated tapered aperiodic structures with apex diameters of  $\sim 3$ –5 nm,





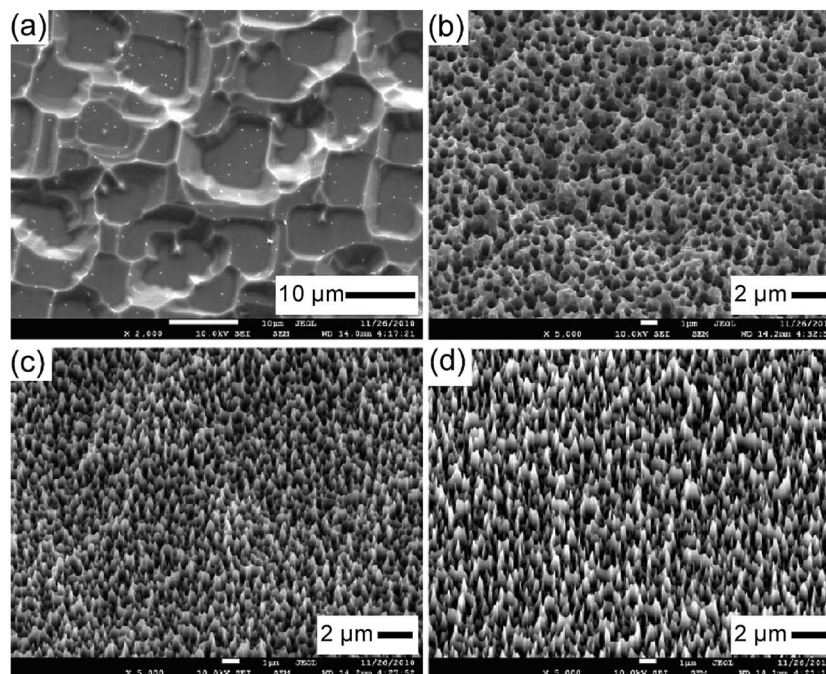


Fig. 14 SEM images of BSi samples fabricated *via* the PIII process at different reactive gas flow rates. (a)  $\text{SF}_6$ ; (b)  $\text{SF}_6/\text{O}_2 = 3.5$ ; (c)  $\text{SF}_6/\text{O}_2 = 4.0$ ; and (d)  $\text{SF}_6/\text{O}_2 = 4.5$ .<sup>118</sup> Reproduced by permission of Elsevier.

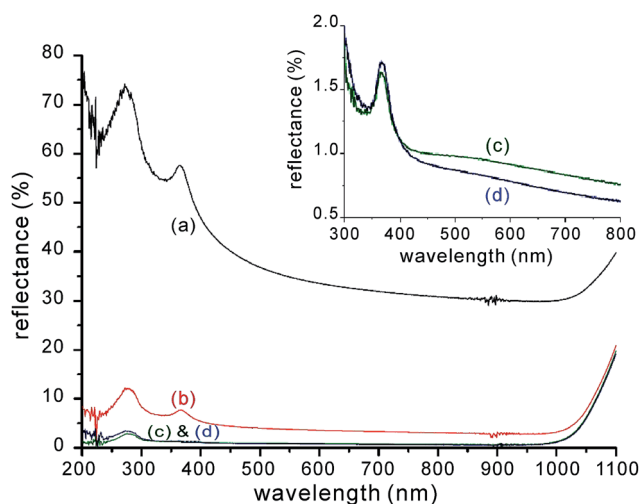


Fig. 15 Reflectance spectra of BSi samples produced by PIII etching, as a function of  $\text{SF}_6/\text{O}_2$  gas ratio: (a)  $\text{SF}_6$  (black); (b) 3.5 (red); (c) 4.0 (green); and (d) 4.5 (blue). The inset shows magnified spectra of cases (c) and (d).<sup>118</sup> Adapted by permission of Elsevier.

base diameters of  $\sim 200$  nm, and lengths from 1 to 16  $\mu\text{m}$  (Fig. 16). These structures effectively suppress reflection over a broad wavelength range, and across a wide range of incidence angles and for both s- and p-polarized light (Fig. 17). The anti-reflection result improves as the silicon surface structures increase in height. For a heights above 5  $\mu\text{m}$ , the reflectance is below 1% over 0.5–2.5  $\mu\text{m}$ , and as low as 0.2% in the 250–400 nm range.<sup>129</sup>

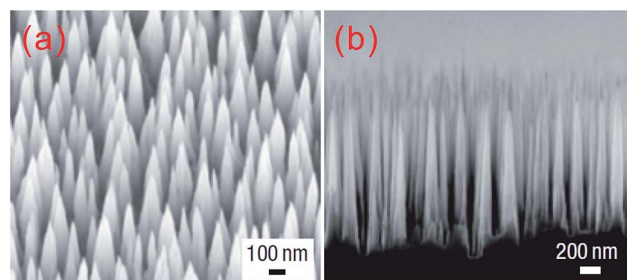


Fig. 16 SEM images of (a) a tilted top view and (b) a side view of a silicon nano-tip array, with a base diameter of  $\sim 200$  nm and a height of 1600 nm.<sup>129</sup> Reproduced by permission of Nature Publishing Group.

Similarly, Chen and co-workers have employed hydrogen bromide (HBr) and oxygen ( $\text{O}_2$ ) during their plasma enhanced RIE.<sup>130</sup> During this process, bromide ions are primarily responsible for etching silicon, resulting in the formation of  $\text{SiBr}_4$ . This reaction product can also react with  $\text{O}^*$  radicals to form random distributed  $\text{SiBr}_x\text{O}_y$  particles, acting as etching masks. By adjusting the gas flow ratios (as well as other process parameters, such as substrate temperature) and controlling this etching-passivation competition mechanism, a wide range of nanostructures, such as nanowhiskers, nanorods and nanotips, have been fabricated.<sup>130</sup>

It is also worth mentioning another deep RIE, or Bosch, process, in which  $\text{CF}_6$  and  $\text{C}_4\text{F}_8$  are alternatively introduced into the reaction chamber for etching and passivation, respectively.<sup>131,132</sup> By repeating this process for hundreds or even thousands of cycles, a very deep and near-vertical silicon needle structure can be fabricated (Fig. 18). Note that this two-step





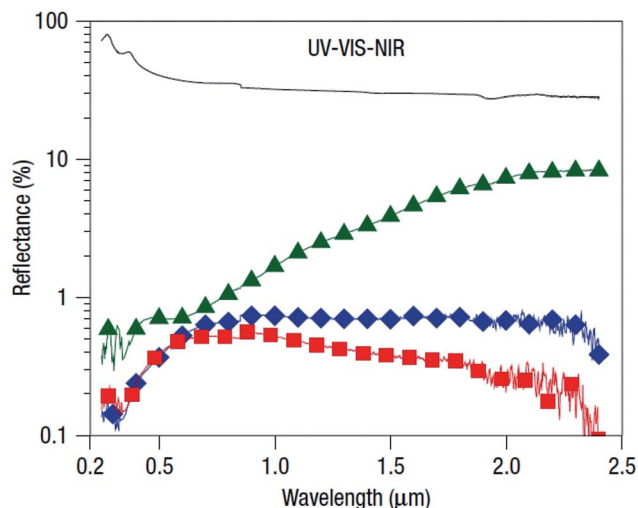


Fig. 17 Reflectance spectra of a planar silicon wafer (solid line, black), and Si nano-tip arrays with different heights, *i.e.*, 1.6 μm (green), 5.5 μm (blue) and 16 μm (red) in the UV-VIS-NIR region.<sup>129</sup> Reproduced by permission of Nature Publishing Group.

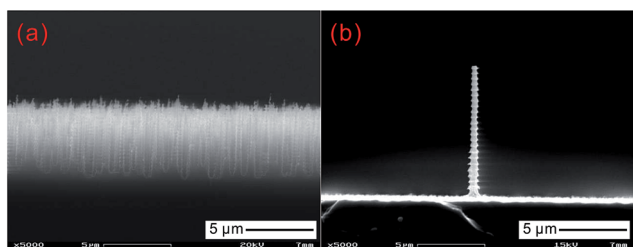


Fig. 18 (a) SEM image of BSi formed by Bosch RIE process; (b) SEM image of a single silicon "needle" produced by Bosch RIE process, with undulated side wall. Image Courtesy of Christoph Kubasch from Institute of Semiconductors and Microsystems, Faculty of Electrical and Computer Engineering, Dresden University of Technology.

cycle process induces an undulating structure on the sidewalls of the silicon needles, with an amplitude of several hundreds of nanometers, in contrast to the smooth side wall produced by cryogenic RIE (Fig. 12).

RIE can also be performed in combination with photolithography or colloidal-particle defined masks to produce periodic or quasi-periodic structures.<sup>133,134</sup> RIE systems are commercially available and are able to process various types of silicon wafers on a large scale. However, its process optimization is relatively complicated, and its cost is also potentially high, owing to the use of vacuum equipment.<sup>135</sup> Moreover, RIE causes significant surface damage to the silicon substrate, reducing the minority carrier lifetime near the surface region (Fig. 19).<sup>136,137</sup> In order to recover the minority carrier lifetime, a subsequent etching is required to remove the top 20–50 nm of the wafer surface, in addition to a RCA (Radio Corporation of America) cleaning of the sample that removes the metallic and organic contaminants. Additional measures, such as lowering the RF power and substrate bias, limiting the process time and usage of O<sub>2</sub> during RIE etching, and performing wafer

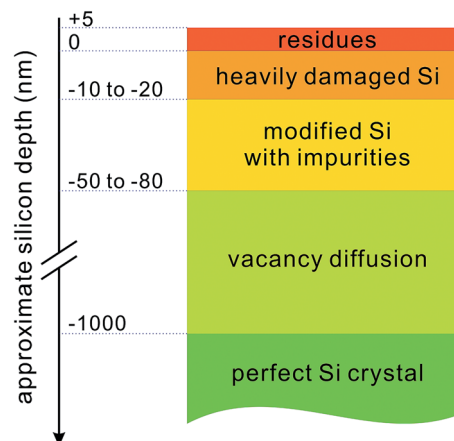


Fig. 19 A schematic illustration of the RIE induced damage to a silicon substrate.<sup>136</sup>

annealing at high temperature (*i.e.*, 400 °C) after the etching, also help to improve the minority carrier lifetime, but at the expense of a lower etching or throughput rate and higher cost.<sup>136</sup>

## 2.5. Laser treatment

Femtosecond-laser (fs-laser) treatment is a versatile technique for performing surface texturing on silicon substrates.<sup>138–144</sup> By irradiating a silicon wafer with a fs-laser in SF<sub>6</sub>, Mazur *et al.* produced conical silicon spikes up to 50 μm high, with a base area of ~6 × 10 μm<sup>2</sup>, tapering to ~1 μm at the tip. The fs-laser structured silicon micro-spike consists of a crystalline core, a highly disordered surface layer (<1 μm thick), and is covered with silicon nanoparticles of 10–50 nm in diameter [Fig. 20a, c and e].<sup>142</sup>

In these experiments, since the laser pulse is in the sub-picosecond region, thermal equilibrium cannot be established in the silicon substrate. Instead, the excitation of electrons from the bonding to anti-bonding states causes repulsive forces and disorder in the lattice structure while remaining thermally cold.<sup>145</sup> Both experiments and simulation have showed that the covalently bonded lattice becomes unstable and leads to disorder formation upon the excitation of ~10% electrons from the valance band to the conduction band; this mechanism is responsible for the roughened silicon surface.

While the roughened surface texture here greatly minimizes surface reflection, one major advantage of laser treatment in a SF<sub>6</sub> environment is the introduction of sulfur atoms (~1 atom %) and structural defects into the silicon lattice of the final product, thus creating more absorbing states in the sub-band gap region of silicon.<sup>141,146</sup> These two factors result in ~90% absorption efficiency from 0.25 to 2.5 μm for silicon wafers coated with ~10–12 μm long spikes, compared to an untreated silicon surface, with absorption efficiency of merely ~60% which occurs mainly in the visible region (Fig. 21). Similarly, selenium and tellurium can also be introduced into silicon by spreading their powders onto a silicon substrate<sup>147</sup> or applying ion implantation,<sup>148</sup> followed by laser irradiation. Such doping



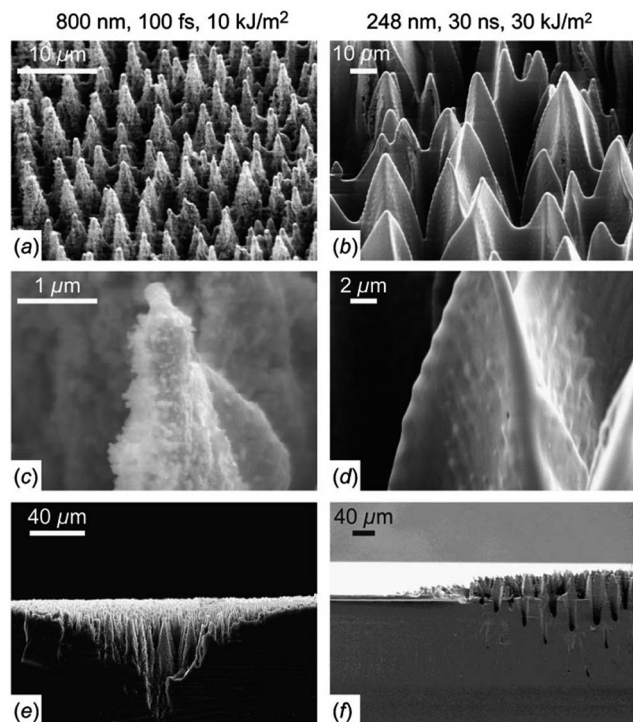


Fig. 20 SEM images of laser-treated silicon surfaces in a  $\text{SF}_6$  environment with [(a), (c) and (e)] fs-laser, and [(b), (d) and (e)] ns-laser. (e) and (f) show the side views of the snapped samples. Reproduced with permission from ref. 142. Copyright 2004, AIP Publishing LLC.

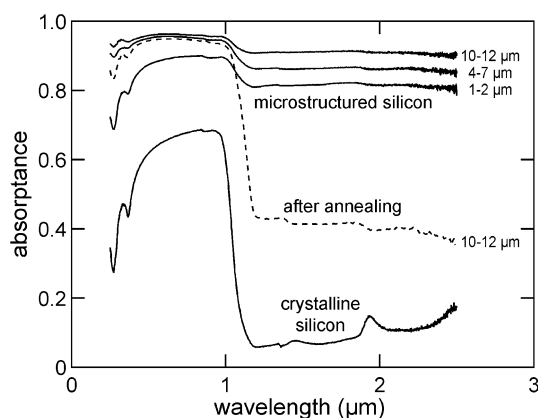


Fig. 21 Absorbance spectra of laser treated BSi samples and a standard wafer. Reproduced with permission from ref. 141. Copyright 2001, AIP Publishing LLC.

also leads to strong sub-bandgap absorption.<sup>147,148</sup> It is interesting to point out that ion-implantation can also be applied to BSi fabricated by other techniques, such as metal-assisted chemical etching, to realize sulfur doping and sub-band absorption.<sup>149</sup>

Owing to laser induced damage, this micro-structured silicon surface is rendered less electronically active.<sup>150</sup> Post-annealing is often performed to reduce the number of defects and improve carrier mobility, while leaving the silicon surface

morphology largely unchanged.<sup>142</sup> However, the annealing temperature requires careful control, because a low temperature anneal does not remove sufficient defects, causing a poor electronic response in the silicon substrate. In contrast, a high temperature annealing significantly decreases the below-bandgap absorption, degrading the overall photoresponse of the micro-structured wafer.<sup>146</sup>

Where doping is not required, one may perform laser irradiation *in vacuo*, or in a non-reactive gas environment. In this case, blunted structures are produced.<sup>139</sup> For example, Sarnet *et al.* have produced microstructures with heights of  $\sim 10\ \mu\text{m}$  and spacings of  $\sim 2.5\ \mu\text{m}$ , so-called “penguin” structures, which have much smoother surfaces in comparison to those produced in  $\text{SF}_6$  (Fig. 22).<sup>151,152</sup> The penguin structures display a flat high absorbance ( $>90\%$ ) over a broadband (350–1000 nm) and reduce the weighted reflectance of silicon from over 30% to  $\sim 9\%$ , owing to enhanced light scattering and trapping effects.<sup>151</sup>

During laser treatment, many parameters can be tuned to optimize the BSi morphology and performance, such as laser polarization, spot size, power density, shot number, scanning parameters, and ambient environment.<sup>152–154</sup> Laser power mainly determines the ablation and silicon volatilization rate, and the pulse number controls the interaction time of laser and silicon, since a longer interaction time transfers energy to the deeper part of a wafer.<sup>153</sup> Given a certain amount of laser energy, these two factors can be optimized in order to produce very high spikes. In addition, studies by Huang suggest that laser fluence, the energy delivered per unit (or effective) area, plays a critical role on the resulting surface morphology.<sup>154</sup> They have shown that as the laser fluence grows, the size of the surface micro- and nano-structures generally increases and the surface roughness is greater. Crucially, the spatial frequency of these features follow a discrete decreasing pattern, *i.e.*,  $2f$ ,  $f$ ,  $f/2$ ,  $f/4$ , and  $f/8$ , where  $f$  is the fundamental frequency corresponding to near-subwavelength ripples. It is proposed that  $f/2$ ,  $f/4$ , and  $f/8$  are

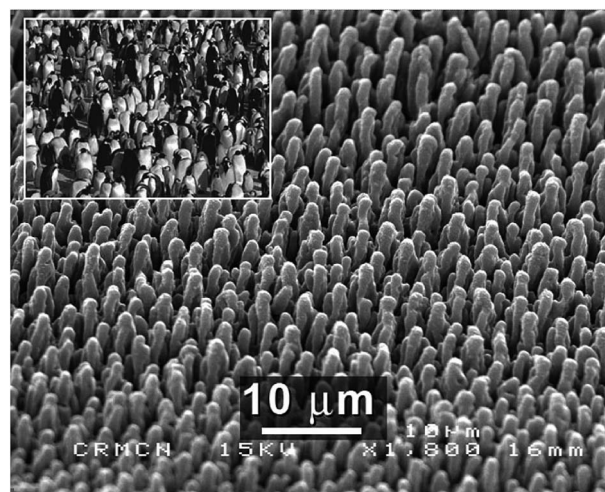


Fig. 22 SEM image of penguin-like silicon microstructures created by fs-laser irradiation; the inset shows a real penguin colony.<sup>151</sup> Reproduced by permission of Elsevier.



from the 2-order, 4-order, 8-order grating coupling.<sup>154</sup> Furthermore, laser treatment can also be performed in water or oil. Much smaller structures, down to sub-100 nm, *i.e.*, one or two orders of magnitude lower than that in the gas environment or *in vacuo*, have been reported.<sup>155,156</sup> These results can be explained by a combined effect of capillary waves on the molten silicon surface in conjunction with laser-induced etching.<sup>155</sup> Laser irradiation may also be employed with a periodic mask to produce more ordered micro-spikes on a silicon wafer.<sup>157</sup>

Laser treatment is not restricted to grain orientation and so can be applied to both c-Si and mc-Si. BSi generated by laser irradiation, especially with sulfur doping, is useful in many different applications. For example, the nanostructured protrusions produced in a SF<sub>6</sub> environment are luminescent upon annealing, and the luminescent wavelength can be modified by varying the annealing temperature.<sup>150</sup> The improved photo-responsivity of the BSi also makes it an ideal photodiode material (Fig. 23).<sup>146,158</sup> Carey *et al.* have shown that photodiodes made of n-type BSi demonstrate a higher responsivity than commercially available silicon photodiodes, *i.e.*, two orders of magnitude higher in the visible region and five orders of magnitude higher in the near infrared region.<sup>146</sup> Moreover, the working window is extended into the infra-red region, owing to the formation of a sulfur-doping induced intermediate band. An avalanche photodiode has also been fabricated with this type of BSi, which offers a lower breakdown voltage (500 V in comparison with 900 V in untextured silicon).<sup>141</sup> Heavily sulfur doped silicon can also be used to fabricate intermediate band photovoltaics. Nevertheless, Sullivan *et al.* have shown that the figure of merit of this material is too low for solar cell applications, in contrast to a single bandgap material.<sup>159</sup>

The laser process is relatively slow in comparison to other etching techniques, especially on an industrial scale, although its processing rate can be improved by increasing laser repetition rate,<sup>161</sup> or raising laser power/spot size. Furthermore, laser induced material damage can be quite substantial; thorough defect removal etching is required when a high material quality is of great concern, as in the case of photovoltaic applications.

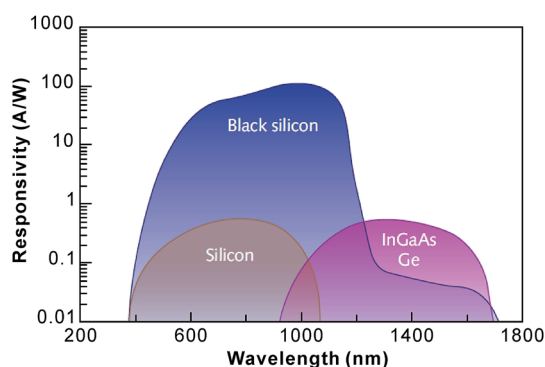


Fig. 23 The responsivity of a BSi photo-detector in comparison to those of standard silicon, InGaAs and Ge.<sup>160</sup> Reproduced by permission of Laser Focus World.

## 2.6. FFC-Cambridge process

Porous BSi can also be fabricated *via* the FFC-Cambridge process. This process was first developed by Chen, Farthing and Fray to electrochemically reduce TiO<sub>2</sub> to Ti in molten salt CaCl<sub>2</sub> at ~850 °C.<sup>162</sup> This simple and cost-competitive approach can also be used to reduce other metal oxides to pure metals, such as Ti, Ta, Cr, and Fe.<sup>162</sup> Nohira *et al.* further extended this method to directly reduce SiO<sub>2</sub> to silicon (Fig. 24).<sup>163</sup> In Nohira's experiment, a ~1 mm thick SiO<sub>2</sub> plate was bound by Mo wires, forming a cathode, and immersed into molten CaCl<sub>2</sub>. The surface layer of the SiO<sub>2</sub> plate was first reduced into silicon at the conductor (Mo)–insulator (SiO<sub>2</sub>)–electrolyte (CaCl<sub>2</sub>) three-phase interface, upon applying a voltage bias (~–1 V *versus* Ca<sup>2+</sup>/Ca) to the cathode. The O<sup>2–</sup> anions extracted during the process, diffuse through CaCl<sub>2</sub>, reach the graphite anode, and are then oxidized into mainly O<sub>2</sub> as well as some CO and CO<sub>2</sub> gases.<sup>164</sup> On the cathode side, the reduced silicon is porous, owing to the removal of oxygen from SiO<sub>2</sub>; the silicon is also conducting at such a high temperature, with a resistivity of ~0.02 Ω × cm.<sup>165</sup> Consequently, the molten salt infiltrates into silicon pores to form a new conductor (Si)–insulator (SiO<sub>2</sub>)–electrolyte (CaCl<sub>2</sub>) three-phase interface, which drives the reduction process. Eventually, after electrolysis for one hour, a ~100–200 μm thick porous silicon layer is produced, with purity higher than 90%.<sup>163</sup> The resulting silicon possesses good crystallinity, because the transition from amorphous to crystalline silicon occurs above 470 °C.<sup>166,167</sup>

Since Nohira's experiments, the silicon reduction mechanism and process control parameters in the FFC-Cambridge process have been analyzed in detail by several groups.<sup>163,164,169–172</sup> The solubility of O<sup>2–</sup> ions in the molten salt plays a key role in the process,<sup>163</sup> where its diffusion in the silicon pores controls the overall SiO<sub>2</sub> reduction rate.<sup>169</sup> Silicon can be successfully produced when the working electrode (cathode) potential is between –0.70 and –1.25 V (*versus* Ca<sup>2+</sup>/Ca), and the reduction rate increases as the cathode potential is lowered. However, when

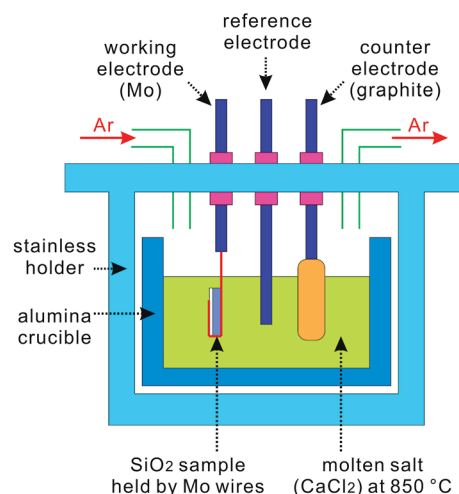


Fig. 24 Experimental setup of the FFC-Cambridge process to produce porous silicon.<sup>168</sup>





the working electrode potential drops further, *i.e.*, to 0.35 V, the formation of CaSi and CaSi<sub>2</sub> alloys becomes quite significant.<sup>170</sup> In addition, one may minimize metal contamination during the SiO<sub>2</sub> reduction process by replacing the metal electrode with a silicon plate, which can be directly tied to the SiO<sub>2</sub> plate. With this strategy, Yasuda *et al.* obtained a high silicon purity of 99.80% by following the electroreduction with a melting and solidification process at 1500 °C.<sup>171</sup>

Using the FFC-Cambridge process, the Fray Group successfully produced a layer of porous silicon by electrochemically reducing a 2 µm thick thermal oxide layer.<sup>173,174</sup> The porous silicon consisted of globular structures, with diameters of several hundreds of nanometers (Fig. 25). Nano-fibers also exist, with diameters of several tens of nanometers, embedded between these globular structures. The measured reflectance of the porous silicon is ~10% across the entire silicon absorption spectrum (400–1100 nm; Fig. 26), making it an especially viable candidate for an antireflection coating on silicon solar cells.<sup>174</sup> The presence of nano-fibers also suggests that it has potential luminescent applications upon processing and structural optimization.

The FFC-Cambridge process is a potentially cheaper and simpler process for producing solar grade silicon at scales to meet industrial demands. This technique is highly versatile, and can be used to deposit thin silicon films onto metal sheets,<sup>168,175</sup> and to fabricate free-standing nanowire arrays.<sup>176</sup> When used to produce a porous BSi anti-reflection layer, this technique affords little material wastage, owing to its electrochemical reduction nature, in contrast to etching processes. This technique is, however, a high temperature process (~850 °C), which can render silicon wafer prone to Mo and other metal contaminations<sup>171</sup> and the high temperature may degrade solar cell performance, especially for wafers made from mc-Si, owing to the diffusion of impurities from grain boundaries into grains.<sup>177</sup>

### 3 Black silicon properties

BSi possesses a few unique properties not found in bulk silicon,<sup>40</sup> making it an ideal candidate material for solar cell components:

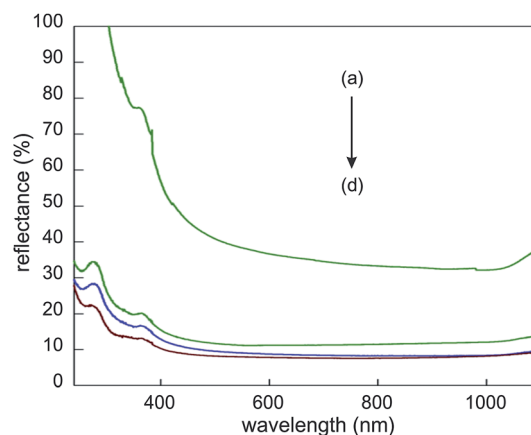


Fig. 26 Reflectance spectra of BSi samples: (a) polished silicon; electro-deoxidized porous silicon with different deoxidation times of (b) 1 h, (c) 17 min and (d) 3 min.<sup>174</sup> Adapted by permission of the Electrochemical Society.

- Light trapping and anti-reflection, which can be exploited to allow anti-reflection coating (ARC) layers to be fabricated.<sup>178–180</sup>
- Modified band gaps controlled by impurity doping, which can be employed to design multi-junction solar cells.
- Low mechanical strength, which can be used to easily separate ultra-thin wafers from silicon ingots.
- Gettering effects, the results of large and active surfaces, which can be utilized to reduce impurities in the wafer.

#### 3.1. Anti-reflection coating

**3.1.1. Optical characteristics.** Optical management in thick wafer-based solar cells is mainly undertaken by reducing front surface reflection, *via* a combined use of anti-reflection (AR) coatings and surface texture. The surface texture additionally acts as a light trap and improves light absorption in the long wavelength range. Industry has traditionally used wet etching to develop textures on silicon solar cells because of its low cost, high etching rate, and good uniformity across large areas.<sup>80</sup> In (100) c-Si wafers, alkaline wet etching is often adopted to form pyramidal structures that are 5–15 µm deep for light scattering

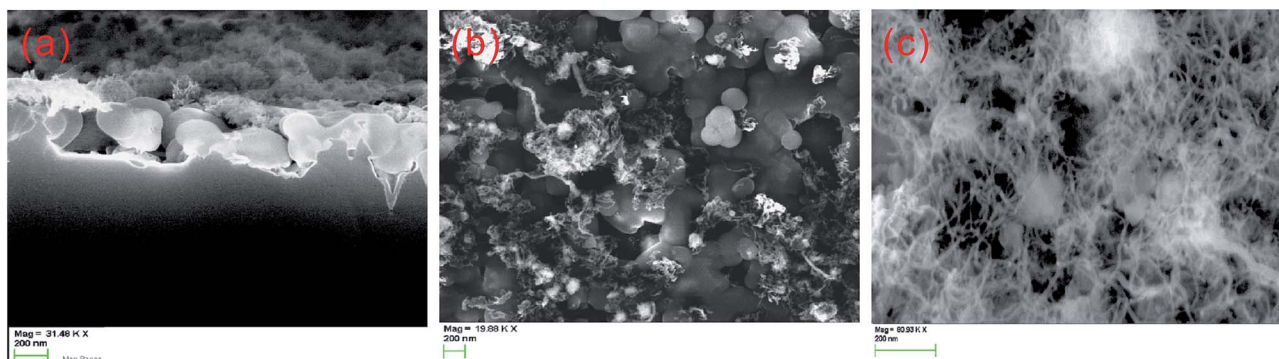


Fig. 25 SEM images of porous silicon formed through the FFC-Cambridge process by directly reducing a 2 µm SiO<sub>2</sub> precursor at  $E = -1.0$  V and  $t = 20$  min. (a) Side and (b) top views of silicon nano-nucleation; and (c) top view of silicon nano-fibres. Scale bar = 200 nm.<sup>174</sup> Reproduced by permission of the Electrochemical Society.



and anti-reflection applications, resulting in a weighted reflectance of  $\sim 15\%$  on wafers without AR coating (Fig. 27a).<sup>35,181</sup> Reducing the sizes of these pyramidal structures, *i.e.*, to  $\sim 4\text{--}6\text{ }\mu\text{m}$  in depth, could lower the weighted solar reflectance to  $11.4\text{--}12.2\%$ .<sup>182</sup> By adding a quarter-wavelength AR coating, typically made from  $\text{SiO}_2$  or  $\text{SiN}_x$ , the fraction of reflected photons can be further reduced to  $2\%$  or less for this type of texture. The  $\text{SiO}_2$  or  $\text{SiN}_x$  coating also improves surface passivation (see Section 4).

Alkaline etching is anisotropic and creates undesirable steps along the grain boundaries in mc-Si wafers (Fig. 27b). Consequently, for mc-Si wafer solar cells, the most common type of solar cells available in the market, isotropic acidic texturing is often employed, affording a weighted reflectance of  $\sim 21\text{--}25\%$  (from  $300$  to  $900\text{ nm}$ ) on wafers without AR coating.<sup>80,183–185</sup> On mc-Si wafers, dielectric layers are also used to improve the passivation and anti-reflection properties; this results in a weighted reflectance down to  $\sim 5\%$  for isotextures.

It is a common manufacturing trend to produce ever thinner solar wafers, for reducing material cost and relaxing the requirements on wafer impurity levels and associated carrier diffusion lengths.<sup>186,187</sup> As wafer thickness decreases, it becomes increasingly difficult to undertake conventional wet etching, owing to its deep etching profile and relatively large wastage of silicon material. Conventional etching techniques, in general, are not appropriate on very thin wafers ( $<10\text{ }\mu\text{m}$ );<sup>137</sup> yet, ARC and

particularly light trapping is critical for the photon management of these thin wafers.<sup>114,188</sup>

An alternative AR solution is to use BSi. BSi helps to reduce reflectance in different ways, depending on the size and shape of its surface texture. First, there is a reflection reduction because of a multitude of interactions of light with the textured surface. Second, when the size of the texture features is large compared to the wavelength of the solar spectrum, surface scattering is responsible for an elongated light path and enhanced absorption.<sup>114,189</sup> Third, for sub- $100\text{ nm}$  nanostructured silicon, the surface feature sizes are so small that the surface essentially acts as an effective index medium and is optically flat.<sup>190</sup> In this case, a smooth refractive index transition from air to bulk silicon, *via* the nanostructured surface, results in an effectively graded-index AR coating which affords a strongly reduced reflectance (Fig. 28).

In the effective index medium region, the substrate material is mixed with air on a sub-wavelength scale. A constant porosity in BSi leads to a step change in refractive index from air to BSi, and then to bulk silicon (Fig. 28b). This porous layer is equivalent to a lower refractive index material. By creating a porosity gradient, a smoother transition in the refractive index from air to bulk silicon [Fig. 28c and d] can be achieved. These BSi layers, such as described in Fig. 28d, lead to a maximum reduction in reflectance;<sup>191–194</sup> the overall reflectance improves as the thickness of the BSi layer increases and as the feature size of the nanostructured silicon becomes smaller.<sup>46,195</sup> The effective medium theory predicts that a  $200\text{--}300\text{ nm}$  thick textured graded index layer is sufficient to almost completely suppress the reflectance across the whole solar spectrum (above the silicon bandgap).<sup>96,191</sup> It should, however, be pointed out that the relationship between silicon porosity and the corresponding refractive index is positive but not linear.<sup>46,190</sup>

Consequently, by increasing its thickness and reducing its feature size, BSi demonstrates comparable, and even superior, low reflection as compared to conventional single layer (such as  $\text{SiN}_x$ ) and double layer (such as  $\text{TiO}_2/\text{MgF}_2$ ) ARC<sup>196</sup> with a reflectance of less than  $1\%$  over a broadband reported.<sup>46,197</sup>

The AR effect of BSi works for a wide range of wavelengths and incident angles, and is polarization-independent.<sup>34,35,198</sup> The wide spectral window of BSi is evident by its flat reflectance

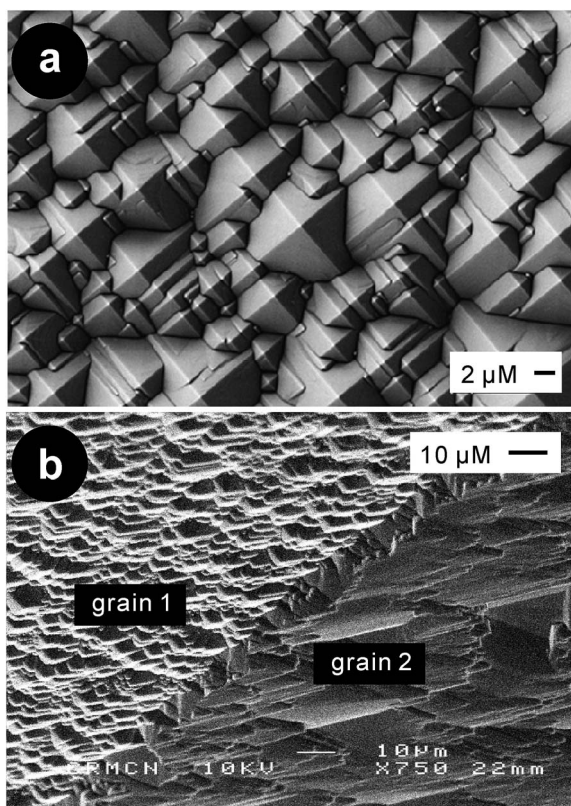


Fig. 27 SEM images of (a) a KOH etching textured (100) c-Si wafer;<sup>182</sup> and (b) anisotropic etching of a mc-Si wafer resulting in grain-dependent texturization.<sup>152</sup> Adapted by permission of Elsevier and SPIE.

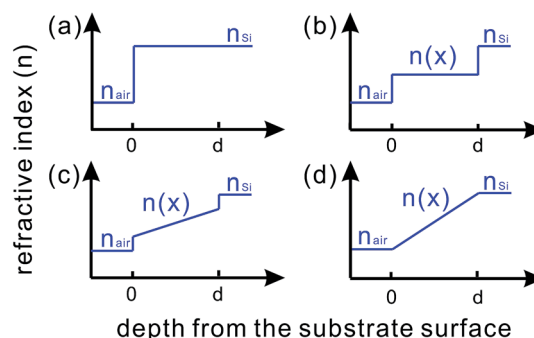


Fig. 28 Refractive index profiles from air to (a) a silicon wafer without any ARC; (b) a silicon wafer with a porous silicon layer of constant porosity; (c) and (d) silicon wafers with gradient porosities.<sup>62</sup>



spectra (with the notable exception of electrochemically etched samples with a fixed porosity, which is equivalent to a homogeneous layer of low refractive index material). Furthermore, the polarization and angular dependence of BSi have been tested by Xie *et al.* and Huang *et al.*, on samples fabricated *via* metal-assisted chemical etching<sup>198</sup> and RIE,<sup>129</sup> respectively. Both types of samples demonstrate a low reflectance up to a large incident angle of  $\sim 80^\circ$  (Fig. 29).

**3.1.2. Electrical performance.** Numerous solar cells with BSi ARC layers have been fabricated by a variety of techniques (Table 1), such as electrochemical HF etching and stain etching,<sup>40,41</sup> laser treatment,<sup>199–201</sup> metal-assisted chemical etching,<sup>32,202</sup> and RIE (including PIII etching).<sup>115,123,203,204</sup> The majority of these BSi cells have similar architectures to a conventional solar cell, in which a p–n junction is formed near the front-surface of a c-Si or mc-Si wafer and metal contacts are screen-printed/deposited on both the front- and rear-surfaces. However, the random alkaline/acid textured surface in conjunction with a single-layer antireflection coating in conventional solar cells has been replaced by a BSi layer (in addition to a thin passivation layer) in BSi solar cells.

Although BSi offers excellent optical performance, its electrical performance in solar cells is, on the whole, quite poor. In some studies, high power conversion efficiencies with BSi have been reported, in comparison to those of planar reference cells.<sup>105,205</sup> These comparisons, however, are typically biased by poor reference cell choices, considering that the surfaces of standard solar cells are always textured. Despite their lower optical reflectance, BSi solar cells generally show lower power conversion efficiencies.<sup>207,224,225</sup> At present, the highest reported efficiencies are 18.2% (ref. 32) (certified by National Renewable Energy Laboratory, USA) and 18.7% (ref. 220) for p-type and n-type c-Si wafer cells, respectively (Fig. 30), *i.e.*, lower than the standard control cells (with random pyramidal textured surfaces, single-layer antireflection coatings and otherwise

similar cell structures as compared to the BSi solar cells) fabricated under similar conditions (Table 2).

The relatively poor performance of BSi-based solar cells is related to its nanostructured surface. Lin *et al.* performed light beam induced current (LBIC) analysis on a BSi solar cell with a porous surface and a reference planar solar cell.<sup>226</sup> A short wavelength laser (*e.g.* 407 nm) was used to characterize the top layer of the solar cells, while a long wavelength laser (*e.g.* 1013 nm) was used to penetrate deeper into the surface and study the bulk silicon properties. This study shows that the bulk of BSi and planar silicon exhibit comparable performances. However, the top surface of the BSi shows a significantly lower LBIC signal compared to the reference solar cell, indicating a poorer performance of the BSi solar cell near the top surface. Yuan *et al.* further showed that the nanostructured layer can be effectively modeled as a dead layer, which is thinner than the actual nanostructured layer thickness.<sup>34,35</sup>

The poor solar cell performance near the nanostructured surface can be attributed to the following causes: (1) the enlarged surface area resulting in increased surface recombination; (2) the surface issuing a heavier and non-uniform doping, leading to substantial Auger recombination and/or shunts; (3) a poor contact to metal fingers. All three factors relate directly to the BSi surface texture.

It is relatively easy to understand the increased surface recombination in BSi, owing to the considerable size of its surface area and associated surface structural defects. This surface recombination may become significant, considering that conventional passivation techniques, such as chemical vapor deposition (CVD) of  $\text{SiN}_x$ , still face considerable challenges in fabricating conformal dielectric coatings on rough surfaces.

A relatively subtle, but equally critical problem in BSi is related to its doping profile. Due to its large surface area, the diffusion of dopants within BSi is much more efficient than in a planar wafer. Currently, most BSi solar cells are still fabricated based on the procedure used for conventionally textured solar cells. Consequently, this leads to very high doping concentrations in BSi emitters, and causes considerable Auger recombination. Such high doping concentrations may even render the effective carrier lifetime independent of the surface area.<sup>32</sup> Oh *et al.* showed that in high doping regions, Auger recombination is a dominating factor for carrier losses in BSi solar cells, while the surface recombination dominates only in low doping regions; in the medium doping region (sheet resistance of  $\sim 90$  to  $210 \Omega \square^{-1}$ ), both surface and Auger recombination mechanisms are important.<sup>32</sup>

In addition to a high doping concentration, non-uniformity in the dopant distribution may also present an issue, especially in nanostructures with high-aspect ratios. For example, Shen *et al.* compared the doping profiles of two fabrication methods.<sup>204</sup> In the first process, the BSi texture was finished first, followed by high temperature doping (Fig. 31a); in the second, the sequence of doping and BSi formation using PIII etching was reversed (Fig. 31b). It was shown that with a thick BSi layer, coated on a silicon substrate by the first process, more dopants entered the nanostructured “needles” *via* the side

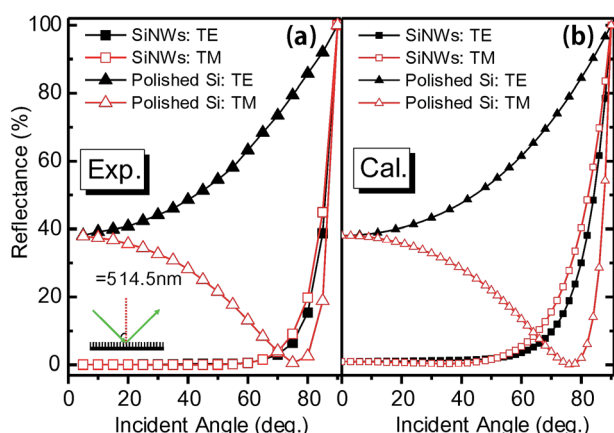


Fig. 29 (a) Measured and (b) calculated reflectance of 800 nm long silicon nanowires for both s-polarized transverse-electric (TE) and p-polarized transverse-magnetic (TM) light at 514.5 nm, as a function of incident angle ( $\theta$ ). The spectra of a polished wafer is also shown for comparison.<sup>198</sup> © IOP Publishing. Reproduced by permission of IOP Publishing. All rights reserved.





Table 1 J–V parameters and efficiencies (eff.) of BSi solar cells fabricated via various techniques<sup>a,b</sup>

S/N	BSi fabrication method	Si type/size	$V_{oc}$ (mV)	$J_{sc}$ (mA cm <sup>-2</sup> )	FF (%)	Eff. (%)	Remarks	Ref.
1	Electrochemical etching	c-Si (CZ), 4 cm <sup>2</sup>	579	28.8	76	12.7	No further passivation; selective emitter	39
2	Electrochemical etching	c-Si (FZ), 4 cm <sup>2</sup>	603	30.4	78	14.3	No further passivation; selective emitter	41
3	Electrochemical etching	c-Si (FZ), 4 cm <sup>2</sup>	601	31.3	78	14.6	No further passivation; micro-nano dual-scale surface texture; <sup>c</sup> selective emitter	41
4	Stain etching	mc-Si, size not specified	569	25.5	68	9.6	No further passivation; selective emitter	205
5	Stain etching	mc-Si, 25 cm <sup>2</sup>	609	29.1	79.7	14.1	No further passivation; selective emitter	41
6	Vapour chemical etching	Polycrystalline-Si, 25 cm <sup>2</sup>	540	24.8	65.6	9.2	No further passivation; selective emitter	85
7	Vapour chemical etching	mc-Si, 25 cm <sup>2</sup>	550	22.4	78	10.0	No further passivation; selective emitter	89
8	Vapour chemical etching	mc-Si, 3.2 cm <sup>2</sup>	560	31.5	74	11.8	No further passivation; buried front contact	206
9	Metal-assisted chemical etching	c-Si (CZ), ~5.76 cm <sup>2</sup>	578	28.9	71	11.7	No further passivation	105
10	Metal-assisted chemical etching	mc-Si, 243.36 cm <sup>2</sup>	604	33.9	77.3	15.8	SiO <sub>2</sub> /SiN <sub>x</sub> stacked layer passivation	207
11	Metal-assisted chemical etching	c-Si, 243.36 cm <sup>2</sup>	616	33.0	77.3	16.1	SiO <sub>2</sub> passivation; micro-nano dual-scale surface texture	208
12	Metal-assisted chemical etching	mc-Si, 232.26 cm <sup>2</sup>	624	36.1	76.2	16.4	SiO <sub>2</sub> /SiN <sub>x</sub> stacked layer passivation	209
13	Metal-assisted chemical etching	c-Si (FZ), ~1 cm <sup>2</sup>	607	34.9	77.2	16.4	SiO <sub>2</sub> passivation	210
14	Metal-assisted chemical etching	c-Si/243.36 cm <sup>2</sup>	615	34.6	76.0	16.5	SiN <sub>x</sub> passivation; micro-nano dual-scale surface texture	208
15	Metal-assisted chemical etching	c-Si (FZ), 4 cm <sup>2</sup>	621	33.1	80.2	16.5	Al <sub>2</sub> O <sub>3</sub> /SiN <sub>x</sub> stacked layer passivation; micro-nano dual-scale surface texture	211
16	Metal-assisted chemical etching	c-Si (FZ), 1 cm <sup>2</sup>	612	34.1	80.6	16.8	SiO <sub>2</sub> passivation; NREL tested	34
17	Metal-assisted chemical etching	mc-Si, 243.36 cm <sup>2</sup>	624	35.2	77.2	16.9	SiN <sub>x</sub> passivation; selective emitter	33
18	Metal-assisted chemical etching	c-Si (FZ), size not specified	615	35.6	78.2	17.1	SiO <sub>2</sub> passivation; micro-nano dual-scale surface texture; NREL tested	35
19	Metal-assisted chemical etching	c-Si, 243.36 cm <sup>2</sup>	623	34.6	77.8	17.1	SiO <sub>2</sub> /SiN <sub>x</sub> stacked layer passivation; micro-nano dual-scale surface texture	208
20	Metal-assisted chemical etching	c-Si (CZ), 156.25 cm <sup>2</sup>	623	35.5	79.3	17.5	SiN <sub>x</sub> passivation; micro-nano dual-scale surface texture	212
21	Metal-assisted chemical etching	c-Si (CZ), 0.92 cm <sup>2</sup>	598	41.3	75.1	18.2	Al <sub>2</sub> O <sub>3</sub> passivation	202
22	Metal-assisted chemical etching	c-Si (FZ), 0.8081 cm <sup>2</sup>	628	36.5	79.6	18.2	SiO <sub>2</sub> passivation; NREL certified	32
23	Metal-assisted chemical etching	c-Si, 243.36 cm <sup>2</sup>	639	37.2	79.1	18.8	SiN <sub>x</sub> passivation; micro-nano dual-scale surface texture	213
24	RIE	c-Si, 0.8 cm <sup>2</sup>	420	24.1	65	6.6	SIS solar cell <sup>d</sup>	214
25	RIE	mc-Si, 100 cm <sup>2</sup>	566	25.0	72	10.2	SiO <sub>2</sub> passivation	116
26	RIE	c-Si, 98 cm <sup>2</sup>	564	28.6	73	11.7	SiO <sub>2</sub> passivation	116
27	RIE	c-Si (CZ), 156.25 cm <sup>2</sup>	611	32.5	77	15.1	SiN <sub>x</sub> passivation	115
28	RIE	mc-Si, 243.36 cm <sup>2</sup>	619	33.5	77.7	16.1	SiN <sub>x</sub> passivation	215
29	RIE	mc-Si, 243.36 cm <sup>2</sup>	614	33.8	78.6	16.3	No passivation details specified	126
30	RIE	c-Si (CZ), 156.25 cm <sup>2</sup>	617	36.8	76	16.7	SiN <sub>x</sub> passivation	124
31	RIE	mc-Si, 243.36 cm <sup>2</sup>	613	36.1	76.0	16.8	SiN <sub>x</sub> passivation	216
32	RIE	mc-Si, 225 cm <sup>2</sup>	621	36.2	76.2	17.1	SiN <sub>x</sub> passivation for both front and rear sides	123
33	RIE	c-Si, 156.25 cm <sup>2</sup>	623	35.4	78.2	17.2	SiN <sub>x</sub> passivation; micro-nano dual-scale surface texture	217
34	RIE	mc-Si, 243.36 cm <sup>2</sup>	632	35.7	77.9	17.6	SiN <sub>x</sub> passivation; selective emitter	218
35	RIE	c-Si (FZ), 4 cm <sup>2</sup>	632	39.2	75.8	18.7	n-Type solar cell; Al <sub>2</sub> O <sub>3</sub> passivation for front side and PassDop <sup>219</sup> passivation for the rear side	220
36	PIII etching	mc-Si, 243.36 cm <sup>2</sup>	600	33.2	77.9	15.5	SiN <sub>x</sub> passivation; doping performed <i>after</i> BSi formation	185
37	PIII etching	c-Si, 156.25 cm <sup>2</sup>	619	32.0	78.3	15.7	SiN <sub>x</sub> passivation	119
38	PIII etching	mc-Si, 243.36 cm <sup>2</sup>	607	34.5	78.1	16.3	SiN <sub>x</sub> passivation; doping performed <i>before</i> BSi formation	204
39	PIII etching	mc-Si, 243.36 cm <sup>2</sup>	613	34.2	77.6	16.3	SiN <sub>x</sub> passivation	221



Table 1 (Contd.)

S/N	BSi fabrication method	Si type/size	$V_{oc}$ (mV)	$J_{sc}$ ( $\text{mA cm}^{-2}$ )	FF (%)	Eff. (%)	Remarks	Ref.
40	PIII etching	mc-Si, 243.36 $\text{cm}^2$	623	36.0	77.8	17.5	$\text{SiN}_x$ passivation	222
41	Laser texturization	c-Si (FZ), 1 $\text{cm}^2$	507	39.2	72	14.1	$\text{SiO}_2/\text{SiN}_x$ stacked layer passivation	200
42	Laser texturization	c-Si (FZ), 1 $\text{cm}^2$	507	39.2	71.4	14.2	$\text{SiO}_2/\text{SiN}_x$ stacked layer passivation	199
43	Laser texturization	c-Si (FZ), 7.3 $\text{cm}^2$	658	37.3	75.0	18.4	$\text{SiO}_2$ passivation for both front and rear sides; double-sided buried contact solar cells	223

<sup>a</sup> Unless otherwise specified, all solar cells reported here are p-type standard cells, *i.e.*, with homojunction and passivated front surface.

<sup>b</sup> Abbreviations used: open circuit voltage,  $V_{oc}$ ; short circuit current density,  $J_{sc}$ ; fill factor, FF; efficiency, eff.; CZ, Czochralski wafers; FZ, flow zone wafers; NREL, National Renewable Energy Laboratory. <sup>c</sup> For micro-nano dual-scale surface texture, micro-pyramid surface texture is firstly developed by anisotropic alkaline etching on (100) wafers; nano-scaled structures are then coated on micro-scaled textures, *via* various BSi fabrication techniques, such as electrochemical etching,<sup>41</sup> metal-assisted chemical etching,<sup>35,208,211–213</sup> and RIE (see Section 5.2 for more details).<sup>217</sup> <sup>d</sup> SIS solar cell: semiconductor-insulator-semiconductor solar cell (see Section 3.2.2 for more details).

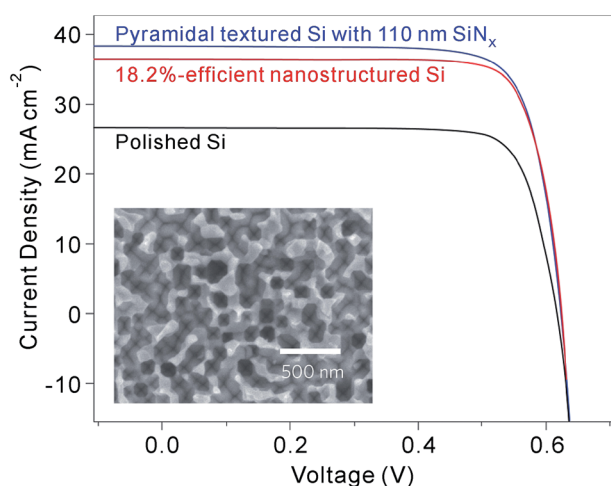


Fig. 30  $J$ - $V$  curves of 18.2%-efficient nanostructured BSi, polished silicon and pyramid-textured silicon with a  $\text{SiN}_x$  antireflection coating under AM1.5 illumination. Inset: top-view SEM image of the BSi solar cell.<sup>32</sup> Reproduced by permission of Nature Publishing Group.

walls, while fewer dopants entered the bulk silicon owing to the smaller contact area. Such non-uniform doping resulted in a varied thickness of the depletion region, a corresponding lateral

field and a lower shunt resistance, as deduced from electron beam-induced current (EBIC) imaging (Fig. 31c). In contrast, with doping performed before the BSi formation, the second process afforded a shallower BSi layer and a more uniform doping profile, contributing to a higher power conversion efficiency of 16.3%, in comparison to 15.5% achieved using the first process.<sup>204</sup>

The same problem of low shunt resistance and high leakage current due to non-uniform doping in BSi was also found by Hsu *et al.*<sup>209</sup> Hsu and co-workers fabricated BSi with different nano-rod lengths using Ag-assisted chemical etching on 6" wafers, and produced solar cells using standard fabrication procedures. Electroluminescence (EL) imaging characterization showed that BSi with long nano-rods led to more widespread non-uniform doping, largely suppressing the luminescence in silicon solar cells and exhibiting more dark areas (Fig. 32). In contrast, the shorter, 100 nm nano-rod coated wafers contained far fewer defect areas, indicating a more uniform doping profile (Fig. 32c).

It is also problematic to form good metal contacts on nanostructured surfaces. In BSi that contains deep pores, metal cannot completely bridge the gaps between nanostructures, resulting in poor contact (Fig. 33).<sup>220</sup> Moreover, some needle-like nanostructures have "self-cleaning" or super-hydrophobic

Table 2 Comparison of  $J$ - $V$  parameters and efficiencies of BSi and conventional solar cells fabricated under similar conditions

	$V_{oc}$ (mV)	$J_{sc}$ ( $\text{mA cm}^{-2}$ )	FF (%)	Efficiency (%)	Remarks
<b>Oh's p-type solar cells</b> <sup>32</sup>					
Polished silicon	617	26.62	79.6	13.1	Size = 1 $\text{cm}^2$
Pyramid textured silicon with 110 nm $\text{SiN}_x$ coating	624	38.26	78.1	18.6	Size = 1 $\text{cm}^2$
BSi	628	36.45	79.6	18.2	Size = 0.8081 $\text{cm}^2$ ; NREL certified
<b>Repo's n-type solar cells</b> <sup>220</sup>					
BSi #1	628	39.3	75.8	18.7	Size = 4 $\text{cm}^2$ ; diffusion at 890 °C
BSi #2	632	39.2	75.8	18.7	Size = 4 $\text{cm}^2$ ; diffusion at 910 °C
BSi #3	630	38.4	76.1	18.4	Size = 4 $\text{cm}^2$ ; diffusion at 930 °C
Pyramid textured silicon with $\text{Al}_2\text{O}_3/\text{SiN}_x$ stacked coating	631	39.9	75.3	18.9	Size = 4 $\text{cm}^2$ ; diffusion at 910 °C



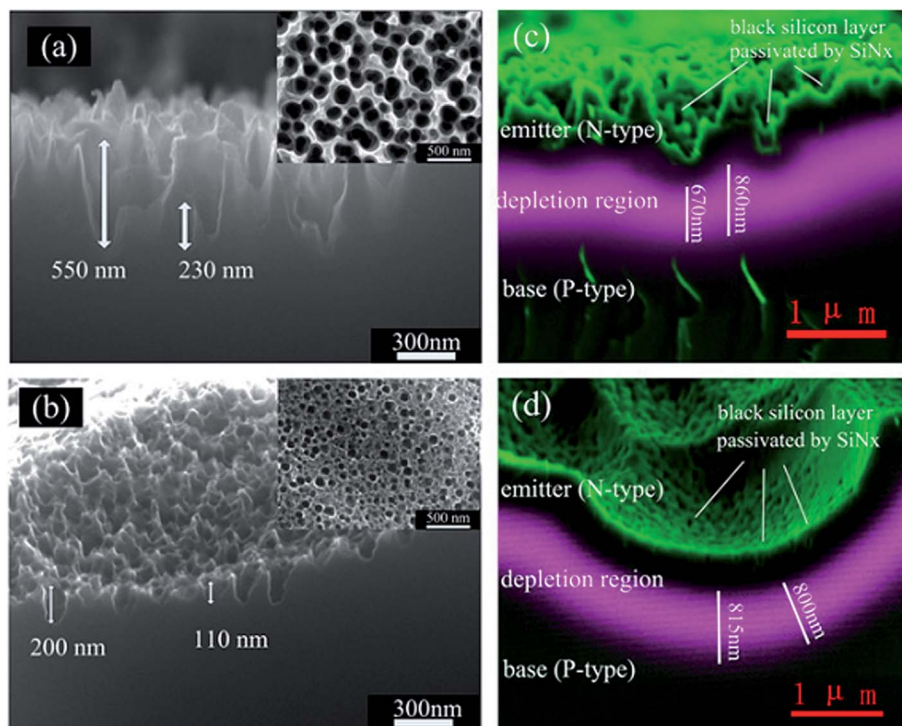


Fig. 31 BSi fabricated with PIII etching performed (a) before doping and (b) after doping; (c) and (d) are cross-section views of EBIC images corresponding to (a) and (b), respectively.<sup>204</sup> Reproduced by permission of Elsevier.

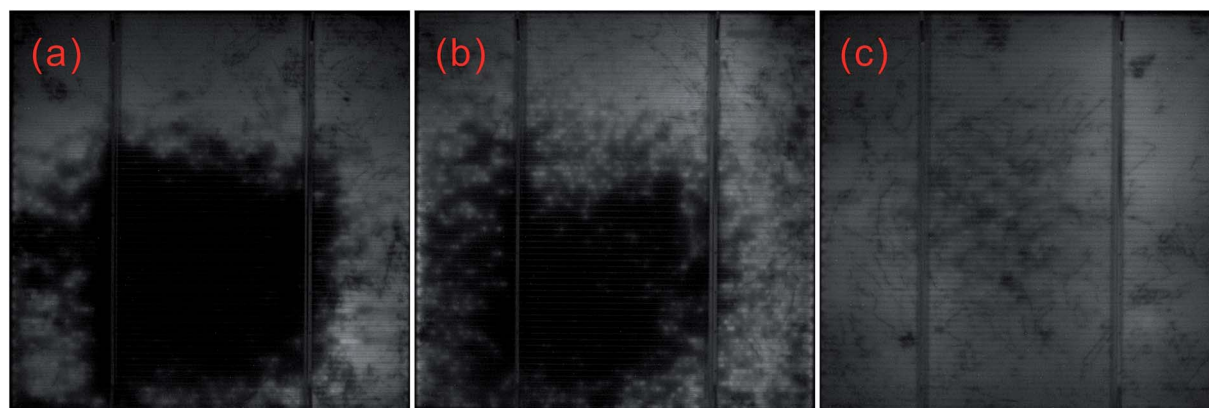


Fig. 32 EL images of BSi solar cells covered by different thickness of nano-rods: (a) 1  $\mu\text{m}$ ; (b) 600 nm; and (c) 100 nm.<sup>209</sup> The black regions contain more defects, and correspond to non-uniform doped areas.

properties, posing significant difficulties for screen printed metal contacts.<sup>25,119</sup>

When a passivation layer, such as  $\text{SiN}_x$ , is deposited onto BSi, the non-uniform thickness of  $\text{SiN}_x$  coating on a roughed silicon surface makes the contact formation even more challenging. For example, in nanostructured valleys with a thick  $\text{SiN}_x$  coating, the silver paste cannot etch through the dielectric layer, thus raising contact resistance.<sup>221,225</sup>

Due to these factors, the overall power conversion efficiency of BSi solar cells is typically low, and the optical gain from BSi often cannot compensate for its electrical losses. In particular, owing to the enlarged surface area and surface defects, heavy

doping, and the associated surface and Auger recombination in BSi emitters, the external quantum efficiency (EQE) of BSi solar cells is especially poor in the short wavelength region.<sup>119,227</sup> Note that short wavelength (or high energy) photons are strongly absorbed in the top layer of a silicon wafer where the BSi resides. This is a typical characteristic of BSi solar cells.

### 3.1.3. Strategies to improve BSi solar cell efficiencies

**Thickness control.** The conflicting optical and electrical demands of BSi require a tradeoff in the optimized morphologies for solar cell applications. A thicker nanostructured layer is required to minimize the surface reflectance, while such a surface structure results in a significantly large surface area for





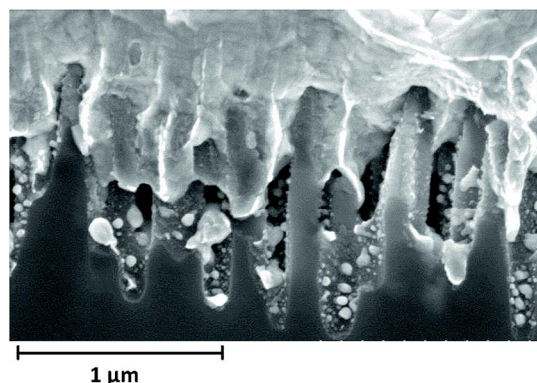


Fig. 33 SEM image of a BSi sample covered by printed front metal contact.<sup>220</sup> Reproduced by permission of Elsevier.

recombination and poses considerable challenges for doping and metal contact formation. In order to attain an improved solar cell performance, the thickness of the nanostructured layer must be tightly controlled.

To this end, several optimal thickness values have been suggested, according to the surface morphologies of the BSi and fabrication technique used. For porous silicon made *via* electrochemical HF etching and stain etching, it has been proposed that a  $\sim 100$  nm thick BSi is required to balance the optical gain against electrical losses.<sup>40,41</sup> In contrast, Lee *et al.* suggested that the optimal depth of RIE nano-structures to achieve the same aim was about 200–400 nm.<sup>126</sup> Using a similar technique, *i.e.*, PIII etching, Zhong *et al.* fabricated a series of solar cells, with different nano-hillock thicknesses from 150 to 600 nm. They showed that the optimal height of their nanostructures was 300 nm.<sup>225</sup> Yuan *et al.* textured their silicon wafers using metal-assisted chemical etching, and found that a thickness around 500 nm yielded the highest solar cell efficiency.<sup>34</sup> In a later study using Ag-assisted chemical etching, Oh *et al.* reported a very high BSi PV efficiency of 18.2%, resulting from BSi nano-structure thicknesses of less than 400 nm.<sup>32</sup> For laser irradiation induced BSi, the surface is micro-structured, and the corresponding texture layer thickness is much larger, of the order of several  $\mu\text{m}$ .<sup>199</sup>

Overall, the optimal thickness for nanostructured BSi layer is several hundreds of nm; this value may be increased for a lower reflectance, provided that the electrical issues are properly addressed, *i.e.*, by applying improved surface passivation and doping strategies.

**Surface cleaning.** BSi formation not only increases the surface area, but also creates a considerable number of defects within the micro- or nanostructured surface; a thorough cleaning or post-etching process is essential to remove these defects. For example, RIE leads to the formation of a  $\sim 50$  nm thick defect layer, which seriously degrades minority carrier lifetime in a solar cell.<sup>227</sup> Kumaravelu and co-workers compared the effective carrier lifetime ( $\tau$ ) of a RIE textured wafer against a planar control wafer using quasi-steady-state photo conductance.<sup>78</sup> In comparison to a large  $\tau$  of  $\sim 400$   $\mu\text{s}$  in the control wafer, the lifetime of the RIE-treated BSi decreases to merely 2–3  $\mu\text{s}$ . After

defect removal by etching in  $\text{HNO}_3$ –HF (50 : 1), its lifetime rises again to  $\sim 36$   $\mu\text{s}$ . The still lower lifetime compared to that of the control wafer was attributed to the increased surface area.<sup>78</sup> Similarly, several other research groups also noticed that a thorough defect removal etching was critical for improving the carrier lifetime in RIE-treated BSi<sup>79,228</sup> and increasing photo-voltaic efficiency in PIII-treated BSi.<sup>222</sup>

For metal-assisted chemical etching, a deep and thorough etching becomes even more critical.<sup>227</sup> First, this etching creates a sub-oxidized surface with a significant number of surface defects. Second, the surface of the chemically etched nano-structures is very rough; on top of the relatively big nano-structures ( $\sim 100$  nm), there are also many small protrusions with a size of  $\sim 2$ –5 nm. These small protrusions have little impact on the optical reflectance of BSi, but cause a substantial increase in its surface area. Third, it is likely that a small trace of metal ions diffuse into silicon during the BSi fabrication; this issue becomes even more vital if a high temperature process (*e.g.* doping) follows the BSi formation.

To address these problems, Algasinger and co-workers performed a modified RCA cleaning, successfully removing the surface defects and gold nanoparticles used for the metal-assisted chemical etching.<sup>227</sup> This cleaning procedure also etched away the small nano-protrusions, which was apparent by the absence of silicon photoluminescence after the cleaning process. The reduced surface area makes the surface passivation much easier to implement. Consequently, upon depositing an  $\text{Al}_2\text{O}_3$  layer onto the BSi surface, using atomic layer deposition (ALD; see Section 4.4), a high carrier lifetime of  $\sim 500$   $\mu\text{s}$  was measured, which is one order of magnitude higher than that in untreated BSi.<sup>227</sup> Similarly, for laser treated micro-structured surfaces, Nayak *et al.* showed that surface cleaning, using NaOH solution rinse followed by an isotropic etching ( $\text{HNO}_3$ – $\text{CH}_3\text{COOH}$ –HF, 30 : 10 : 4), played an important role in the removal of redeposited materials and induced defects, and improved solar cell efficiencies.<sup>199</sup>

**Doping profile control.** The large surface area of BSi means the mass transfer rate of dopants is faster than that of planar silicon. Zhong *et al.* compared that the resistance of a BSi wafer and a planar wafer with the same doping conditions and found that the BSi had a lower resistance, indicating a higher level of doping.<sup>185</sup> In order to control the BSi doping concentration and minimize Auger recombination, Zhong and co-workers showed that a lower doping temperature should be employed. They performed doping at different temperatures (815, 820, 825, 830 and 835  $^\circ\text{C}$ ) in PIII-treated BSi samples, and found that doping at 815  $^\circ\text{C}$  led to the highest EQE in the short wavelength region ( $<550$  nm).<sup>185</sup> Repo *et al.* arrived at the same conclusion by performing doping in RIE-treated BSi samples at 890, 910, and 930  $^\circ\text{C}$ , and discovered that their internal quantum efficiency (IQE) reduced with increasing doping temperature.<sup>220</sup>

Oh *et al.* adopted a different strategy to remove the highly doped regions in BSi. They performed doping at 850  $^\circ\text{C}$  with a subsequent anisotropic tetramethyl-ammonium-hydroxide (TMAH) etch procedure. This etching had two effects: first, the highly doped dead layer on the surface of the BSi was removed; second, the total surface area was reduced, owing to a reduction



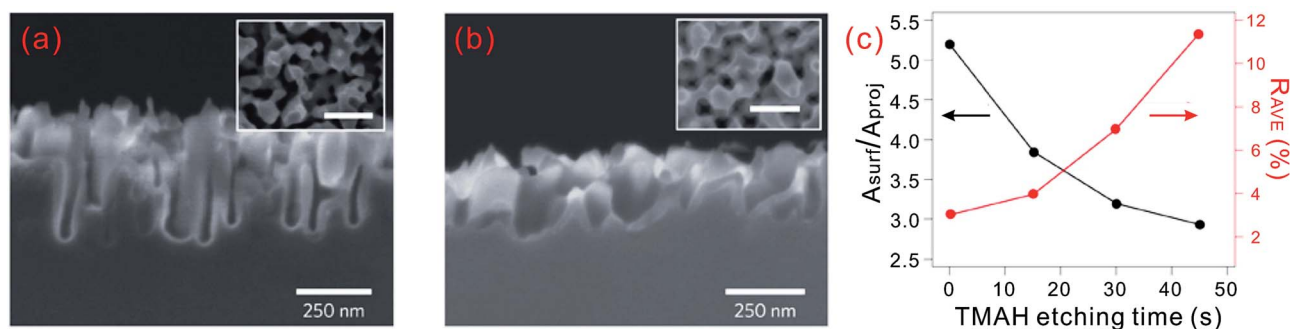


Fig. 34 SEM images of the morphologies of nanostructured silicon surface, fabricated with Ag-assisted chemical etching (a) before and (b) after 30 s of TMAH back-etching. (a) and (b) show the side views of the BSi samples, while the insets represent their top views. The white conformal layer in each side view of the samples show a thermal oxide passivation layer. (c) Ratios of the actual surface area over the projected planar surface area ( $A_{\text{surf}}/A_{\text{proj}}$ ) and the reflectance of the TMAH back-etched BSi, as a function of back-etching time.<sup>32</sup> Reproduced by permission of Nature Publishing Group.

in the nanostructured layer thickness and an enlargement of its surface feature size, but at the expense of increased reflectance (Fig. 34).<sup>32</sup> Based on this method, an excellent BSi solar cell performance with 18.2% efficiency was realized.

Another method to circumvent the doping problem associated with BSi is to dope the wafer prior to texturization. This approach has been successfully adopted by some groups.<sup>33,204</sup> Nevertheless, a high doping concentration at the emitter is likely to change the surface morphology of the resulting BSi. For example, during metal-assisted chemical etching, the surface feature size tends to increase in line with the doping level of the silicon substrate, and the impact of doping on the etching rate is not yet fully understood.<sup>92</sup> Further work is thus required before a wider deployment of this doping strategy can be adopted.

**Other issues.** Owing to the importance of passivation, especially for BSi solar cells, we devote Section 4 of this paper to this topic.

For nanostructures with a surface feature size below the wavelength of visible light, the surface acts as an effective index medium and can be considered to be optically flat. Hence, the normal incident light will penetrate through the wafer without undergoing scattering. In order to increase the optical path length in silicon and to enhance the absorption of long wavelength light, it is important to roughen its back surface for light trapping (Section 5.2).<sup>34</sup> Furthermore, due to the higher surface resistance in BSi compared to that of a planar wafer, it is necessary to reoptimize the metal-grid within BSi solar cells to enhance the charge collection efficiency.<sup>205</sup>

**Strategy summary.** To summarize, current fabrication methods of BSi solar cells are still largely based on conventional solar cell technologies, but a number of modifications are required to improve their cell efficiencies. More specifically, nanostructures of low aspect ratio should be employed to balance the optical gain and electrical losses; thorough removal of surface defects is critical to maximize carrier lifetime; a modified doping strategy should be developed to minimize Auger recombination in the surface layer. Good passivation is important in BSi, due to its enlarged surface area, and the solar

cell architecture requires re-optimization, by methods such as incorporating light trapping structures and applying a finer and denser metal grid for a higher charge collection efficiency. By undertaking these improvements, it is likely that the efficiency of BSi solar cells will advance even further in the near future, with a >20% efficient solar cell concept recently envisioned.<sup>32</sup>

**3.1.4. Cost analysis.** Currently, the power conversion efficiencies of BSi solar cells are generally still lower than those of conventional silicon solar cells. However, BSi holds potential in reducing solar cell fabrication costs *via* several means. Firstly, there is less silicon wastage in BSi fabrication than in conventional wet etching processing. BSi fabrication typically consumes a layer of silicon with a thickness of the order of 100 nm, in comparison to that of 10  $\mu\text{m}$  for conventional wet etching. Secondly, in standard solar cells, a passivation layer, usually composed of dielectrics, such as  $\text{SiN}_x$ ,  $\text{SiO}_2$  and/or  $\text{Al}_2\text{O}_3$ , also functions as an ARC (Section 4), requiring a typical thickness of  $\sim 60$ – $100$  nm. With BSi, Oh *et al.* have suggested that ARC deposition is not required.<sup>32</sup> While this is true, passivation layers are still necessary but could be made thinner (*i.e.*, thickness  $\approx 10$  nm) in BSi solar cells. This represents a cost-advantage and might lead to more freedom in the solar cell design. Similarly, in some solar cell designs, transparent conducting oxide (TCO) acts both as an electrode and as an ARC (Section 3.2.2). In conjunction with BSi, the TCO layer can be optimized solely focussing on achieving optimal transmission and sufficient conductance, potentially reducing costs. Thirdly, it has been proposed that BSi fabrication combines two existing production processes in a conventional solar cell production line, namely texture etching and ARC deposition; simplifying the solar cell fabrication flow potentially reduces production and facility costs.<sup>32,229,230</sup> This inference is largely based on the assumption that no vacuum-based  $\text{SiN}_x$  deposition is required for BSi solar cell production, while thermal oxide is employed for surface passivation. However, it should be mentioned that  $\text{SiN}_x$  are still adopted by some research groups for passivating BSi (Section 4.1). Fourthly, according to current industrial practice, a uniform ARC layer is critical for maintaining the desired aesthetic appearance of solar cells; non-uniform



colored cells can even lead to yield loss. This requirement is likely to be relaxed by incorporating BSi with a unique black appearance, thus improving production yield. Lastly, the black color, typical of BSi solar cells, is aesthetically more appealing for some applications/customers, such as in roof-top photovoltaics.

It is encouraging to note that the first trial-run of BSi solar cells in a production line at Natcore Technology has recently been performed, yielding an efficiency of 15.7%; this compares with an efficiency of 17–19% for conventional reference cells.<sup>229,230</sup> JA Solar, one of the major solar cell manufacturers, has reported an efficiency of 18.3% in their mc-BSi solar cells and introduced a BSi solar cell module rated at 270 W.<sup>231</sup> While the efficiency of BSi solar cells is likely to be further improved *via* process optimization, these results demonstrate that BSi solar cells can be integrated with existing industrial production lines.

Natcore Technology has claimed that solar cell processing cost savings of up to 23.5% per cell could be made with BSi.<sup>229,230</sup> However, this number is likely to be over-optimistic. In a different report, it was estimated that the savings in solar cell processing costs and the overall manufacturing costs could be up to 8% and 3%, respectively, *via* the incorporation of BSi technology.<sup>232</sup>

However, BSi also faces a few technical challenges in both its optical characteristics (Section 3.1.1) and electrical performance (Section 3.1.2). In particular, the optical trapping effect in nanostructured BSi could be very poor, unlike that of microstructured pyramidal structures, which is commonly used in c-Si solar cells. On one hand, the market entry barrier for BSi technology is lower in mc-Si and thin c-Si solar cells, where it is difficult or impossible to perform conventional alkaline etching. On the other hand, light trapping becomes even more critical, particularly for thin c-Si solar cells. Nevertheless, implementing light trapping on thin substrates without wafer breakage is likely to be a challenging task.<sup>233</sup> One alternative option is to increase the feature size of BSi, in order to retain the light trapping function at a slight degradation of surface reflection. Based on the optical modeling of periodic pyramidal-like structures, Sai and co-workers have suggested that a sub-microstructured surface (with period  $>\sim 500$  nm) could retain both low surface reflection and good light trapping effects.<sup>234</sup>

### 3.2. Novel solar cell architectures

**3.2.1. Selective emitter solar cells.** The selective emitter design has been developed to balance different doping requirements, forming a good metal/silicon contact while simultaneously minimizing Auger recombination. On the one hand, a high doping concentration is preferred to reduce the contact resistance between metal fingers and the silicon substrate and form a deep p-n junction to prevent a shunt across this junction due to Ag diffusion. On the other hand, a low doping concentration is critical for limiting Auger recombination. To address these two contradictory requirements, a selective doping profile, featuring a high-doping concentration underneath the metal contacts, and a relatively low doping

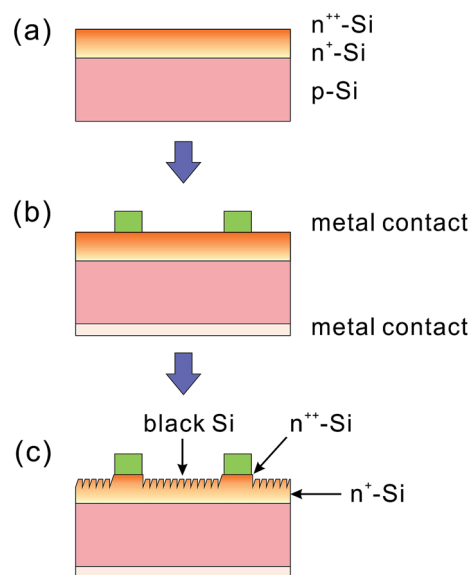


Fig. 35 Typical fabrication procedures to create a selective emitter BSi solar cell: (a) heavy doping; (b) metallization; and (c) back-etching.<sup>41</sup>

concentration in the non-metal covered areas, is adopted in the selective emitter design.<sup>41</sup> The selective emitter is particularly attractive to BSi solar cells, because it remains a challenge to form a good metal/silicon contact on nanostructured silicon surfaces; nonetheless, by using the selective emitter design, the metallic/silicon contact is essentially built on planar silicon (Fig. 35).

In this design, the BSi fabrication leads to the simultaneous formation of a selective emitter, *via* a back-etching process to remove the top heavily-doped dead layer. Existing etching methods have been employed previously in the fabrication of this type of solar cell.<sup>33,40,41,85,205</sup> Since pre-deposited metal fingers may be damaged during the etch process, strategies are used to minimize such effects. One method is to perform a quick etching with a large current density but for a short duration, *i.e.*, 3–4 s using electrochemical etching,<sup>40,41</sup> or performing a rapid stain etching.<sup>205</sup> Another method is to apply a polymeric protection film onto the metal grid during the etching, which can be removed afterwards using acetone.

However, this coating may cover  $\sim 0.1$  mm of silicon next to the metal fingers, and prevent the formation of BSi in those areas.<sup>41</sup> Based on these methods, 25 cm<sup>2</sup> mc-Si selective emitter solar cells coated with porous silicon have been fabricated with  $\sim 14\%$  efficiencies, without applying texturization, passivation, or additional ARC.<sup>41</sup> One additional method to minimize metal contact damage is to employ a gentler etch, such as chemical vapour etching. Rabha *et al.* used this to fabricate a selective emitter solar cell. The power conversion efficiency went from 7.7 to 9.2% after the back-etching process, without any passivation or additional ARC, in 25 cm<sup>2</sup> mc-Si solar cells.<sup>85</sup> In contrast, Wang *et al.* applied SiN<sub>x</sub> passivation on their selective emitter solar cells, formed *via* Ag catalyzed back etching. Here, wax was used to protect the metal contact formation area on the silicon substrate; and the metal fingers were printed after SiN<sub>x</sub>





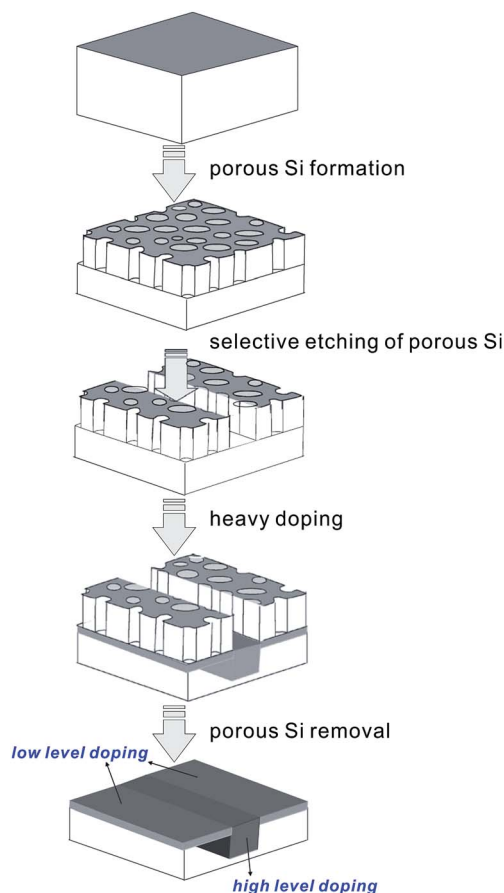


Fig. 36 Fabrication procedures to produce a high-low doping profile using BSi as a sacrificing layer.<sup>235</sup> Adapted by permission of Elsevier.

deposition. Efficiencies up to 16.94% were reported using this methodology.<sup>33</sup>

It is also worth mentioning the experiment of Moon and co-workers, which used porous silicon as a sacrificial layer to create a high-low doping profile for selective emitter solar cells (Fig. 36).<sup>235</sup> They used stain etching to fabricate porous silicon, part of which was selectively removed. The remaining porous silicon acted as a mask to lower the doping concentration in underlying silicon. This mask can be etched away after the doping process. Consequently, a silicon wafer with alternating doping concentrations is fabricated. The resistances in the high- and low-doped regions were measured at 30–35 and 97–474  $\Omega \square^{-1}$ , respectively. A low cost doping source,  $\text{H}_3\text{PO}_4$ -methanol, has been used in this case, instead of  $\text{POCl}_3$  which is

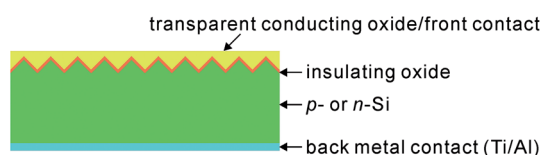


Fig. 37 A schematic of a semiconductor-insulator-semiconductor solar cell.

used commercially. As yet, no solar cells have been fabricated using this type of wafer.

**3.2.2. SIS solar cells.** In semiconductor-insulator-semiconductor (SIS) solar cells, a transparent conducting oxide (TCO) layer is coated on either n-Si or p-Si (Fig. 37).<sup>214</sup> The work function of the TCO layer leads to an inversion in the surface layer of the silicon substrate and forms a p-n junction.<sup>236</sup> Between the TCO layer and the silicon substrate, there is a layer of insulating oxide, typically made of  $\text{SiO}_2$  or  $\text{Al}_2\text{O}_3$  (Fig. 37). This insulating layer should be thick enough to passivate the interface and provide a buffer layer for the lattice mismatch between silicon and TCO, but also thin enough to allow the tunnelling of charge carriers; the ideal thickness is  $\sim 15 \text{ \AA}$ .<sup>236,237</sup> The SIS solar cell offers a few advantages: first, its fabrication process is simple and only requires modest heating; second, the TCO layer is transparent and eliminates the metal shading effect observed in other conventional solar cells; third, the UV response is enhanced due to a spatially abrupt p-n junction; fourth, the TCO layer may also serve as an ARC.<sup>214</sup> However, the AR effect of the TCO film is dependent on wavelength and incident angle. To achieve a broadband anti-reflection effect, BSi can be used to replace the flat silicon substrate in a SIS solar cell.

Füchsel *et al.* fabricated a SIS solar cell using RIE-treated BSi.<sup>214</sup> They sputtered indium-doped tin oxide (ITO) onto the BSi

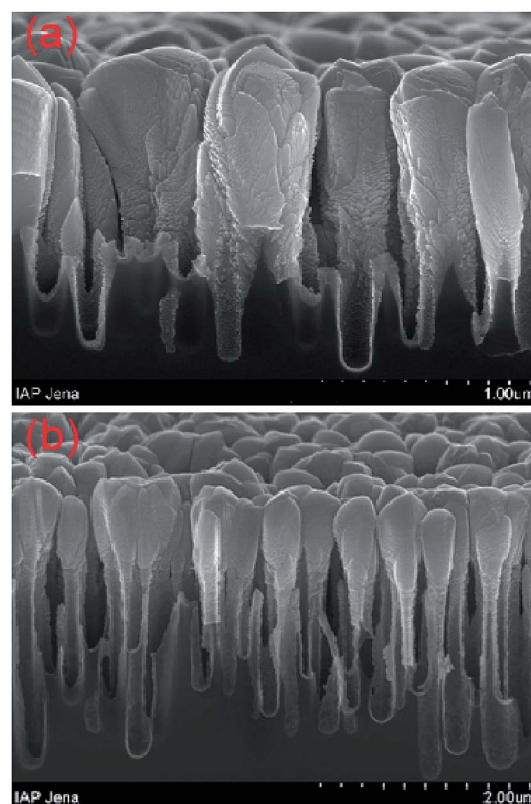


Fig. 38 700 nm Sputtered ITO film-coated BSi with different aspect ratios: (a) BSi composed of nano-rods with diameters  $\approx 100 \text{ nm}$  and lengths  $\approx 500 \text{ nm}$ ; (b) BSi covered by nano-needles with diameters  $\approx 50 \text{ nm}$  and lengths  $\approx 1.7 \mu\text{m}$ .<sup>214</sup> Adapted by permission of SPIE.



to form the front contact. However, the conformality of the ITO film is very poor, especially on high aspect ratio BSi (Fig. 38). The sputtered ITO quickly seals the silicon nano-pores without completely filling them, and merges into a film. Consequently, despite the fact that it has higher  $I_{sc}$  because of a reduced reflectance, the SIS solar cell offers lower  $V_{oc}$ , lower fill factor and overall lower power conversion efficiency (6.6% for low aspect ratio BSi) as compared to a SIS solar cell on a planar silicon substrate (6.9%); this is caused by the poor ITO coverage over BSi as well as the enlarged ITO/BSi interface. The power conversion efficiency of high aspect ratio BSi is even poorer.<sup>214</sup> In addition, the reflectance of the BSi increases from ~1–3% to ~7% after ITO coating, because of the refractive index mismatch between ITO and the BSi.

Instead of sputtering, Otto and co-workers deposited a thin layer (up to 88 nm) of ZnO and Al doped ZnO (ZnO–Al) onto BSi using atomic layer deposition (ALD; see Section 4.4).<sup>238</sup> Excellent TCO conformal coating was achieved for nano-spikes of up to 1  $\mu\text{m}$  high (Fig. 39). At low deposition temperatures (~100 °C), the

grain size in the film was small, and the resistivity relatively high [ $(1.01 \pm 0.22) \times 10^4 \Omega \square^{-1}$  at 120 °C]. At 220 °C, the grain size was enlarged, and surface resistivity dropped to  $60.3 \pm 1.3 \Omega \square^{-1}$ . Upon further increasing the deposition temperature, however, defect formation resulted in an increased resistivity. This temperature dependence was also observed by Steglich *et al.*<sup>239</sup> The thin TCO coating also had little impact on the reflectance of BSi, resulting in a flat and low reflectance below 5% in both the visible and near-IR regions.<sup>238</sup>

Otto *et al.* also fabricated an  $\text{Al}_2\text{O}_3$  film onto a nano-structured BSi sample (with nano-needle diameters of ~150 nm and depths of ~1.7  $\mu\text{m}$ ) using ALD; this film acted as the insulating layer in a SIS cell. The  $\text{Al}_2\text{O}_3$  passivated BSi exhibits an excellent lifetime of 173  $\mu\text{s}$ , comparable to that of planar silicon (446  $\mu\text{s}$ ) at an injection level of  $10^{15} \text{ cm}^{-3}$ .<sup>240</sup> It is expected that these highly conformal insulator and ITO coatings will further boost the efficiency of BSi SIS cells, with an absolute efficiency gain of 1–1.5%, over those made of a planar silicon substrates.<sup>114</sup>

**3.2.3. Tandem solar cells.** A tandem solar cell consists of a stack of two or more solar cells with different bandgaps that are optimized for different parts of the solar spectrum. This potentially allows for a higher solar cell efficiency predominantly due to a reduction of thermalization losses and partly due to a better usage of low energy photons (depending on the bandgap of the bottom solar cell).

When silicon substrates are treated by a fs-laser process in  $\text{SF}_6$ , the surface is micro-structured with hillocks several  $\mu\text{m}$  high. During this process, sulfur atoms diffuse into silicon, forming an intermediate band and extending the absorption spectra of BSi to 2500 nm.<sup>241</sup> This sulfur doping effectively creates an n-Si emitter in the laser-treated area.<sup>242</sup>

Based on this property, a tandem solar cell with two emitters was fabricated by Guenther *et al.*:<sup>241</sup> one is a conventional front emitter and the other is sulfur doped emitter at the rear side of the cell, while the p-substrate acts as a base for both emitters (Fig. 40). In this tandem  $n^+ - p - n^+$  solar cell, the front emitter is responsible for absorbing high energy photons, while the back emitter with an intermediate band absorbs long wavelength photons in the visible and IR regions. The p–n junction at the rear side is shown to generate a  $V_{oc}$  of ~17 mV and a  $J_{sc}$  of ~1  $\text{mA cm}^{-2}$ .

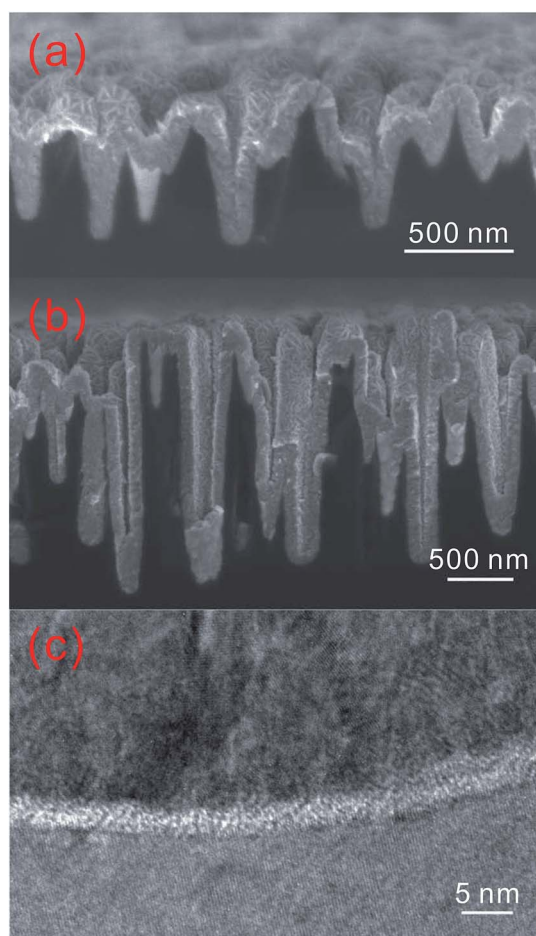


Fig. 39 SEM images of an ALD-deposited ZnO–Al layer sitting on top of (a) a shallow BSi structure and (b) a deep BSi structure, with good conformality; (c) high resolution TEM image confirming the good conformality between ZnO (top), amorphous oxide (middle), and silicon (bottom).<sup>238</sup> Reproduced by permission of John Wiley & Sons, Inc.

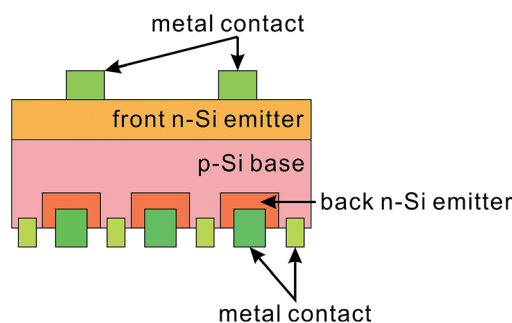


Fig. 40 Tandem  $n^+ - p - n^+$  solar cell using laser treated BSi.<sup>241</sup>



However, the laser treatment and sulfur doping lead to many defects in the substrate. To retain a sufficient sulfur concentration, one is also restricted to low temperature annealing, which removes structural defects but also significantly decreases sulfur concentration and reduces photon absorption in the IR region. Consequently, this tandem cell only affords a power conversion efficiency of 4.5%.<sup>241,242</sup>

### 3.2.4. Other solar cell designs incorporating black silicon.

Rabha and Bessais have adopted a buried contact concept to improve the charge collection efficiency in a mc-Si solar cell. The grooves for depositing metal fingers are formed *via* chemical vapour etching (with  $\text{HNO}_3\text{--HF} > 1/4$ ) through a mask, resulting in the formation of water soluble  $(\text{NH}_4)_2\text{SiF}_6$  powders. The thickness of the grooves in the front and back sides of the cell amounts to 60 and 160  $\mu\text{m}$ , respectively. After typical solar cell fabrication procedures, the front surface is also textured using chemical vapour deposition with a reduced  $\text{HNO}_3\text{--HF}$  ratio to form nearly 500 nm thick porous silicon. The porous silicon affords a weighted reflectance of  $\sim 8\%$  from 450 to 950 nm. Consequently, a solar cell efficiency of 11.8% was reported.<sup>206</sup> This efficiency is relatively low, owing largely to the poor surface passivation by porous silicon.

Grau *et al.* used HF etching to form a porous silicon Bragg reflector with alternating high/low porosities.<sup>243</sup> This reflector is inserted between a thin film silicon cell and a cheap substrate, such as glass. Depending on the porosity and thickness of the porous layer, the reflectivity of the Bragg reflector can top 90% over a broad range, *i.e.*, 750–1100 nm. This enhanced reflection improves light absorption in thin film silicon solar cells and boosts device performance.<sup>244</sup> However, the overall efficiency gain from this Bragg reflector will not be very significant, owing

to its modest overall back-reflecting properties and high back-interface carrier recombination.<sup>243</sup>

### 3.3. Flexible/thin wafer production

Thin film silicon solar cells (thickness  $< 30\ \mu\text{m}$ ) are preferred due to their lower material cost, and relaxed requirements on wafer quality.<sup>245</sup> Owing to its weak mechanical strength, porous silicon has been employed as a separation layer to produce such thin film solar cells in a kerfless porous silicon process (Fig. 41). This method offers a significant advantage over the conventional wafer-sawing technique in reducing silicon wastage.

In a typical fabrication process, porous silicon is first formed by anodization in HF and ethanol or acetic acid solution. A top layer with low porosity (10–20%) and a bottom layer of high porosity (50–70%) are fabricated by adjusting current density and/or changing [HF] during the electrochemical etching.<sup>245</sup> Upon annealing at a high temperature ( $>1000\ ^\circ\text{C}$ ) in a  $\text{H}_2$  environment, the top (low porosity) layer closes its pores and becomes smooth in order to reduce surface energy; this layer subsequently serves as a platform for epitaxial deposition of silicon, typically *via* CVD using  $\text{SiH}_4$ . The epitaxial silicon film can be used to fabricate solar cells, *via* diffusion, metallization and so forth. After device fabrication, the completed solar cell is glued to a cheap foreign substrate, such as glass. In the meantime, annealing of the bottom (high porosity) layer leads to the formation of voids and nano-pillars connecting the top low porosity layer to the initial silicon substrate. This high porosity layer serves as a separation layer, from which the solar cell can be separated from the initial silicon substrate by applying a mechanical force.<sup>245</sup> Based on this concept, many similar processes for fabricating thin film c-Si solar cells have been developed, with differences being mainly in the sequence of

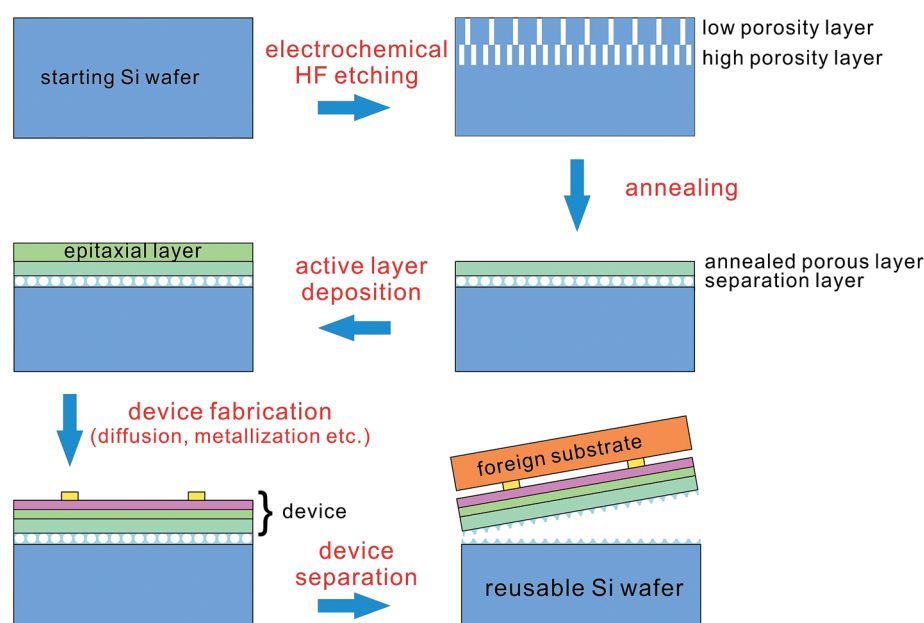


Fig. 41 Using porous silicon as a separation layer to produce thin film silicon solar cells.<sup>245</sup>





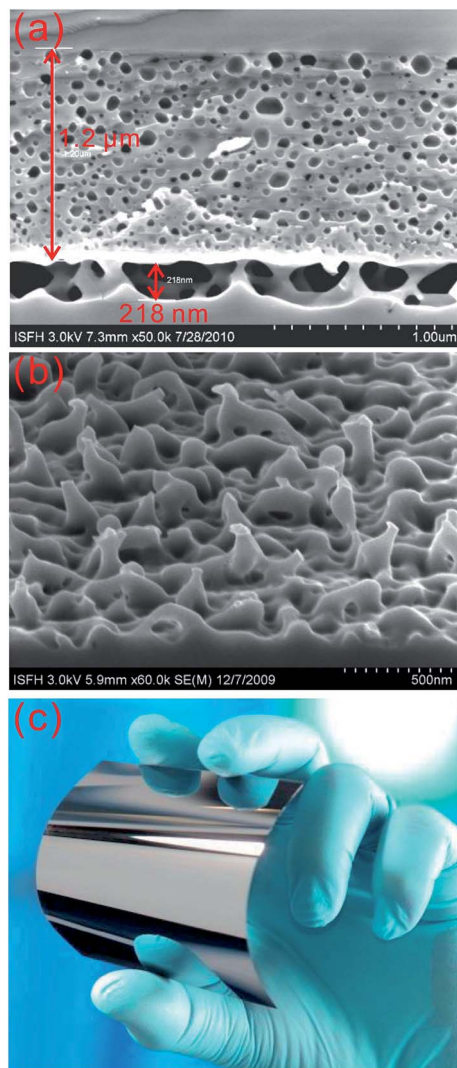


Fig. 42 SEM images of (a) a low porosity silicon layer after epitaxial deposition (top), sitting on top of a silicon substrate (bottom) *via* a high porosity separation layer (middle); and (b) the tilted view of the separation layer after the top layer is lifted off. (c) Photograph of the top layer (30  $\mu\text{m}$  thick,  $9 \times 9 \text{ cm}^2$  large).<sup>246</sup> Adapted by permission of Elsevier.

epitaxial layer deposition, device fabrication and layer separation/transfer.<sup>245</sup>

Using the kerfless porous silicon process, Kajari-Schröder *et al.* produced a 30  $\mu\text{m}$  thick thin and flexible silicon film (Fig. 42). The separation layer used is relatively thin ( $\sim 200 \text{ nm}$ ), and consists of nano-pillars with diameters of  $\sim 40\text{--}100 \text{ nm}$  at the narrowest points after annealing. These nano-pillars cover about 3% of the total substrate area, and can be broken off relatively easily.<sup>246</sup> Radhakrishnan *et al.* demonstrated that the defects in the epitaxial layer created by this porous silicon-based layer transfer process can be effectively controlled, leading to high minority carrier lifetimes exceeding 100  $\mu\text{s}$ .<sup>247,248</sup> Based on this process and a back-contact back-junction cell design,<sup>249</sup> Solexel, Inc. has reported a 20.62% efficiency for a 156 mm  $\times$  156 mm full-square ultrathin ( $\sim 35 \mu\text{m}$  thick) silicon solar cell;

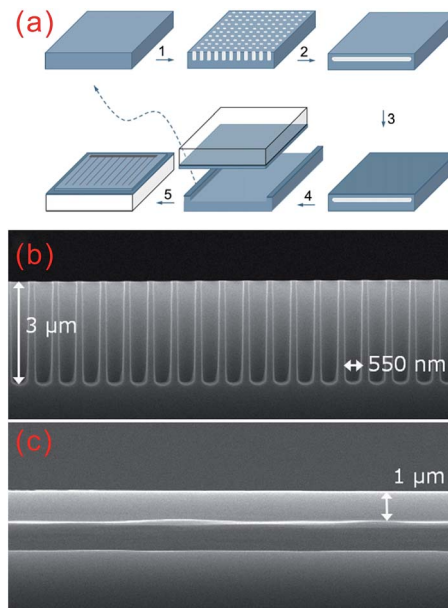


Fig. 43 (a) Fabrication procedures to produce thin silicon films in an epifree process: (1) pore formation; (2) annealing; (3) the first side of the solar cell process; (4) thin film bonding to a low cost substrate; (5) the second side of the solar cell process and reuse of the initial substrate. SEM images of side views of (b) a nano-pore array in a silicon substrate and (c) formation of an extended void and a 1  $\mu\text{m}$  thick overlaying film after annealing the silicon nanopore array.<sup>252</sup> Adapted by permission of Elsevier.

their roadmap indicates a 23.5% cell and a 22% module efficiency target, respectively.<sup>250,251</sup>

Instead of using two layers of porous silicon, Gordon and co-workers fabricated a thin silicon film, by directly annealing a single periodic silicon nano-pore array (Fig. 43a).<sup>252</sup> Currently this pore array is fabricated *via* RIE through a lithographically defined mask, though a low cost nano-imprint defined mask in combination with HF anodization could potentially replace this fabrication technique. Upon annealing for 45–60 min in  $\text{H}_2$  at 1150  $^\circ\text{C}$ , a 3  $\mu\text{m}$  thick pore array (Fig. 43b) is converted to a 1  $\mu\text{m}$  thick film, separated by an extended void from the initial substrate (Fig. 43c).<sup>252</sup> A proof-of-concept solar cell with 4.1% power conversion efficiency has been made, based on this 1  $\mu\text{m}$  thick wafer.<sup>252</sup>

It is also worth mentioning the flexible BSi produced by Mei *et al.*<sup>253</sup> They used laser irradiation to micro-structure the surface of a silicon-on-insulator (SOI) wafer. Following the laser treatment, the  $\text{SiO}_2$  layer in the SOI wafer is etched away, and the isolated top layer functions as a thin and flexible BSi film, with absorption over 97% in the visible region. This flexible BSi can be potentially used for photo-detectors, thermal-electric generation, or solar thermal receivers.<sup>253,254</sup> While used as a solar thermal receiver, this flexible BSi demonstrates good heat transfer and light absorption efficiencies, 13% higher than that of anodized aluminium.<sup>254</sup>

While developing thin silicon films is a trend in the solar industry, there remain many technical challenges for the kerfless porous silicon process, such as improving film quality and reducing wafer crack during the lift-off process.



### 3.4. Gettering

Porous silicon may serve as a gettering agent to remove impurities from bulk silicon during the annealing process, owing to its large surface area and high surface reactivity.<sup>255–258</sup> The optimized annealing temperature varies from 900 to 1000 °C depending on the experimental setup and ambient environment.<sup>255–257</sup> This porous layering can be etched away after the annealing process. Nouri *et al.* showed that this gettering process improved mc-Si quality, with an absolute solar cell efficiency gain of ~1.5% in their case.<sup>257</sup>

The porous silicon can also be used to reduce the impurity level in epitaxial deposited silicon layers (Fig. 42), with a gettering coefficient of  $\sim 10^3$  to  $10^4$  in decreasing metal contamination.<sup>259</sup> Although the presence of this porous layer increases surface area and the associated interfacial recombination rate ( $\sim 250$  times higher than that at the interface of an epitaxial layer and a flat p<sup>+</sup>-Si substrate), this problem can be mitigated *via* introducing an epitaxially grown back surface field on top of the porous silicon; this prevents minority carriers in the epitaxial layer from getting close to the highly recombinative porous interface.<sup>260</sup> Consequently, it has been shown that the surface recombination rate is reduced from  $\sim 2.5 \times 10^5 \text{ cm s}^{-1}$  to  $\sim 1\text{--}2 \times 10^3 \text{ cm s}^{-1}$ , comparable to that on bulk silicon surfaces.<sup>260</sup>

## 4 Passivation methods

Surface passivation is essential for high efficiency solar cells.<sup>261</sup> For BSi, it is believed that the surface nanostructures provide good passivation as their feature sizes decrease to a few nm.<sup>39</sup> This is because the bandgap of the nanostructured silicon is significantly higher than bulk silicon due to quantum confinement effects, and minority carriers generated in the bulk are thus prevented from getting close to the surface owing to a bandgap offset. Indeed, porous silicon produced *via* stain etching and electrochemical HF etching exhibits  $\sim 20\%$  higher lifetime ( $\tau$ ) than unpassivated planar silicon. However, the absolute value of  $\tau$  passivated by porous silicon amounts to only  $\sim 3.5 \mu\text{s}$ .<sup>41</sup> This value is far less than that can be obtained by using dielectric passivation materials (*i.e.*, SiN<sub>x</sub>, SiO<sub>2</sub>, and Al<sub>2</sub>O<sub>3</sub>) or a-Si, when ms lifetimes are achievable. Consequently, although porous silicon passivated BSi solar cells demonstrate higher efficiencies than un-passivated solar cells, their absolute values are on the lower side ( $\sim 10\text{--}14\%$ ).<sup>84,89</sup>

As the feature size of nanostructures increases, *i.e.*, to several hundreds of nm, the minority carrier mirror effect becomes very weak. In addition, the surface area of nanostructured BSi is significantly larger than that of planar silicon. Hence, good passivation becomes vital for BSi solar cells. In this section, we will examine the characters of the four most popular passivation materials used in silicon solar cells, including SiN<sub>x</sub>, a-Si, SiO<sub>2</sub> and Al<sub>2</sub>O<sub>3</sub>; and review their application in passivating BSi. Our discussion will focus on Al<sub>2</sub>O<sub>3</sub> fabricated *via* atomic layer deposition (ALD), due to its excellent conformality to nanostructured surfaces and increasing popularity in solar cell applications.

### 4.1. SiN<sub>x</sub>

SiN<sub>x</sub> is currently the industrial standard used to passivate the n-type emitter of p-type silicon wafer solar cells. It is deposited onto silicon using ammonia and silane mixtures through plasma-enhanced CVD (PECVD) at  $\sim 400^\circ\text{C}$ .<sup>262</sup> The relative weight of silicon and nitrogen can be adjusted by changing the flow rate of ammonia and silane. N<sub>2</sub> may also be added into the gas mixture in order to lower the silicon content, improve the etching rate of SiN<sub>x</sub> (for forming the metal contact), minimize its UV light absorption, and maintain a high minority time.<sup>263</sup> In Si-rich SiN<sub>x</sub>, the passivation is mainly governed by chemical passivation, *i.e.*, by reducing the number of surface dangling bonds. As the nitrogen content increases, a high density of fixed positive charge ( $Q_f = \sim 10^{12} \text{ cm}^{-2}$ ) develops.<sup>264,265</sup> This positive interfacial charge is beneficial for passivating n-Si through field effect passivation. Essentially, an accumulation layer is created near the silicon surface due to the positive charge; thereby reducing the minority carrier concentration at the surface.<sup>264</sup>

Owing to its good chemical passivation and positive interfacial charge, SiN<sub>x</sub> passivation works for n-Si of arbitrary doping concentrations, and lightly doped p-Si; but it is less ideal for heavily doped p-Si.<sup>266</sup> Based on SiN<sub>x</sub> passivation, very low surface recombination rate of 6 and  $15 \text{ cm s}^{-1}$  have been reported for  $1.5 \Omega \times \text{cm}$  n-Si and p-Si, respectively.<sup>267–269</sup> However, under low illumination conditions, the passivation effect in lightly p-doped wafers may degrade due to additional bulk recombination in the inversion layer close to the surface.<sup>265</sup>

Since solar cell emitters are always heavily doped and SiN<sub>x</sub> does not work for p<sup>+</sup>-Si, its passivation is limited to p-type solar cells (with n<sup>+</sup> emitters). In addition to its role of passivation, a quarter-wavelength thick SiN<sub>x</sub> film also acts as an AR layer and is commonly used in commercial solar cells. SiN<sub>x</sub> has been employed for passivating n<sup>+</sup> BSi emitters fabricated *via* various processes, such as metal-assisted chemical etching,<sup>33,207</sup> RIE,<sup>115</sup> and PIII etching.<sup>225,270</sup> It greatly improved BSi solar cell efficiency from 11.5 to 14.9% in Liu's experiments.<sup>207</sup> However, since SiN<sub>x</sub> is often deposited *via* PECVD, its surface conformality is relatively poor for high aspect ratio BSi (Fig. 44a).

It has been reported that the passivation effect of SiN<sub>x</sub> improves as its film thickness increases, but saturates when its film thickness exceeds  $\sim 20 \text{ nm}$  for a planar silicon wafer.<sup>271,272</sup> Nevertheless, Liu *et al.* noticed that in the case of BSi, thicker SiN<sub>x</sub> film afforded better passivation. Unfortunately, a thick SiN<sub>x</sub> film also increases serial resistance for printed metal contacts. Consequently, a trade-off is required and a  $77 \text{ nm}$  thick SiN<sub>x</sub> offers a higher solar cell efficiency than those of  $44$  and  $100 \text{ nm}$  thick in Liu's experiments.<sup>270</sup>

### 4.2. Amorphous silicon (a-Si)

a-Si can be deposited *via* PECVD at a relatively low temperature between  $200$  and  $250^\circ\text{C}$ .<sup>273</sup> It forms a good interface to c-Si, thus affording strong chemical passivation, and can be used to passivate both p- and n-Si in conjunction with hydrogen annealing.<sup>273–276</sup> Silicon surface recombination rates as low as  $2 \text{ cm s}^{-1}$  have been demonstrated with a-Si passivation.<sup>264</sup> While employed in solar cells, minority carrier lifetimes greater than  $5$



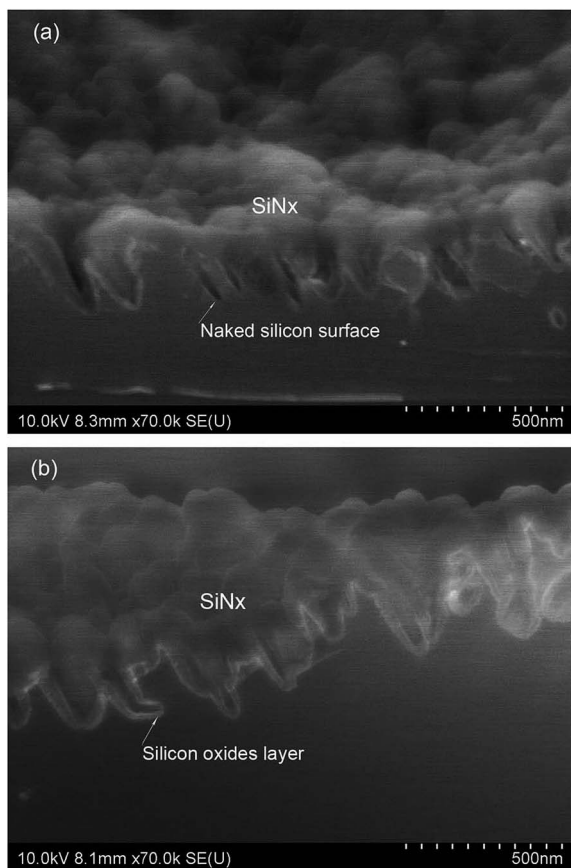


Fig. 44 SEM images of BSi coated with (a) 80 nm SiN<sub>x</sub>; and (b) 20 nm thermal oxide and 60 nm SiN<sub>x</sub>.<sup>207</sup> Reproduced by permission of John Wiley & Sons, Inc.

ms and  $V_{oc}$  up to 738 mV have been demonstrated with post-deposition plasma-hydrogenation and annealing.<sup>277</sup> However, a-Si strongly absorbs in the visible region of the solar spectrum, and is not thermally stable.<sup>266,274–276</sup> Owing to the use of PECVD, the conformality of a-Si on BSi is likely to be problematic. Therefore, to date, no a-Si passivation method has been reported.

#### 4.3. SiO<sub>2</sub>

Thermal oxide provides very good chemical passivation, reducing silicon interfacial defects to  $10^9$  to  $10^{10}$  eV<sup>-1</sup> cm<sup>-2</sup>.<sup>264,265,278</sup> It also contains a small amount of positive fixed charge with a density of  $10^{10}$  to  $10^{11}$  cm<sup>-2</sup>, affording a weak field passivation effect.<sup>264,265</sup> It can be used to passivate either n- or p-Si of arbitrary doping concentrations with excellent surface conformality. However, the positive interfacial charge implies that the passivation effect on a p<sup>+</sup> emitter is likely inferior than that on an n<sup>+</sup>-emitter.

Nevertheless, with the “aneal” process, Kerr and co-workers successfully passivated p<sup>+</sup> wafers using thermal oxide.<sup>279</sup> Here, a layer of Al was pre-deposited on an oxidized wafer before annealing. During the subsequent annealing (at 400 °C for 30 min in forming gas), the oxidization of Al with water residue in the oxide layer released atomic hydrogen, which effectively

passivates the SiO<sub>2</sub>/Si interface. The remaining Al can be etched away after this process. *Via* this process, very low surface recombination rates of 2 and 12 cm s<sup>-1</sup> were reported on 1.5 Ω × cm n-Si and 1 Ω × cm p-Si wafer, respectively.<sup>279</sup> The aneal process also allowed Zhao *et al.* to attain 24% power conversion efficiency in their PERL cell, by increasing minority carrier lifetime from 14 μs in the as-deposited SiO<sub>2</sub> state to 400 μs.<sup>280</sup>

The primary drawback of thermal oxide passivation concerns its high processing temperature (850–1100 °C). Consequently, only c-Si with low impurities is suitable for this process.<sup>281</sup> In mc-Si, such a high processing temperature leads to the diffusion of impurities from grain boundaries to the bulk; thermal oxide is thus not preferred for mc-Si, owing to both performance and cost/throughput considerations.<sup>263</sup> Moreover, the dopants in the emitter are drawn into the oxide layer, changing the doping profile and potentially degrading solar cell efficiencies during high temperature thermal oxidation in some cases.<sup>224</sup>

Various strategies have been developed to circumvent this high temperature problem. For example, SiO<sub>x</sub> can be deposited *via* low temperature PECVD. This layer affords poorer passivation performance in comparison to SiO<sub>2</sub>, but its properties can be improved by capping amorphous SiN<sub>x</sub> (a-SiN<sub>x</sub>) or Al<sub>2</sub>O<sub>3</sub> layers.<sup>264</sup> Alternatively, one may use low-temperature wet oxidation (at ~800 °C) to replace high-temperature dry oxidation.<sup>282</sup> Natcore Technology has also developed a proprietary liquid-phase SiO<sub>2</sub> deposition technique at room temperature in a reactive solution containing H<sub>2</sub>SiF<sub>6</sub>, SiO<sub>2</sub> powder, and H<sub>2</sub>O.<sup>210</sup>

Owing to its good surface conformality, SiO<sub>2</sub> has been employed to passivate n<sup>+</sup> emitters in BSi.<sup>32,34,79</sup> In the record high 18.2% efficiency BSi solar cell, Oh *et al.* used thermal oxide to passivate their nanostructured silicon surface (Fig. 34).<sup>32</sup> Liu and co-workers attempted to improve the thermal oxidation process for BSi solar cells.<sup>224</sup> They compared two different thermal oxidation processes: one used low O<sub>2</sub> pressure but a high processing temperature [1 atmospheric pressure (atm) at 800 °C for 20 min]; the other employed high O<sub>2</sub> pressure and a low processing temperature (30 atm at 450 °C for 20 min). Here, the EQE of the low-temperature processed sample was higher in the short wavelength region (350–700 nm) and comparable in the longer wavelength region compared with the high-temperature processed sample. Consequently, the low-temperature processed sample exhibited a higher power conversion efficiency of 12.22%, *versus* 11.47% for the high-temperature processed sample.<sup>224</sup> Yuan and co-workers employed Natcore's liquid phase deposition technique to grow a thin layer of SiO<sub>2</sub> (thickness < 10 nm) to passivate BSi.<sup>210</sup> This SiO<sub>2</sub> layer demonstrated better surface passivation quality than thermal oxide (thickness = 25–30 nm) according to minority carrier lifetime analysis and led to higher solar cell spectral response at short wavelengths (~350–700 nm). Consequently, a 16.4%-efficient BSi solar cell, passivated by the liquid phase deposited SiO<sub>2</sub> layer, has been fabricated.<sup>210</sup>

#### 4.4. Al<sub>2</sub>O<sub>3</sub>

Al<sub>2</sub>O<sub>3</sub> is an excellent surface passivation dielectric material, and can be deposited on silicon *via* several methods, such as ALD,





PECVD and pulsed laser deposition.<sup>264,283</sup> In relation to BSi, our subsequent discussion will focus on  $\text{Al}_2\text{O}_3$  deposited *via* ALD only, owing to its excellent surface conformality on complex surface morphologies.

During ALD growth of  $\text{Al}_2\text{O}_3$ , an aluminium precursor, typically  $\text{Al}(\text{CH}_3)_3$ , and an oxidative agent, typically  $\text{H}_2\text{O}$ , are alternatively introduced into the reaction chamber.<sup>281</sup> The deposition of  $\text{Al}(\text{CH}_3)_3$  or  $\text{H}_2\text{O}$  is a self-limiting process; that is, a monolayer of these molecules covers the entire substrate surface, upon which further deposition of the same type of molecules is prevented. Hence, by sequentially depositing an  $\text{Al}(\text{CH}_3)_3$  or  $\text{H}_2\text{O}$  monolayer, their reactions lead to the formation of an atomic layer of  $\text{Al}_2\text{O}_3$  in each cycle. Consequently, excellent thickness and uniformity control, and great conformality over large area, can be achieved.<sup>264</sup>

In addition to  $\text{H}_2\text{O}$ , one additional oxidation source, such as  $\text{O}_3$  plasma or  $\text{O}_2$  plasma is often added to the chamber. Based on this additional oxidation source, ALD is classified as thermal ALD (either using  $\text{H}_2\text{O}$  or  $\text{O}_3$ ) or plasma-assisted ALD (PE-ALD, when  $\text{O}_2$  plasma is in use).<sup>264,281</sup> The deposition rate of PE-ALD is  $\sim 30\%$  faster in comparison to that of thermal ALD, owing to more active oxygen radicals and a shorter purging time.<sup>264,266,281</sup> PE-ALD also offers lower impurity levels, and better quality, especially at low temperatures<sup>264</sup> and provides good passivation, which is almost independent of temperature, in the range 200–300 °C.<sup>281</sup> Moreover, Hoex *et al.* found that PE-ALD outperformed thermal ALD upon annealing in  $\text{N}_2$  for 30 min at 425 °C, primarily because the former generated a higher fixed negative charged density ( $Q_f$ ), *i.e.*,  $7 \times 10^{12}$  in contrast to  $10^{12} \text{ cm}^{-2}$  for the latter, leading to enhanced field passivation.<sup>281</sup> An improved annealing strategy for thermal ALD is required to minimize this performance gap.

Post-annealing is critical to improving the passivation effect of  $\text{Al}_2\text{O}_3$ . During Hoex's PE-ALD experiment, the thickness of interfacial  $\text{SiO}_x$ , sandwiched between amorphous  $\text{Al}_2\text{O}_3$  and Si, increased from  $\sim 1.2$  to  $\sim 1.5$  nm upon annealing. This inflated  $\text{SiO}_x$  layer was responsible for both reduced interfacial defects with better coordination of Si and O and selective hydrogenation, as well as increased  $Q_f$ .<sup>265,266,284,285</sup> In Lei's thermal ALD experiment, a rapid annealing at 550 °C increases the interfacial

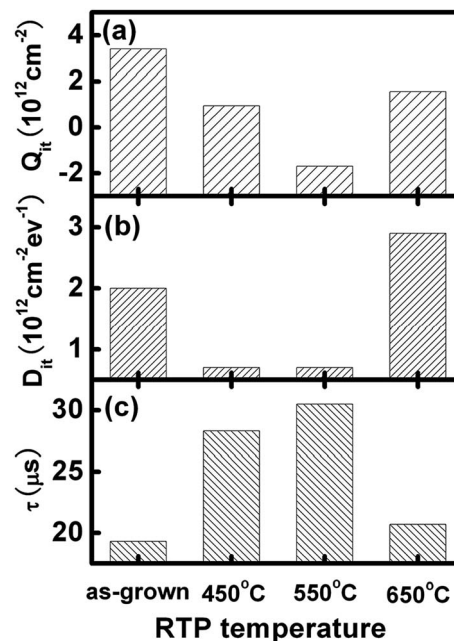


Fig. 46 Evolution of (a) interfacial fixed charge density,  $Q_{it}$ ; (b) density of interfacial states,  $D_{it}$ ; and (c) effective carrier lifetime,  $\tau$ , for  $\text{Al}_2\text{O}_3$  passivated p-Si wafers annealed at different temperatures *via* rapid thermal processing (RTP). Reproduced with permission from ref. 286. Copyright 2011, AIP Publishing LLC.

$\text{SiO}_x$  thickness from  $\sim 1.5$  to  $\sim 4.0$  nm and greatly minimizes the interfacial defects (Fig. 45).<sup>286</sup> Moreover,  $Q_f$  switches from positive to negative, offering improved field effect passivation to p-Si. Consequently, the minority carrier lifetime increases from  $\sim 19$  to  $\sim 31 \mu\text{s}$  in a moderately doped p-Si wafer ( $1.25 \times 10^{15} \text{ cm}^{-3}$ ) upon annealing (Fig. 46). It is also interesting to note that the annealing temperature plays an important role in the overall passivation result. In Liu's case, the results of 450 and 650 °C annealing are less ideal and even afford positive interfacial charges.<sup>286</sup> The positive  $Q_f$  is most likely a process-dependent result. In contrast, Hoex reported that  $Q_f$  was always negative for an  $\text{Al}_2\text{O}_3$  film after annealing, regardless of the deposition method.<sup>265</sup>

The interfacial defect density between  $\text{Al}_2\text{O}_3$  and Si is estimated to be  $\sim 10^{11} \text{ eV}^{-1} \text{ cm}^{-2}$ ,<sup>265</sup> which is higher than that offered by thermal oxide ( $10^9$  to  $10^{10} \text{ eV}^{-1} \text{ cm}^{-2}$ ). However,  $\text{Al}_2\text{O}_3$  affords a stronger field effect passivation due to a larger  $Q_f$ , up to  $\sim 10^{13} \text{ cm}^{-2}$ .<sup>265,266,281</sup> This value is much higher than that in  $\text{SiO}_2$ , which amounts to  $\sim 10^{10}$  to  $10^{11} \text{ cm}^{-2}$ . Since the field effect passivation roughly scales with  $Q_f^2$ , it is about four orders of magnitude higher in  $\text{Al}_2\text{O}_3$  than in thermal oxide; this effect relaxes the requirement on interfacial surface defects in  $\text{Al}_2\text{O}_3$ .<sup>265</sup> Consequently, very low surface recombination velocity of  $2 \text{ cm s}^{-1}$  and  $13 \text{ cm s}^{-1}$  has been reported for low resistivity n-Si and p-Si wafers, respectively.<sup>266</sup> These values are comparable to those offered by state-of-the-art thermal oxide passivation.

$\text{Al}_2\text{O}_3$  offers excellent surface passivation effects. A good level of passivation can be maintained down to  $\sim 5$  and  $\sim 10$  nm of  $\text{Al}_2\text{O}_3$  for PE-ALD and thermal ALD, respectively.<sup>264</sup> Owing to the

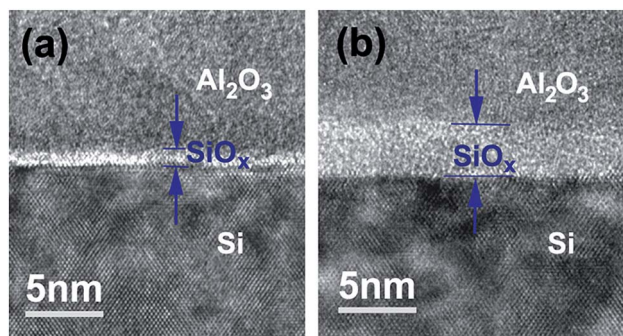


Fig. 45 TEM images of  $\text{Al}_2\text{O}_3$ /Si interfaces (a) in the as-deposited state; and (b) after 550 °C rapid thermal annealing. Reproduced with permission from ref. 286. Copyright 2011, AIP Publishing LLC.

negative built-in interfacial charge,  $\text{Al}_2\text{O}_3$  is effective in passivating p-Si and has been used to passivate the rear surface of a  $\text{n}^+\text{p}$  solar cell.<sup>287</sup> In cases of passivating  $\text{p}^+$ -emitters,  $\text{Al}_2\text{O}_3$  outperforms forming gas annealed thermal oxide, a-Si, and as-deposited a-SiN<sub>x</sub><sup>265,288</sup> and has been successfully incorporated on the emitter of a  $\text{p}^+\text{n}$  solar cell.<sup>289</sup> Moreover, Black and co-workers have demonstrated that the passivation effects at the Si/ $\text{Al}_2\text{O}_3$  interface are independent of the boron dopant concentration in the range from  $9.2 \times 10^{15}$  to  $5.2 \times 10^{19} \text{ cm}^{-3}$ .<sup>290</sup>

Because of its relatively low interfacial defect density (chemical passivation),  $\text{Al}_2\text{O}_3$  has also been employed to passivate  $\text{n}^+$ -emitters and offers good performance, although  $\text{SiO}_2/\text{Al}_2\text{O}_3$  stacks without negative charges are likely preferable.<sup>202,264,291</sup>

Similar to SiN<sub>x</sub>,  $\text{Al}_2\text{O}_3$  (with a refractive index of  $\sim 1.60$ – $1.65$  for 2 eV light<sup>266</sup>) can also serve as an AR layer. With 70 and 100 nm of  $\text{Al}_2\text{O}_3$  coated on pyramidal structured silicon wafers, the averaged reflectance can be reduced from 14.2% to 4.2 and 2.8%, respectively.<sup>292</sup>

The ALD technique used for  $\text{Al}_2\text{O}_3$  growth affords excellent thickness control, good step coverage and conformality, low defect density, high uniformity over a large area, good reproducibility, and low deposition temperature.<sup>202</sup> Its properties are not affected by UV-radiation.<sup>281</sup> Since the solar cell industry is predicted to shift to n-type silicon photovoltaics (with  $\text{p}^+$ -emitters) soon, due to their relative insensitivity to various impurities and defects compared to p-type solar cells,  $\text{Al}_2\text{O}_3$  is likely to play a more important role in this industry with its particular strengths in passivating  $\text{p}^+$ -emitters and affording favourable optical properties.

The primary drawback of ALD  $\text{Al}_2\text{O}_3$  is related to its slow growth rate, which renders an  $\text{Al}_2\text{O}_3$  film thickness of  $\sim 0.5$ – $1.5$  Å per cycle, at several seconds per cycle. To address this concern, several industrial processes have been developed.<sup>264</sup> One method relies on batch-ALD, during which multiple wafers are processed simultaneously, and a throughput rate of  $>3000$  solar cells per hour has been realized. Experimental results show that the passivation effect from industrial-scale ALD processes is comparable to those obtained at a wafer scale.

ALD  $\text{Al}_2\text{O}_3$  is an attractive BSi passivation option, owing to its excellent conformality on nanostructures (Fig. 47) and has been investigated by several research groups.<sup>202,220,228,240,293–295</sup> Otto *et al.* fabricated three BSi samples, using RIE on low resistivity p-Si wafers, and passivated them with 100 nm ALD  $\text{Al}_2\text{O}_3$

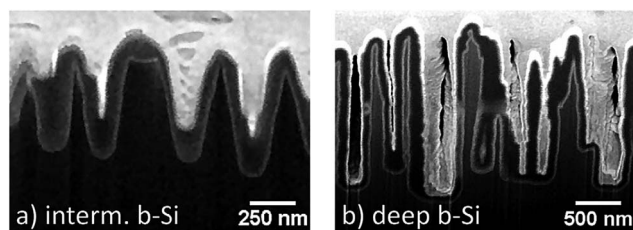


Fig. 47 SEM images of BSi samples coated by  $\sim 100$  nm ALD  $\text{Al}_2\text{O}_3$  (dark grey). A protection Pt film (white) is deposited before the cross-section preparation. Reproduced with permission from ref. 228. Copyright 2012, AIP Publishing LLC.

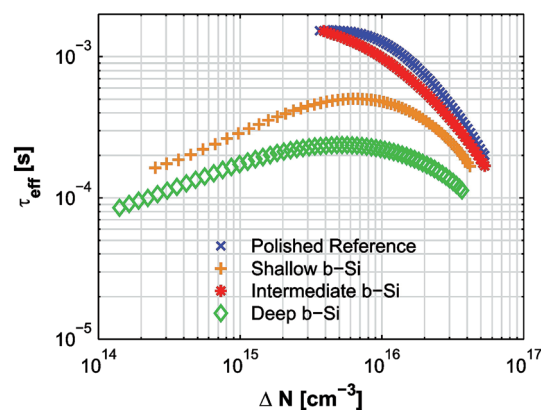


Fig. 48 Injection level dependent carrier lifetime of three BSi samples with different aspect ratios and a reference planar wafer. All samples are passivated with 100 nm  $\text{Al}_2\text{O}_3$ , and annealed in low-pressure Ar ambient at  $425^\circ\text{C}$  for 30 min. Reproduced with permission from ref. 228. Copyright 2012, AIP Publishing LLC.

(Fig. 47).<sup>228</sup> The heights of these nanostructures were 500, 600, and 1700 nm, respectively, affording aspect ratios of 3, 4 and 10. Otto and co-workers showed that good passivation, comparable to that on planar wafers, was realized on the optimized BSi with an intermediate aspect ratio (Fig. 48). A very low surface recombination velocity, less than  $13 \text{ cm s}^{-1}$ , has been measured, leading to an effective carrier lifetime in the ms range. The relatively poor performance of the other two BSi samples is likely caused by ion-induced surface damages during RIE, which was not thoroughly cleaned.

In another independent study on low-resistivity p-Si wafers, Repo *et al.* confirmed that the lifetime of BSi was in the ms range and comparable to that of planar wafers with ALD  $\text{Al}_2\text{O}_3$  passivation.<sup>294</sup> Repo and co-workers also noticed that the lifetime of  $\text{Al}_2\text{O}_3$  passivated wafers was one order of magnitude longer than that with thermal oxide passivation. In addition to the good passivation properties, both  $\text{Al}_2\text{O}_3$  and thermal oxide further improved the reflectance of BSi, down to less than 1%; and  $\text{Al}_2\text{O}_3$  offered a slightly better optical performance than thermal oxide. This difference was attributed to two factors: their refractive indices are different; and the nanostructure morphologies may be changed slightly during thermal oxidation.<sup>294,295</sup>

Based on ALD  $\text{Al}_2\text{O}_3$  passivation, Repo *et al.* fabricated an n-type PERL (passivated emitter with rear locally diffused) cell with BSi on the front  $\text{p}^+$ -emitter side. This solar cell demonstrated a record high efficiency of 18.7%.<sup>220</sup>

ALD  $\text{Al}_2\text{O}_3$  passivation has also been applied to a p-type BSi solar cell with an  $\text{n}^+$ -emitter by Wang *et al.*<sup>202</sup> In their case, good chemical passivation improved the carrier lifetime from  $1.05 \mu\text{s}$  to  $18.1 \mu\text{s}$ , leading to a high power conversion efficiency of 18.2%.

#### 4.5. Stacked layers

Every dielectric passivation material has limitations. For example, the positive fixed charge in SiN<sub>x</sub> degrades its passivation effect on a  $\text{p}^+$ -emitter; and the performance of  $\text{Al}_2\text{O}_3$  is less



ideal on an  $n^+$ -emitter. A stacked dielectric layer, however, can be employed to avoid these drawbacks. For instance, a  $\text{SiO}_2/\text{Al}_2\text{O}_3$  stacked layer removes the negative fixed charge associated with  $\text{Al}_2\text{O}_3$ , and offers an improved passivation performance on  $n\text{-Si}$ .<sup>264</sup>

In addition to tuning the fixed interfacial charge density, a stacked layer may also boost chemical passivation, such as in the case of  $\text{SiO}_2/\text{SiN}_x$ . In this stacked passivation layer, a  $\text{SiO}_2$  layer greater than 10 nm is required to provide a good interface to silicon; during the deposition of  $\text{SiN}_x$ , further hydrogenation helps to passivate the dangling bonds at the  $\text{Si}/\text{SiO}_2$  interface, leading to an impressive passivation effect, comparable to that offered by the alneal process (Fig. 49).<sup>263</sup> The  $\text{SiO}_2/\text{SiN}_x$  stack also greatly improves the thermal stability of the dielectric layer; this feature is critical for solar cell fabrication, since solar cells have to go through a few high temperature processes. Nevertheless, thermal oxide in this stacked layer is fabricated at high temperature and is not desirable.

To avoid high-temperature thermal oxide growth, Dingemans *et al.* used PECVD to grow a  $\text{SiO}_x/\text{SiN}_y$  stack and passivate a low resistivity  $p\text{-Si}$  wafer.<sup>296</sup> They reported a low surface recombination velocity ( $<11\text{ cm s}^{-1}$ ). Duttagupta *et al.* further extended this technique to passivate a  $p^+$ -emitter. They deposited a stack of 15 nm  $\text{SiO}_x$  and 70 nm  $a\text{-SiN}_x$ . Upon annealing, the interfacial fixed charge density amounts to  $\sim 10^{11}\text{ cm}^{-2}$  and the interface defect density is reduced to  $\sim 3 \times 10^{10}\text{ V}^{-1}\text{ cm}^{-2}$ ; consequently, a low  $J_{0e}$  of  $\sim 25\text{ fA cm}^{-2}$  was measured. This study shows that a modest positive fixed charge density of  $\sim 10^{11}\text{ cm}^{-2}$  can be tolerated for passivating  $p^+$  emitters in the presence of excellent chemical passivation.<sup>297</sup> This stacked film also exhibits an AR effect, reducing the weighted reflectance in the range 300–1000 nm to  $\sim 2\%$ .

One potential concern for  $\text{SiO}_2/\text{SiN}_x$  stacked layers regards UV radiation induced damages. The defects at the  $\text{Si}/\text{SiO}_2$  interface can be created following the injection of energetic electrons from the silicon substrate to  $\text{SiO}_2$  under UV radiation.

Typically, un-concentrated sunlight is not sufficiently energetic to cause such damage. However, with  $\text{SiN}_x$  coating which introduces a positive charge density of  $\sim 2 \times 10^{12}\text{ cm}^{-2}$ , a defect can be created by a much lower energy photon, *i.e.*, 3.95 eV (314 nm); such photons are abundantly available in the solar spectrum.<sup>298</sup>

Stacked  $\text{Al}_2\text{O}_3/\text{SiN}_x$  layers have also been employed for both passivation and AR effects on  $p\text{-Si}$ . In particular,  $\text{Al}_2\text{O}_3$  may be deposited by PECVD instead of ALD on planar wafers to minimize cost and increase throughput. Duttagupta *et al.* showed that in the PECVD  $\text{AlO}_x/\text{SiN}_y$  stacked layer on a  $p^+$  emitter, 5 nm  $\text{AlO}_x$  was enough for the passivation effect; the additional 65 nm  $\text{SiN}_x$  boosted AR effects and afforded a weighted reflectance of 2.3% in the range 300 to 1000 nm.<sup>299</sup>

When used in BSi solar cells, one additional concern on the dielectric passivation layer regards its surface conformality.  $\text{SiO}_2/\text{SiN}_x$  has thus been adopted by several research groups.<sup>207–209</sup>  $\text{SiO}_2$  is preferred for its great surface conformality (Fig. 34). Liu *et al.* showed that  $\text{SiN}_x$  could not completely cover the BSi surface, resulting in a solar cell efficiency of only 14.9% (Fig. 44a).<sup>207</sup> By inserting an additional thermal oxide layer (20 nm) between bulk silicon and  $\text{SiN}_x$  (60 nm), the surface coverage and associated passivation effect is greatly improved (Fig. 44b); consequently, the solar cell efficiency rises to 15.8%. Similarly, Zhao and co-workers found that their solar cell passivated by the stacked layer of  $\text{SiO}_2/\text{SiN}_x$  offers higher power conversion efficiency (17.1%), in comparison to those passivated either by  $\text{SiO}_2$  (16.1%) or  $\text{SiN}_x$  (16.5%) alone.<sup>208</sup> Interestingly, Zhao *et al.* also noticed that thermal oxidation reduces emitter doping concentration, which is beneficial for minimizing Auger recombination in an over-heavily doped emitter.<sup>208</sup> However, high temperature thermal oxidation is undesirable, especially for  $m\text{-Si}$  solar cells. Hsu *et al.* adopted a trade-off strategy by performing a quick thermal anneal followed by PECVD  $\text{SiN}_x$  growth on an  $n^+$ -emitter. With a hydrogenated  $\text{SiO}_2$  (5 nm)/ $\text{SiN}_x$  (50 nm) stack, the minority carrier lifetime increased substantially from 1.8 to 7.2  $\mu\text{s}$  for a 100 nm-long nano-rod coated solar cell and a high power conversion efficiency of 16.38% was measured.<sup>209</sup> Instead of thermal oxide, Wong *et al.* passivated their nanostructured  $n^+$ -emitter with 20 nm ALD  $\text{Al}_2\text{O}_3$  to achieve good surface conformality, followed by 70 nm PECVD  $\text{SiN}_x$ . A power conversion efficiency of 16.5% was achieved.<sup>211</sup>

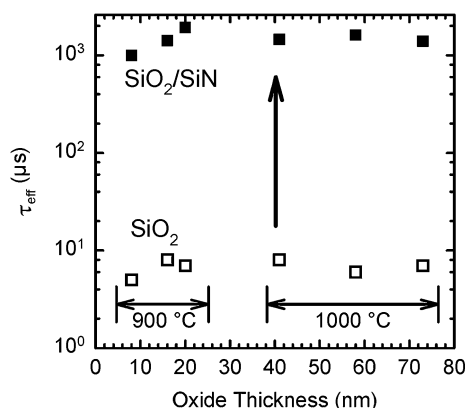


Fig. 49 Comparison of the effective lifetime in a low resistivity  $p\text{-Si}$  wafer with only  $\text{SiO}_2$  passivation (open squares) and with a  $\text{SiO}_2/\text{SiN}_x$  stacked passivation layer. The  $\text{SiO}_2$  thickness varies according to the growth temperature (900 or 1000 °C) and growth time (5–63 min), while the thickness of  $\text{SiN}_x$  is fixed at 60 nm.<sup>263</sup> © IOP Publishing. Reproduced by permission of IOP Publishing. All rights reserved.

## 5 Future research directions

### 5.1 Encapsulation effects

When solar cells are deployed in open-air fields or installed on rooftops, they are encapsulated under a glass layer to prevent moisture attack, mechanical damage and electrical shock. Encapsulation plays a critical role in the energy production and field performance of solar cells. Yet, it is largely ignored in BSi research when the performance of its different textures are evaluated. To our best knowledge, the only work taking encapsulation into consideration was that undertaken by Gjessing and Marstein (Fig. 50).<sup>300</sup>

Gjessing and Marstein compared the weighted reflectance of three different textures on  $c\text{-Si}$  wafers, fabricated *via* isotropic





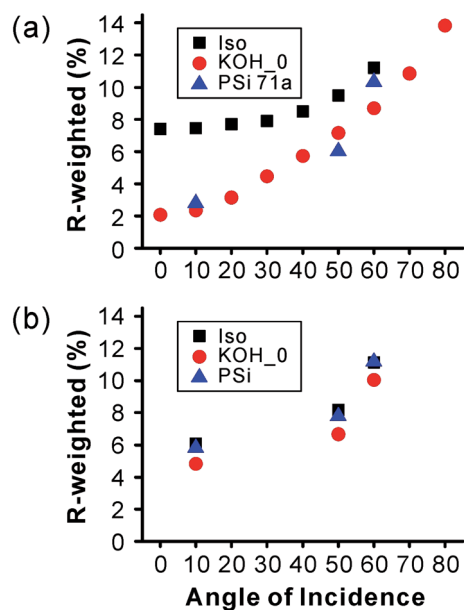


Fig. 50 Weighted reflectance of c-Si with different surface textures via isotropic acid etching, KOH etching (pyramidal structures), and electrochemical HF etching (porous silicon) (a) before and (b) after glass encapsulation.<sup>300</sup> Reproduced by permission of Elsevier.

acid etching, KOH etching (pyramidal structures), and electrochemical HF etching (porous silicon with gradient porosity), and calculated the weighted reflectance using the AM1.5 spectrum from 350 to 1200 nm.<sup>300</sup> Note that the first two textures were further coated with a layer of SiN<sub>x</sub> ARC. Gjessing and Marstein's absolute reflectance readings are likely to be biased, owing to the use of partly polarized illumination and the potential mixing of reflections from both the front and rear sides of the wafers—especially in the long wavelength region. However, they demonstrated one important trend: the reflectance differences among different textures decreased from ~5% to only ~1% upon encapsulation.<sup>300</sup>

Essentially, the main effect of encapsulation is a change of the medium refractive index in the superstrate from  $n = 1$  to  $n = 1.5$ . This effect reduces the AR requirement significantly, while having little impact on the requirement for improved light trapping. Good pyramidal and isotextured surfaces (combined with ARC) reach very low reflectance values and are, arguably, not much worse than BSi in air.

This result indicates that the encapsulation effect must be taken into account, when optimizing the surface roughness of BSi and balancing its optical and electrical gains for practical applications. To be more specific, since the optical gain of BSi relative to other textures is reduced upon encapsulation, a lower aspect ratio nanostructured surface might be required to optimize BSi solar cell efficiency.

## 5.2. Dual-scale structures

It is expected that dual-scale structures, in which nano-scaled structures are coated on micro-scaled textures, will play an increasingly important role in the development of BSi (>100 μm; Fig. 51). Both anti-reflection and light trapping/scattering are

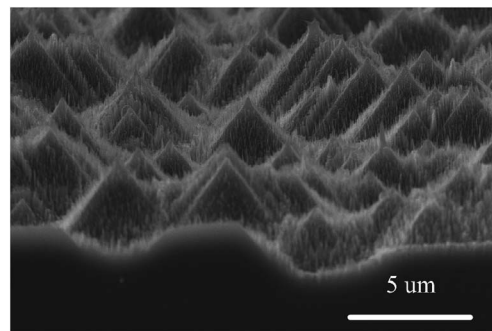


Fig. 51 A micro- and nano-dual scale surface texture on a (100) wafer.<sup>224</sup> Reproduced by permission of the Electrochemical Society.

critical for increasing the optical path length and enhancing photon absorption in solar cells, especially for thin film silicon PV devices. However, sub-100 nm nanostructured BSi is equivalent to an effective index medium; it is optically flat and does not have significant scattering/trapping effects. In other words, this type of BSi offers excellent AR effects, but normal incident light will penetrate through this wafer without much absorption. Nevertheless, the light scattering/trapping effects can be addressed by combining microstructured texture with nanostructured surface. Second, the surface area in BSi must be controlled for a better electrical performance. However, adopting low aspect ratio nanostructures degrades the optical performance of BSi. In contrast, the dual-scale structure is an effective solution to balance the conflicting demands on the reflectance and surface area of BSi. It affords an equivalent optical performance with a reduced thickness or surface area of the nano-structured layer. Third, the microstructured surface improves the mechanical properties of BSi. Xiu *et al.* showed that the dual-scale structure remained non-wettable under abrasion, since nanostructures are protected by the relatively strong micro-structures.<sup>301</sup>

To this end, Toor *et al.* applied dual-scale texturization on a (100) silicon wafer.<sup>35</sup> They first fabricated conventional pyramidal structures on the wafer, followed by producing a thin layer of nanostructured surface using metal-catalyzed chemical etching. Consequently, the weighted reflectance (from 350 to 1000 nm) of 1.8% is realized with a nanostructured layer that is only 100 nm thick, in contrast to ~250 nm on a planar BSi for the same reflectance. This light management strategy minimizes the surface area without compromising the antireflection benefits. The thinner nanostructured layer also improves the blue response of the BSi solar cell, leading to a 17.1% power conversion efficiency. Similar dual-scale surface texture strategies have also been used by several other research groups, where the nanostructured layers are fabricated *via* different techniques, such as metal-assisted chemical etching, electrochemical HF etching, and modified RIE etching.<sup>35,36,41,208,211–213,217,224,302,303</sup>

The dual-scale structure can be potentially fabricated in a single fabrication step. Vorobyev and Guo produced a parallel micro-grooved silicon surface structure by scanning a fs-laser through a wafer.<sup>304</sup> Fine-micro and nanostructures are imposed



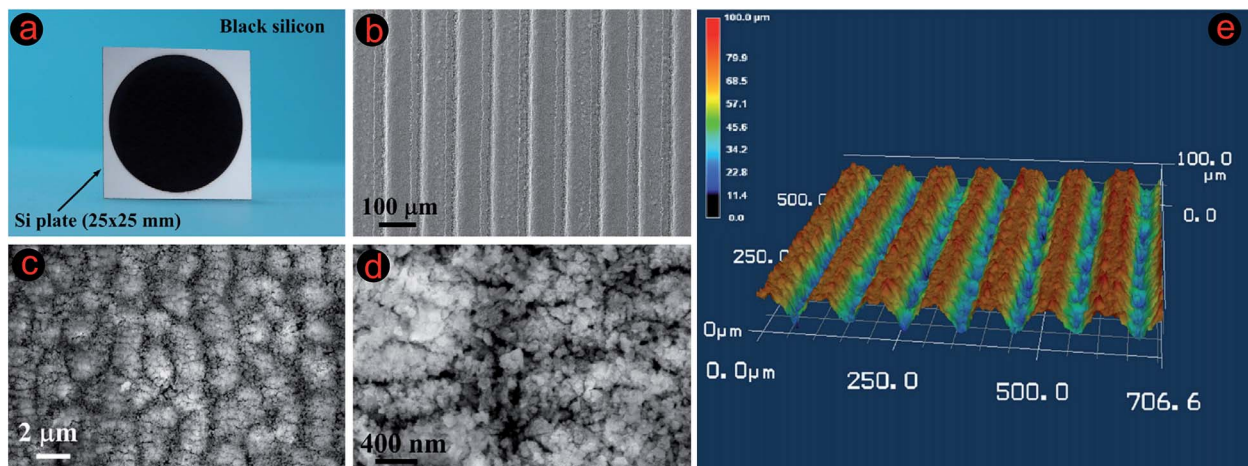


Fig. 52 (a) A photograph of laser treated BSi; (b) SEM image of the micro-grooved BSi; (c) and (d) correspond to the zoomed-in SEM images, showing the micro- and nano-scale surface texture, respectively; (e) A 3D optical image of the micro-grooved BSi.<sup>304</sup> Adapted by permission of Elsevier.

on top of the ridges and valleys of these groove-structures (Fig. 52). This dual-level structure demonstrates a low reflectance across a broadband. In the visible range (250–1000 nm), the reflectance is  $\sim 3\text{--}4\%$ ; in the mid-IR region, the reflectance increases to  $\sim 20\%$  but still amounts to only half of that on an untreated surface. This BSi displays remarkable mechanical strength, unlike other nanostructured surfaces. However, the absorption in the above-bandgap region clearly indicates the presence of laser-induced defects; annealing and/or etching to remove defects is necessary where electrical performance is of great concern.

Interestingly, the “dual-scale design” can also be realized by structuring both the front and back surfaces of a silicon substrate, for anti-reflection and light trapping, respectively. With optimized structures, photocurrent close to the Yablono-vitch limit was predicted for thin film silicon solar cells.<sup>188,305</sup>

### 5.3. Thin solar cells

One possible route to reduce the cost of silicon photovoltaics is to develop thin film solar cells (thickness  $< 30\text{ }\mu\text{m}$ ) or even ultra-thin solar cells (thickness  $< 10\text{ }\mu\text{m}$ ), by significantly decreasing the consumption of silicon during solar cell fabrication. Thin solar cells also offer many other advantages, such as light weight, mechanical flexibility, and easy integration with a diverse range of substrate materials.<sup>186,306–308</sup> Surface texture of ultra-thin silicon *via* alkaline or acid wet etching requires the usage of a photolithography-defined mask<sup>309</sup> and is not considered to be industrially compatible.<sup>233</sup> Hence, the limitation of wet etching in thin film silicon solar cells presents a good opportunity for developing BSi texture.

While BSi poses several challenges, such as in preforming doping, forming good Si/metal contact and increasing surface recombination, novel cell designs can be adopted to mitigate these problems. For example, in a back-contact back-junction (BCBJ) solar cell, the active junction is formed at the rear side and the interdigitated metal contact is built on a flat substrate

surface (Fig. 53a). The BCBJ design has been used in thick silicon solar cells;<sup>310–313</sup> Jeong *et al.* have showed that the benefits of this design are even more significant in thin solar cells, avoiding the doping and contact formation problems associated with BSi. Consequently, a power conversion efficiency of 13.7% was realized in an ultrathin solar cell (thickness  $< 10\text{ }\mu\text{m}$ ); *cf.* 10.9% in a planar solar cell with ARC.<sup>314</sup>

In another slightly different design (Fig. 53b), the p–n junction is also formed at the flat rear side, while the front metal contact is still built on BSi. However, a front surface field (FSF) has been created *via* heavy boron doping, in order to reduce

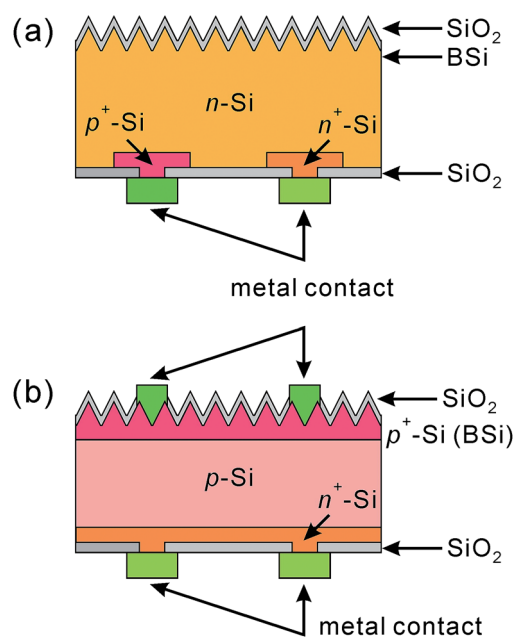


Fig. 53 (a) A schematic of a back-contact back-junction solar cell with a BSi front surface.<sup>314</sup> (b) A schematic of a back-junction solar cell with a BSi front surface and front surface field.<sup>187</sup>



surface recombination. A similar design has been adopted by Chan and co-workers in fabricating  $\sim 5.7$   $\mu\text{m}$  thick micro-BSi solar cells.<sup>187</sup> It should be pointed that a FSF may also be incorporated into a BCBJ cell. In addition to its role of reducing surface recombination, a FSF also improves lateral base conductivity and enhances cell stability against UV radiation in BCBJ solar cells.<sup>315–317</sup>

For thin solar cells, light trapping becomes critical for photon management, in addition to anti-reflection.<sup>318–322</sup> BSi with a feature size less than 100 nm is optically flat and does not scatter light nor increase the optical path length. Hence, additional light trapping structures become essential to enhance the efficiencies of this type of thin solar cell. By incorporating a diffuse backside reflector into a BSi microcell, Chan *et al.* have showed that the solar cell efficiency improved from 6.9% to 11.4%.<sup>187</sup> Alternatively, one may also consider optimizing the feature size of BSi; optimal modeling has showed that a sub-microstructured surface (with period  $> \sim 500$  nm) could retain good light trapping effects, while simultaneously maintaining low surface reflection.<sup>234</sup>

## 6 Concluding remarks

Various methods have been developed to fabricate micro- or nano-structured BSi surfaces. By carefully varying their process parameters, a wide range of surface morphologies can be created with a high degree of control. For example, the porosity and thickness can be manipulated by simply adjusting current density and etching time during electrochemical etching in HF. Moreover, the wet etching, such as metal-assisted chemical etching, holds a great promise for large scale industrial deployment, owing to its simple experimental setup and fast etching rate. We should also highlight RIE, which can produce silicon nano-needles and result in smooth refractive index transitions from air to bulk silicon. Consequently, very low reflectance, down to less than 1% over a broadband and different polarization, has been realized with BSi.

While BSi offers superior optical performance, its poor electrical characteristics hinder the overall power conversion efficiencies of BSi solar cells. The roughed surface in BSi leads to increased surface recombination, causes high and sometimes non-uniform doping concentrations, and poses significant challenges for forming a good silicon/metal contact. Consequently, improved fabrication processes are required to balance the optical gains and electrical losses of BSi in order to achieve high solar cell efficiencies. A few strategies have thus been identified, including controlling the thickness of the nanostructured layer and using low aspect ratio nanostructures, developing new doping methods and minimizing Auger recombination, applying a thorough surface defect cleaning process and providing excellent surface passivation. The incorporation of BSi in advanced solar cell designs and in thin silicon wafer production has also been surveyed; these techniques may potentially improve solar cell efficiencies or reduce material cost during photovoltaic production. It is worth adding that BSi texturing methods are likely to also play an important role in mc-Si and ultra-thin solar cells—especially where

conventional wet etching methods fail as cell thicknesses decrease.

Owing to the importance of surface passivation to BSi, major passivation techniques using  $\text{SiN}_x$ , thermal oxide,  $\text{Al}_2\text{O}_3$  and a-Si have been critically examined. It is found that atomic layer deposited  $\text{Al}_2\text{O}_3$  offers excellent surface conformality and passivation to the silicon surface, especially on  $\text{p}^+$ -emitters. With ALD  $\text{Al}_2\text{O}_3$  passivation, a record high 18.7% efficient BSi solar cell has been successfully fabricated. As the market share of n-type solar cells (with  $\text{p}^+$ -emitters) is expected to rise in the near future, this passivation technique is particularly attractive and may become a new industry standard.

While the efficiencies of BSi solar cells currently remain below those of conventional silicon solar cells, this review offers some promising solutions. In particular, with a better understanding of the carrier loss mechanisms and improvements in cell design and fabrication strategies, the efficiency of BSi solar cells will continue to increase. The future of BSi remains bright.

## Acknowledgements

The Solar Energy Research Institute of Singapore is sponsored by the National University of Singapore (NUS) and the National Research Foundation of Singapore through the Singapore Economic Development Board (SEDB). X.L. is grateful to SEDB for a Clean Energy Scholarship. J.M.C. thanks the Fulbright Commission for a UK-US Fulbright Scholar Award, hosted by Argonne National Laboratory where work done was supported by DOE Office of Science, Office of Basic Energy Sciences, under contract no. DE-AC02-06CH11357. P.R.C. is indebted to I. Wender (Terrativa Minerais S.A.) for sponsoring this research.

## References

- 1 H. Föll, M. Christophersen, J. Carstensen and G. Hasse, *Mater. Sci. Eng., R*, 2002, **39**, 93–141.
- 2 M. J. Sailor, *Porous Silicon in Practice: Preparation, Characterization and Applications*, Wiley, Weinheim, Germany, 2012.
- 3 K. W. Kolasinski, *Curr. Opin. Solid State Mater. Sci.*, 2005, **9**, 73–83.
- 4 G. Barillaro, A. Nannini and M. Piotta, *Sens. Actuators, A*, 2002, **102**, 195–201.
- 5 A. Jane, R. Dronov, A. Hodges and N. H. Voelcker, *Trends Biotechnol.*, 2009, **27**, 230–239.
- 6 M. P. Stewart and J. Buriak, *Adv. Mater.*, 2000, **12**, 859–869.
- 7 L. De Stefano, L. Moretti, A. Lamberti, O. Longo, M. Rocchia, A. M. Rossi, P. Arcari and I. Rendina, *IEEE Trans. Nanotechnol.*, 2004, **3**, 49–54.
- 8 A. Angelescu, I. Kleps, M. Mihaela, M. Simion, T. Neghina, S. Petrescu, N. Moldovan, C. Paduraru and A. Raducanu, *Rev. Adv. Mater. Sci.*, 2003, **5**, 440–449.
- 9 M. J. Sailor and E. J. Lee, *Adv. Mater.*, 1997, **9**, 783–793.
- 10 M. Berger, C. Dieker, M. Thonissen, L. Vescan, H. Luth, H. Munder, W. Theiss, M. Wernke and P. Grosse, *J. Phys. D: Appl. Phys.*, 1994, **27**, 1333–1336.





- 11 C. Mazzoleni and L. Pavesi, *Appl. Phys. Lett.*, 1995, **67**, 2983–2985.
- 12 M. Berger, M. Thönissen, R. Arens-Fischer, H. Münder, H. Lüth, M. Arntzen and W. Theiß, *Thin Solid Films*, 1995, **255**, 313–316.
- 13 M. Araki, H. Koyama and N. Koshida, *Appl. Phys. Lett.*, 1996, **69**, 2956–2958.
- 14 L. Pavesi, C. Mazzoleni, A. Tredicucci and V. Pellegrini, *Appl. Phys. Lett.*, 1995, **67**, 3280–3282.
- 15 M. Berger, R. Arens-Fischer, M. Thönissen, M. Krüger, S. Billat, H. Lüth, S. Hilbrich, W. Theiss and P. Grosse, *Thin Solid Films*, 1997, **297**, 237–240.
- 16 V. Torres-Costa and R. J. Martin-Palma, *J. Mater. Sci.*, 2010, **45**, 2823–2838.
- 17 M. Steglich, M. Zilk, F. Schrempel, A. Tünnermann and E. B. Kley, *Appl. Phys. Lett.*, 2013, **102**, 111110.
- 18 M. Steglich, M. Zilk, A. Bingel, C. Patzig, T. Käsebie, F. Schrempel, E.-B. Kley and A. Tünnermann, *J. Appl. Phys.*, 2013, **114**, 183102.
- 19 J.-H. Park, L. Gu, G. von Maltzahn, E. Ruoslahti, S. N. Bhatia and M. J. Sailor, *Nat. Mater.*, 2009, **8**, 331–336.
- 20 J. Rong, C. Masarapu, J. Ni, Z. Zhang and B. Wei, *ACS Nano*, 2010, **4**, 4683–4690.
- 21 M. Ge, X. Fang, J. Rong and C. Zhou, *Nanotechnology*, 2013, **24**, 422001.
- 22 A. Vu, Y. Qian and A. Stein, *Adv. Energy Mater.*, 2012, **2**, 1056–1085.
- 23 J. Oh, T. G. Deutsch, H.-C. Yuan and H. M. Branz, *Energy Environ. Sci.*, 2011, **4**, 1690–1694.
- 24 E. P. Ivanova, J. Hasan, H. K. Webb, G. Gervinskas, S. Juodkazis, V. K. Truong, A. H. Wu, R. N. Lamb, V. A. Baulin and G. S. Watson, *Nat. Commun.*, 2013, **4**, 2838.
- 25 D. Qi, N. Lu, H. Xu, B. Yang, C. Huang, M. Xu, L. Gao, Z. Wang and L. Chi, *Langmuir*, 2009, **25**, 7769–7772.
- 26 M. Barberoglou, V. Zorba, A. Pagozidis, C. Fotakis and E. Stratakis, *Langmuir*, 2010, **26**, 13007–13014.
- 27 P. Granitzer and K. Rumpf, *Materials*, 2010, **3**, 943–998.
- 28 A. B. Christiansen, J. S. Clausen, N. A. Mortensen and A. Kristensen, *Microelectron. Eng.*, 2014, **121**, 47–50.
- 29 J. Wei, J. M. Buriak and G. Siuzdak, *Nature*, 1999, **399**, 243–246.
- 30 S. Fan, M. G. Chapline, N. R. Franklin, T. W. Tomblor, A. M. Cassell and H. Dai, *Science*, 1999, **283**, 512–514.
- 31 A. Žukauskas, M. Malinauskas, A. Kadys, G. Gervinskas, G. Seniutinas, S. Kandasamy and S. Juodkazis, *Opt. Express*, 2013, **21**, 6901–6909.
- 32 J. Oh, H. C. Yuan and H. M. Branz, *Nat. Nanotechnol.*, 2012, **7**, 743–748.
- 33 Y. Wang, Y. P. Liu, T. Lai, H. L. Liang, Z. L. Li, Z. X. Mei, F. M. Zhang, A. Kuznetsov and X. L. Du, *RSC Adv.*, 2013, **3**, 15483–15489.
- 34 H. C. Yuan, V. E. Yost, M. R. Page, P. Stradins, D. L. Meier and H. M. Branz, *Appl. Phys. Lett.*, 2009, **95**, 123501.
- 35 F. Toor, H. M. Branz, M. R. Page, K. M. Jones and H. C. Yuan, *Appl. Phys. Lett.*, 2011, **99**, 103501.
- 36 X. Ao, X. Tong, D. S. Kim, L. Zhang, M. Knez, F. Müller, S. He and V. Schmidt, *Appl. Phys. Lett.*, 2012, **101**, 111901.
- 37 G. Masson, M. Latour, M. Reking, I. Theologitis and M. Papoutsis, *Global Market Outlook for Photovoltaics 2013–2017*, European Photovoltaic Industry Association, 2013.
- 38 P. Menna, G. Di Francia and V. La Ferrara, *Sol. Energy Mater. Sol. Cells*, 1995, **37**, 13–24.
- 39 L. Stalmans, J. Poortmans, H. Bender, M. Caymax, K. Said, E. Vazsonyi, J. Nijs and R. Mertens, *Prog. Photovolt. Res. Appl.*, 1998, **6**, 233–246.
- 40 V. Y. Yerokhov and I. I. Melnyk, *Renewable Sustainable Energy Rev.*, 1999, **3**, 291–322.
- 41 R. Bilyalov, R. Lüdemann, W. Wettling, L. Stalmans, J. Poortmans, J. Nijs, L. Schirone, G. Sotgiu, S. Strehlke and C. Lévy-Clément, *Sol. Energy Mater. Sol. Cells*, 2000, **60**, 391–420.
- 42 M. D. Kelzenberg, S. W. Boettcher, J. A. Petykiewicz, D. B. Turner-Evans, M. C. Putnam, E. L. Warren, J. M. Spurgeon, R. M. Briggs, N. S. Lewis and H. A. Atwater, *Nat. Mater.*, 2010, **9**, 239–244.
- 43 C. L. Cheng, C. W. Liu, J. T. Jeng, B. T. Dai and Y. H. Lee, *J. Electrochem. Soc.*, 2009, **156**, H356–H360.
- 44 L. Tsakalacos, J. Balch, J. Fronheiser, B. Korevaar, O. Sulima and J. Rand, *Appl. Phys. Lett.*, 2007, **91**, 233117.
- 45 Y. Li, H. Yu, J. Li, S. M. Wong, X. W. Sun, X. Li, C. Cheng, H. J. Fan, J. Wang and N. Singh, *Small*, 2011, **7**, 3138–3143.
- 46 S. Chattopadhyay, Y. F. Huang, Y. J. Jen, A. Ganguly, K. H. Chen and L. C. Chen, *Mater. Sci. Eng., R*, 2010, **69**, 1–35.
- 47 R. Memming and G. Schwandt, *Surf. Sci.*, 1966, **4**, 109–124.
- 48 A. Cullis and L. Canham, *Nature*, 1991, **353**, 335–338.
- 49 A. Cullis, L. T. Canham and P. Calcott, *J. Appl. Phys.*, 1997, **82**, 909–965.
- 50 K. Hirschman, L. Tsybeskov, S. Dutttagupta and P. Fauchet, *Nature*, 1996, **384**, 338–341.
- 51 L. T. Canham, *Appl. Phys. Lett.*, 1990, **57**, 1046–1048.
- 52 L. H. Lie, M. Duerdin, E. M. Tuite, A. Houlton and B. R. Horrocks, *J. Electroanal. Chem.*, 2002, **538**, 183–190.
- 53 Y. Chao, L. Šiller, S. Krishnamurthy, P. R. Coxon, U. Bangert, M. Gass, L. Kjeldgaard, S. N. Patole, L. H. Lie and N. O'Farrell, *Nat. Nanotechnol.*, 2007, **2**, 486–489.
- 54 J. H. Ahire, Q. Wang, P. R. Coxon, G. Malhotra, R. Brydson, R. Chen and Y. Chao, *ACS Appl. Mater. Interfaces*, 2012, **4**, 3285–3292.
- 55 P. Kleimann, J. Linnros and R. Juhasz, *Appl. Phys. Lett.*, 2001, **79**, 1727–1729.
- 56 H. S. Jang, H.-J. Choi, B.-Y. Oh and J. H. Kim, *Electrochem. Solid-State Lett.*, 2011, **14**, D5–D9.
- 57 X. Zhang, S. Collins and R. Smith, *J. Electrochem. Soc.*, 1989, **136**, 1561–1565.
- 58 X. Zhang, *J. Electrochem. Soc.*, 2004, **151**, C69–C80.
- 59 P. Kleimann, X. Badel and J. Linnros, *Appl. Phys. Lett.*, 2005, **86**, 183108.
- 60 V. Lehmann, *Electrochemistry of Silicon: Instrumentation, Science, Materials and Applications*, Wiley-VCH, Weinheim, 2002.
- 61 S. Matthias, F. Müller, C. Jamois, R. B. Wehrspohn and U. Gösele, *Adv. Mater.*, 2004, **16**, 2166–2170.



- 62 C. Striemer and P. Fauchet, *Appl. Phys. Lett.*, 2002, **81**, 2980–2982.
- 63 R. Bilyalov, L. Stalmans and J. Poortmans, *J. Electrochem. Soc.*, 2003, **150**, G216–G222.
- 64 L. L. Ma, Y. C. Zhou, N. Jiang, X. Lu, J. Shao, W. Lu, J. Ge, X. M. Ding and X. Y. Hou, *Appl. Phys. Lett.*, 2006, **88**, 171907.
- 65 D. Ariza-Flores, J. Pérez-Huerta, Y. Kumar, A. Encinas and V. Agarwal, *Sol. Energy Mater. Sol. Cells*, 2014, **123**, 144–149.
- 66 E. Osorio, R. Urteaga, L. N. Acquaroli, G. García-Salgado, H. Juárez and R. R. Koropecski, *Sol. Energy Mater. Sol. Cells*, 2011, **95**, 3069–3073.
- 67 H. A. Macleod, *Thin-Film Optical Filters*, CRC Press, Boca Raton, FL, 4th edn, 2010.
- 68 J. H. Selj, T. T. Mongstad, R. Søndena and E. S. Marstein, *Sol. Energy Mater. Sol. Cells*, 2011, **95**, 2576–2582.
- 69 V. Y. Yerokhov, R. Hezel, M. Lipinski, R. Ciach, H. Nagel, A. Mylynych and P. Panek, *Sol. Energy Mater. Sol. Cells*, 2002, **72**, 291–298.
- 70 SEMSYSCO, <http://www.semsysco.com/porous-silicon/>, accessed June 30 2014.
- 71 R. Smith and S. Collins, *J. Appl. Phys.*, 1992, **71**, R1–R22.
- 72 S. Shih, K. Jung, T. Hsieh, J. Sarathy, J. Campbell and D. Kwong, *Appl. Phys. Lett.*, 1992, **60**, 1863–1865.
- 73 H. Robbins and B. Schwartz, *J. Electrochem. Soc.*, 1959, **106**, 505–508.
- 74 H. Robbins and B. Schwartz, *J. Electrochem. Soc.*, 1960, **107**, 108–111.
- 75 B. Schwartz and H. Robbins, *J. Electrochem. Soc.*, 1961, **108**, 365–372.
- 76 B. Schwartz and H. Robbins, *J. Electrochem. Soc.*, 1976, **123**, 1903–1909.
- 77 É. Vázsonyi, E. Szilágyi, P. Petrik, Z. Horváth, T. Lohner, M. Fried and G. Jalsovszky, *Thin Solid Films*, 2001, **388**, 295–302.
- 78 G. Kumaravelu, M. M. Alkaisi, A. Bittar, D. Macdonald and J. Zhao, *Curr. Appl. Phys.*, 2004, **4**, 108–110.
- 79 R. Khandelwal, U. Plachetka, B. Min, C. Moormann and H. Kurz, *Microelectron. Eng.*, 2013, **111**, 220–223.
- 80 Y.-T. Cheng, J.-J. Ho, S.-Y. Tsai, Z.-Z. Ye, W. Lee, D.-S. Hwang, S.-H. Chang, C.-C. Chang and K. L. Wang, *Sol. Energy*, 2011, **85**, 87–94.
- 81 D. Turner, *J. Electrochem. Soc.*, 1960, **107**, 810–816.
- 82 M. Winton, S. Russell and R. Gronsky, *J. Appl. Phys.*, 1997, **82**, 436–441.
- 83 M. Saadoun, N. Mliki, H. Kaabi, K. Daoudi, B. Bessaïs, H. Ezzaouia and R. Bennaceur, *Thin Solid Films*, 2002, **405**, 29–34.
- 84 M. B. Rabha, W. Dimassi, M. Bouaïcha, H. Ezzaouia and B. Bessaïs, *Sol. Energy*, 2009, **83**, 721–725.
- 85 M. Ben Rabha, M. Saadoun, M. Boujmil, B. Bessaïs, H. Ezzaouia and R. Bennaceur, *Appl. Surf. Sci.*, 2005, **252**, 488–493.
- 86 A. Ben Jaballah, M. Hassen, M. Hajji, M. Saadoun, B. Bessaïs and H. Ezzaouia, *Phys. Status Solidi A*, 2005, **202**, 1606–1610.
- 87 A. B. Jaballah, M. Saadoun, M. Hajji, H. Ezzaouia and B. Bessaïs, *Appl. Surf. Sci.*, 2004, **238**, 199–203.
- 88 M. Saadoun, B. Bessaïs, N. Mliki, M. Ferid, H. Ezzaouia and R. Bennaceur, *Appl. Surf. Sci.*, 2003, **210**, 240–248.
- 89 M. B. Rabha, H. Anouar and B. Brahim, *Sol. Energy*, 2012, **86**, 1411–1415.
- 90 R. T. Collins, P. M. Fauchet and M. A. Tischler, *Phys. Today*, 1997, **50**, 24–31.
- 91 X. Li and P. Bohn, *Appl. Phys. Lett.*, 2000, **77**, 2572–2574.
- 92 Z. Huang, N. Geyer, P. Werner, J. De Boer and U. Gösele, *Adv. Mater.*, 2011, **23**, 285–308.
- 93 K. Nishioka, S. Horita, K. Ohdaira and H. Matsumura, *Sol. Energy Mater. Sol. Cells*, 2008, **92**, 919–922.
- 94 S. Yae, Y. Kawamoto, H. Tanaka, N. Fukumuro and H. Matsuda, *Electrochem. Commun.*, 2003, **5**, 632–636.
- 95 S. K. Srivastava, D. Kumar, P. K. Singh, M. Kar, V. Kumar and M. Husain, *Sol. Energy Mater. Sol. Cells*, 2010, **94**, 1506–1511.
- 96 S. Koynov, M. S. Brandt and M. Stutzmann, *Appl. Phys. Lett.*, 2006, **88**, 203107.
- 97 Y. T. Lu and A. R. Barron, *Phys. Chem. Chem. Phys.*, 2013, **15**, 9862–9870.
- 98 C. Y. Chen, W. J. Li and H. H. Chen, *ChemPhysChem*, 2012, **13**, 1415–1420.
- 99 Y. Li, J. Zhang, S. Zhu, H. Dong, Z. Wang, Z. Sun, J. Guo and B. Yang, *J. Mater. Chem.*, 2009, **19**, 1806–1810.
- 100 W. Choi, T. Liew, M. Dawood, H. I. Smith, C. Thompson and M. Hong, *Nano Lett.*, 2008, **8**, 3799–3802.
- 101 S. W. Chang, V. P. Chuang, S. T. Boles, C. A. Ross and C. V. Thompson, *Adv. Funct. Mater.*, 2009, **19**, 2495–2500.
- 102 C. F. Guo, T. Sun, Y. Wang, J. Gao, Q. Liu, K. Kempa and Z. Ren, *Small*, 2013, **9**, 2415–2419.
- 103 Y. Matsui and S. Adachi, *J. Appl. Phys.*, 2013, **113**, 173502.
- 104 S. Koynov, M. S. Brandt and M. Stutzmann, *J. Appl. Phys.*, 2011, **110**, 043537.
- 105 S. K. Srivastava, D. Kumar, M. Sharma, R. Kumar and P. K. Singh, *Sol. Energy Mater. Sol. Cells*, 2012, **100**, 33–38.
- 106 H. Jansen, M. de Boer, R. Legtenberg and M. Elwenspoek, *J. Micromech. Microeng.*, 1995, **5**, 115–120.
- 107 R. Dussart, T. Tillocher, P. Lefauchaux and M. Boufnichel, *J. Phys. D: Appl. Phys.*, 2014, **47**, 123001.
- 108 R. Dussart, M. Boufnichel, G. Marcos, P. Lefauchaux, A. Basillais, R. Benoit, T. Tillocher, X. Mellhaoui, H. Estrade-Szwarckopf and P. Ranson, *J. Micromech. Microeng.*, 2004, **14**, 190.
- 109 R. Dussart, X. Mellhaoui, T. Tillocher, P. Lefauchaux, M. Boufnichel and P. Ranson, *Microelectron. Eng.*, 2007, **84**, 1128–1131.
- 110 R. Dussart, X. Mellhaoui, T. Tillocher, P. Lefauchaux, M. Volatier, C. Socquet-Clerc, P. Brault and P. Ranson, *J. Phys. D: Appl. Phys.*, 2005, **38**, 3395.
- 111 M. J. De Boer, J. G. E. Gardeniers, H. V. Jansen, E. Smulders, M. J. Gilde, G. Roelofs, J. N. Sasserath and M. Elwenspoek, *J. Microelectromech. Syst.*, 2002, **11**, 385–401.
- 112 H. V. Jansen, M. J. De Boer, S. Unnikrishnan, M. C. Louwerse and M. C. Elwenspoek, *J. Micromech. Microeng.*, 2009, **19**, 033001.



- 113 X. Mellhaoui, R. Dussart, T. Tillocher, P. Lefauchaux, P. Ranson, M. Boufnichel and L. J. Overzet, *J. Appl. Phys.*, 2005, **98**, 104901.
- 114 M. Kroll, M. Otto, T. Kšebier, K. Füchsel, R. Wehrspohn, E. B. Kley, A. Tunnermann and T. Pertsch, *Proceedings of Photonics for Solar Energy Systems IV*, Brussels, 2012, p. 843817.
- 115 J. Yoo, G. Yu and J. Yi, *Mater. Sci. Eng., B*, 2009, **159–160**, 333–337.
- 116 J. S. Yoo, I. O. Parm, U. Gangopadhyay, K. Kim, S. K. Dhungel, D. Mangalaraj and J. Yi, *Sol. Energy Mater. Sol. Cells*, 2006, **90**, 3085–3093.
- 117 S. M. Rossnagel, J. J. Cuomo and W. D. Westwood, *Handbook of Plasma Processing Technology: Fundamentals, Etching, Deposition, and Surface Interactions*, William Andrew Inc., Norwich, New York, 1990.
- 118 Y. Xia, B. Liu, S. Zhong and C. Li, *J. Electron Spectrosc. Relat. Phenom.*, 2012, **184**, 589–592.
- 119 Y. Xia, B. Liu, J. Liu, Z. Shen and C. Li, *Sol. Energy*, 2011, **85**, 1574–1578.
- 120 N. Cheung, *Mater. Chem. Phys.*, 1996, **46**, 132–139.
- 121 D. Murias, C. Reyes-Betanzo, M. Moreno, A. Torres, A. Itzmoyotl, R. Ambrosio, M. Soriano, J. Lucas and P. R. I. Cabarrocas, *Mater. Sci. Eng., B*, 2012, **177**, 1509–1513.
- 122 J. Gittleman, E. Sichel, H. Lehmann and R. Widmer, *Appl. Phys. Lett.*, 1979, **35**, 742–744.
- 123 Y. Inomata, K. Fukui and K. Shirasawa, *Sol. Energy Mater. Sol. Cells*, 1997, **48**, 237–242.
- 124 J. Yoo, *Sol. Energy*, 2010, **84**, 730–734.
- 125 S. Kalem, P. Werner, Ö. Arthursson, V. Talalaev, B. Nilsson, M. Hagberg, H. Frederiksen and U. Södervall, *Nanotechnology*, 2011, **22**, 235307.
- 126 K.-S. Lee, M.-H. Ha, J. H. Kim and J.-W. Jeong, *Sol. Energy Mater. Sol. Cells*, 2011, **95**, 66–68.
- 127 C.-H. Hsu, H.-C. Lo, C.-F. Chen, C. T. Wu, J.-S. Hwang, D. Das, J. Tsai, L.-C. Chen and K.-H. Chen, *Nano Lett.*, 2004, **4**, 471–475.
- 128 C. Hsu, Y. Huang, L. Chen, S. Chattopadhyay, K. Chen, H. Lo and C. Chen, *J. Vac. Sci. Technol., B*, 2006, **24**, 308–311.
- 129 Y.-F. Huang, S. Chattopadhyay, Y.-J. Jen, C.-Y. Peng, T.-A. Liu, Y.-K. Hsu, C.-L. Pan, H.-C. Lo, C.-H. Hsu and Y.-H. Chang, *Nat. Nanotechnol.*, 2007, **2**, 770–774.
- 130 Y. Chen, Z. Xu, M. R. Gartia, D. Whitlock, Y. Lian and G. L. Liu, *ACS Nano*, 2011, **5**, 8002–8012.
- 131 F. Laermer and A. Schlip, *US Pat.*, US5501893, 1996.
- 132 F. Laermer and A. Schlip, *US Pat.*, US6284148, 2001.
- 133 G. Kumaravelu, M. M. Alkaisi and A. Bittar, *Proceedings of the 29th IEEE Photovoltaic Specialists Conference*, New Orleans, 2002, pp. 258–261.
- 134 W. Nositschka, C. Beneking, O. Voigt and H. Kurz, *Sol. Energy Mater. Sol. Cells*, 2003, **76**, 155–166.
- 135 K. N. Nguyen, P. Basset, F. Marty, Y. Leprince-Wang and T. Bourouina, *J. Appl. Phys.*, 2013, **113**, 194903.
- 136 S. Schaefer and R. Ludemann, *J. Vac. Sci. Technol., A*, 1999, **17**, 749–754.
- 137 S. H. Zaidi, D. S. Ruby and J. M. Gee, *IEEE Trans. Electron Devices*, 2001, **48**, 1200–1206.
- 138 A. Y. Vorobyev and C. Guo, *Laser Photonics Rev.*, 2013, **7**, 385–407.
- 139 T.-H. Her, R. J. Finlay, C. Wu, S. Deliwala and E. Mazur, *Appl. Phys. Lett.*, 1998, **73**, 1673–1675.
- 140 T.-H. Her, R. J. Finlay, C. Wu and E. Mazur, *Appl. Phys. A: Mater. Sci. Process.*, 2000, **70**, 383–385.
- 141 C. Wu, C. Crouch, L. Zhao, J. Carey, R. Younkin, J. Levinson, E. Mazur, R. Farrell, P. Gothoskar and A. Karger, *Appl. Phys. Lett.*, 2001, **78**, 1850–1852.
- 142 C. H. Crouch, J. E. Carey, J. M. Warrender, M. J. Aziz, E. Mazur and F. Y. Génin, *Appl. Phys. Lett.*, 2004, **84**, 1850–1852.
- 143 T. Sarnet, T. Derrien, R. Torres, P. Delaporte, F. Torregrosa, M. Sher, Y. Lin, B. Franta, G. Deng and E. Mazur, *Proceedings of 28th European Photovoltaic Solar Energy Conference and Exhibition*, Paris, 2013, pp. 1882–1886.
- 144 T. Sarnet, J. E. Carey and E. Mazur, *Proceedings of International Symposium on High Power Laser Ablation 2012*, New Mexico, 2012, pp. 219–228.
- 145 S. Sundaram and E. Mazur, *Nat. Mater.*, 2002, **1**, 217–224.
- 146 J. E. Carey, C. H. Crouch, M. Shen and E. Mazur, *Opt. Lett.*, 2005, **30**, 1773–1775.
- 147 M. A. Sheehy, B. R. Tull, C. M. Friend and E. Mazur, *Mater. Sci. Eng., B*, 2007, **137**, 289–294.
- 148 I. Umez, J. M. Warrender, S. Charnvanichborikarn, A. Kohno, J. S. Williams, M. Tabbal, D. G. Papazoglou, X.-C. Zhang and M. J. Aziz, *J. Appl. Phys.*, 2013, **113**, 213501.
- 149 K. Liu, S. Qu, X. Zhang, F. Tan, Y. Bi, S. Lu and Z. Wang, *Appl. Phys. A: Mater. Sci. Process.*, 2014, **114**, 765–768.
- 150 Q. Lü, J. Wang, C. Liang, L. Zhao and Z. Jiang, *Opt. Lett.*, 2013, **38**, 1274–1276.
- 151 M. Halbwax, T. Sarnet, P. Delaporte, M. Sentis, H. Etienne, F. Torregrosa, V. Vervisch, I. Perichaud and S. Martinuzzi, *Thin Solid Films*, 2008, **516**, 6791–6795.
- 152 T. Sarnet, M. Halbwax, R. Torres, P. Delaporte, M. Sentis, S. Martinuzzi, V. Vervisch, F. Torregrosa, H. Etienne and L. Roux, *Proceedings of Commercial and Biomedical Applications of Ultrafast Lasers VIII*, San Jose, 2008, p. 688119.
- 153 Y. Peng, Y. Wen, D. Zhang, S. Da Luo, L. Chen and Y. M. Zhu, *Appl. Opt.*, 2011, **50**, 4765–4768.
- 154 M. Huang, F. Zhao, Y. Cheng, N. Xu and Z. Xu, *Opt. Express*, 2010, **18**, A600–A619.
- 155 M. Shen, C. H. Crouch, J. E. Carey and E. Mazur, *Appl. Phys. Lett.*, 2004, **85**, 5694–5696.
- 156 R. Le Harzic, H. Schuck, D. Sauer, T. Anhut, I. Riemann and K. König, *Opt. Express*, 2005, **13**, 6651–6656.
- 157 M. Shen, C. Crouch, J. Carey, R. Younkin, E. Mazur, M. Sheehy and C. Friend, *Appl. Phys. Lett.*, 2003, **82**, 1715–1717.
- 158 M. Pralle, J. Carey, H. Homayoon, S. Alie, J. Sickler, X. Li, J. Jiang, D. Miller, C. Palsule and J. McKee, *Proceedings of Infrared Technology and Applications XXXVI*, Orlando, 2010, p. 76600N.





- 159 J. Sullivan, C. Simmons, J. Krich, A. Akey, D. Recht, M. Aziz and T. Buonassisi, *J. Appl. Phys.*, 2013, **114**, 103701.
- 160 J. E. Carey and J. Sickler, *Laser Focus World*, 2009, **45**, 39–44.
- 161 G. Nava, R. Osellame, R. Ramponi and K. C. Vishnubhatla, *Opt. Mater. Express*, 2013, **3**, 612–623.
- 162 G. Z. Chen, D. J. Fray and T. W. Farthing, *Nature*, 2000, **407**, 361–364.
- 163 T. Nohira, K. Yasuda and Y. Ito, *Nat. Mater.*, 2003, **2**, 397–401.
- 164 P. C. Pistorius and D. J. Fray, *J. South. Afr. Inst. Min. Metall.*, 2006, **106**, 31–41.
- 165 L. Burton and A. Madjid, *Phys. Rev.*, 1969, **185**, 1127.
- 166 C. Spinella, S. Lombardo and F. Priolo, *J. Appl. Phys.*, 1998, **84**, 5383–5414.
- 167 G. Olson and J. Roth, *Mater. Sci. Rep.*, 1988, **3**, 1–77.
- 168 S. K. Cho, F.-R. F. Fan and A. J. Bard, *Electrochim. Acta*, 2012, **65**, 57–63.
- 169 K. Yasuda, T. Nohira, K. Amezawa, Y. H. Ogata and Y. Ito, *J. Electrochem. Soc.*, 2005, **152**, D69–D74.
- 170 K. Yasuda, T. Nohira and Y. Ito, *J. Phys. Chem. Solids*, 2005, **66**, 443–447.
- 171 K. Yasuda, T. Nohira, R. Hagiwara and Y. H. Ogata, *Electrochim. Acta*, 2007, **53**, 106–110.
- 172 X. Jin, P. Gao, D. Wang, X. Hu and G. Z. Chen, *Angew. Chem., Int. Ed.*, 2004, **43**, 733–736.
- 173 E. Juzeliunas, A. Cox and D. J. Fray, *Electrochem. Commun.*, 2010, **12**, 1270–1274.
- 174 E. Juzeliunas, A. Cox and D. J. Fray, *Electrochim. Acta*, 2012, **68**, 123–127.
- 175 S. K. Cho, F. R. F. Fan and A. J. Bard, *Angew. Chem., Int. Ed.*, 2012, **124**, 12912–12916.
- 176 J. Zhao, J. Li, P. Ying, W. Zhang, L. Meng and C. Li, *Chem. Commun.*, 2013, **49**, 4477–4479.
- 177 J. Zhao, A. Wang, M. A. Green and F. Ferrazza, *Appl. Phys. Lett.*, 1998, **73**, 1991.
- 178 F. Priolo, T. Gregorkiewicz, M. Galli and T. F. Krauss, *Nat. Nanotechnol.*, 2014, **9**, 19–32.
- 179 H.-P. Wang, D.-H. Lien, M.-L. Tsai, C.-A. Lin, H.-C. Chang, K.-Y. Lai and J.-H. He, *J. Mater. Chem. C*, 2014, **2**, 3144–3171.
- 180 J. Zhu, Z. Yu, S. Fan and Y. Cui, *Mater. Sci. Eng., R*, 2010, **70**, 330–340.
- 181 A. Chu, J. Wang, Z. Tsai and C. Lee, *Sol. Energy Mater. Sol. Cells*, 2009, **93**, 1276–1280.
- 182 P. K. Basu, D. Sarangi, K. D. Shetty and M. B. Boreland, *Sol. Energy Mater. Sol. Cells*, 2013, **113**, 37–43.
- 183 K. Kim, S. Dhungel, S. Jung, D. Mangalaraj and J. Yi, *Sol. Energy Mater. Sol. Cells*, 2008, **92**, 960–968.
- 184 B. González-Díaz, R. Guerrero-Lemus, B. Díaz-Herrera, N. Marrero, J. Méndez-Ramos and D. Borchert, *Mater. Sci. Eng., B*, 2009, **159**, 295–298.
- 185 S. Zhong, B. Liu, Y. Xia, J. Liu, J. Liu, Z. Shen, Z. Xu and C. Li, *Energy Procedia*, 2012, **14**, 505–511.
- 186 Y. Yao, E. Brueckner, L. Li and R. Nuzzo, *Energy Environ. Sci.*, 2013, **6**, 3071–3079.
- 187 L. Chan, D. Kang, S.-M. Lee, W. Li, H. Hunter and J. Yoon, *Appl. Phys. Lett.*, 2014, **104**, 223905.
- 188 A. Ingenito, O. Isabella and M. Zeman, *ACS Photonics*, 2014, **1**, 270–278.
- 189 M. Kroll, T. Kšebier, M. Otto, R. Salzer, R. Wehrspohn, E.-B. Kley, A. Tünnermann and T. Pertsch, *Proceedings of Photonics for Solar Energy Systems III*, Brussels, 2010, p. 772505.
- 190 H. K. Raut, V. A. Ganesh, A. S. Nair and S. Ramakrishna, *Energy Environ. Sci.*, 2011, **4**, 3779–3804.
- 191 R. B. Stephens and G. D. Cody, *Thin Solid Films*, 1977, **45**, 19–29.
- 192 K.-H. Kim and Q.-H. Park, *Sci. Rep.*, 2013, **3**, 1062.
- 193 M.-L. Kuo, D. J. Poxson, Y. S. Kim, F. W. Mont, J. K. Kim, E. F. Schubert and S.-Y. Lin, *Opt. Lett.*, 2008, **33**, 2527–2529.
- 194 M. Chen, H.-c. Chang, A. S. P. Chang, S.-Y. Lin, J. Q. Xi and E. F. Schubert, *Appl. Opt.*, 2007, **46**, 6533–6538.
- 195 H. M. Branz, V. E. Yost, S. Ward, K. M. Jones, B. To and P. Stradins, *Appl. Phys. Lett.*, 2009, **94**, 231121.
- 196 P. Singh, S. N. Sharma and N. M. Ravindra, *JOM*, 2010, **62**, 15–24.
- 197 M.-J. Huang, C.-R. Yang, Y.-C. Chiou and R.-T. Lee, *Sol. Energy Mater. Sol. Cells*, 2008, **92**, 1352–1357.
- 198 W. Q. Xie, J. I. Oh and W. Z. Shen, *Nanotechnology*, 2011, **22**, 065704.
- 199 B. K. Nayak, V. V. Iyengar and M. C. Gupta, *Prog. Photovolt. Res. Appl.*, 2011, **19**, 631–639.
- 200 V. V. Iyengar, B. K. Nayak and M. C. Gupta, *Sol. Energy Mater. Sol. Cells*, 2010, **94**, 2251–2257.
- 201 V. V. Iyengar, B. K. Nayak, K. L. More, H. M. Meyer, M. D. Biegalski, J. V. Li and M. C. Gupta, *Sol. Energy Mater. Sol. Cells*, 2011, **95**, 2745–2751.
- 202 W.-C. Wang, C.-W. Lin, H.-J. Chen, C.-W. Chang, J.-J. Huang, M.-J. Yang, B. Tjahjono, J.-J. Huang, W.-C. Hsu and M.-J. Chen, *ACS Appl. Mater. Interfaces*, 2013, **5**, 9752–9759.
- 203 W. K. Huang, T.-S. Chen, C.-T. Tsai, M.-C. Kuo, K.-S. Chang, H.-M. Lin, Y.-K. Chiou, C.-C. Wang, M.-C. Lin and C.-S. Wu, *Energy Procedia*, 2011, **8**, 435–442.
- 204 Z. Shen, B. Liu, Y. Xia, J. Liu, J. Liu, S. Zhong and C. Li, *Scr. Mater.*, 2013, **68**, 199–202.
- 205 R. Martín-Palma, L. Vázquez, J. Martínez-Duart, M. Schnell and S. Schaefer, *Semicond. Sci. Technol.*, 2001, **16**, 657–661.
- 206 M. Ben Rabha and B. Bessaïs, *Sol. Energy*, 2010, **84**, 486–491.
- 207 Y. Liu, T. Lai, H. Li, Y. Wang, Z. Mei, H. Liang, Z. Li, F. Zhang, W. Wang, A. Y. Kuznetsov and X. Du, *Small*, 2012, **8**, 1392–1397.
- 208 Z. Zhao, B. Zhang, P. Li, W. Guo and A. Liu, *Int. J. Photoenergy*, 2014, **2014**, 683654.
- 209 W. C. Hsu, Y. S. Lu, J. Y. Chyan and J. A. Yeh, *Int. J. Photoenergy*, 2012, **2012**, 197514.
- 210 H.-C. Yuan, J. Oh, Y. Zhang, O. A. Kuznetsov, D. J. Flood and H. M. Branz, *Proceedings of the 38th IEEE Photovoltaic Specialists Conference*, Austin, 2012, pp. 686–689.
- 211 Y. Liu, A. Das, Z. Lin, I. B. Cooper, A. Rohatgi and C. P. Wong, *Nano Energy*, 2014, **3**, 127–133.
- 212 D. Z. Dimitrov and C.-H. Du, *Appl. Surf. Sci.*, 2013, **266**, 1–4.



- 213 L. Yang, Y. Liu, Y. Wang, X. Li, W. Chen, Y. Hua, Q. Zhang, J. Fu, H. Liang, Z. Mei and X. Du, *RSC Adv.*, 2014, **4**, 24458–24462.
- 214 K. Fuchsels, U. Schulz, N. Kaiser, T. Käsebier, E.-B. Kley and A. Tünnermann, *Proceedings of Photonics for Solar Energy Systems III*, Brussels, 2010, p. 772502.
- 215 J. Yoo, G. Yu and J. Yi, *Sol. Energy Mater. Sol. Cells*, 2011, **95**, 2–6.
- 216 P. Kwang Mook, L. Myoung Bok, J. Kyeong Su and C. Sie Young, *Jpn. J. Appl. Phys.*, 2013, **52**, 03BD01.
- 217 J. Liu, B. Liu, S. Liu, Z. Shen, C. Li and Y. Xia, *Surf. Coat. Technol.*, 2013, **229**, 165–167.
- 218 J.-M. Shim, H.-W. Lee, K.-Y. Cho, J.-K. Seo, J.-S. Kim, E.-J. Lee, J.-Y. Choi, D.-J. Oh, J.-E. Shin and J.-S. Kim, *Int. J. Photoenergy*, 2012, **2012**, 248182.
- 219 D. Suwito, U. Jager, J. Benick, S. Janz, M. Hermle and S. W. Glunz, *IEEE Trans. Electron Devices*, 2010, **57**, 2032–2036.
- 220 P. Repo, J. Benick, V. Vähänissi, J. Schön, G. von Gastrow, B. Steinhäuser, M. C. Schubert, M. Hermle and H. Savin, *Energy Procedia*, 2013, **38**, 866–871.
- 221 J. Liu, B. Liu, Z. Shen, S. Zhong, S. Liu, C. Li and Y. Xia, *Sol. Energy*, 2012, **86**, 3004–3008.
- 222 G. Xiao, B. Liu, J. Liu and Z. Xu, *Mater. Sci. Semicond. Process.*, 2014, **22**, 64–68.
- 223 M. Abbott and J. Cotter, *Prog. Photovolt. Res. Appl.*, 2006, **14**, 225–235.
- 224 W. F. Liu, J. M. Bian, Z. C. Zhao, Y. L. Luo, Z. Yuan, B. Y. Zhang and A. M. Liu, *ECS Solid State Lett.*, 2013, **2**, Q17–Q20.
- 225 S. Zhong, B. Liu, Y. Xia, J. Liu, J. Liu, Z. Shen, Z. Xu and C. Li, *Sol. Energy Mater. Sol. Cells*, 2013, **108**, 200–204.
- 226 C. H. Lin, D. Z. Dimitrov, C. H. Du and C. W. Lan, *Phys. Status Solidi C*, 2010, **7**, 2778–2784.
- 227 M. Algasinger, J. Paye, F. Werner, J. Schmidt, M. S. Brandt, M. Stutzmann and S. Koykov, *Adv. Energy Mater.*, 2013, **3**, 1068–1074.
- 228 M. Otto, M. Kroll, T. Kšebier, R. Salzer, A. Tünnermann and R. B. Wehrspohn, *Appl. Phys. Lett.*, 2012, **100**, 191603.
- 229 J. Ayre, <http://cleantechnica.com/2014/05/11/black-silicon-wafers-processed-solar-cells-actual-production-line-first-time/>, accessed June 30 2014.
- 230 Natcore Technology, <http://www.natcoresolar.com/news/natcores-black-silicon-technology-projected-to-slash-solar-cell-production-costs-by-23-5/>, accessed June 30 2014.
- 231 JA Solar Holdings Co., Ltd., <http://www.jasolar.com/webroot/company/activity.php?action=disp&newsid=295>, accessed June 30 2014.
- 232 D. Ponnampalam, [http://pv.energytrend.com/knowledge/Black\\_Silicon.html](http://pv.energytrend.com/knowledge/Black_Silicon.html), accessed June 30 2014.
- 233 D. M. Powell, M. T. Winkler, H. J. Choi, C. B. Simmons, D. B. Needleman and T. Buonassisi, *Energy Environ. Sci.*, 2012, **5**, 5874–5883.
- 234 H. Sai, Y. Kanamori, K. Arafune, Y. Ohshita and M. Yamaguchi, *Prog. Photovolt. Res. Appl.*, 2007, **15**, 415–423.
- 235 I. Moon, K. Kim, M. Thamilselvan, Y. Kim, K. Han, D. Kyeong, T. Kwon, D. Vinh Ai, J. Lee, M. Ju, K. Lee and J. Yi, *Sol. Energy Mater. Sol. Cells*, 2009, **93**, 846–850.
- 236 K. Fuchsels, M. Kroll, T. Kšebier, M. Otto, T. Pertsch, E. B. Kley, R. B. Wehrspohn, N. Kaiser and A. Tünnermann, *Proceedings of Photonics for Solar Energy Systems IV*, Brussels, 2012, p. 84380M.
- 237 J. Shewchun, J. Dubow, A. Myszkowski and R. Singh, *J. Appl. Phys.*, 1978, **49**, 855–864.
- 238 M. Otto, M. Kroll, T. Kšebier, S. M. Lee, M. Putkonen, R. Salzer, P. T. Miclea and R. B. Wehrspohn, *Adv. Mater.*, 2010, **22**, 5035–5038.
- 239 M. Steglich, A. Bingel, G. Jia and F. Falk, *Sol. Energy Mater. Sol. Cells*, 2012, **103**, 62–68.
- 240 M. Otto, M. Kroll, T. Kšebier, R. Salzer and R. B. Wehrspohn, *Energy Procedia*, 2012, **27**, 361–364.
- 241 K. M. Guenther, A. L. Baumann, T. Gimpel, S. Kontermann and W. Schade, *Energy Procedia*, 2012, **27**, 555–560.
- 242 S. Kontermann, T. Gimpel, A. L. Baumann, K. M. Guenther and W. Schade, *Energy Procedia*, 2012, **27**, 390–395.
- 243 M. Y. Ghannam, A. A. Abouelsaood, A. S. Alomar and J. Poortmans, *Sol. Energy Mater. Sol. Cells*, 2010, **94**, 850–856.
- 244 M. Grau, N.-T. Nguyen, A. Straboni and M. Lemi, *Energy Procedia*, 2011, **10**, 8–13.
- 245 C. S. Solanki, R. R. Bilyalov, J. Poortmans, J. Nijs and R. Mertens, *Sol. Energy Mater. Sol. Cells*, 2004, **83**, 101–113.
- 246 S. Kajari-Schröder, J. Käsiewieter, J. Hensen and R. Brendel, *Energy Procedia*, 2013, **38**, 919–925.
- 247 H. S. Radhakrishnan, M. Debucquoy, F. Korsós, K. Van Nieuwenhuysen, V. Depauw, I. Gordon, R. Mertens and J. Poortmans, *Energy Procedia*, 2013, **38**, 950–958.
- 248 H. S. Radhakrishnan, R. Martini, V. Depauw, K. Van Nieuwenhuysen, M. Debucquoy, J. Govaerts, I. Gordon, R. Mertens and J. Poortmans, *IEEE Journal of Photovoltaics*, 2014, **4**, 70–77.
- 249 E. V. Kerschaver and G. Beaucarne, *Prog. Photovolt. Res. Appl.*, 2006, **14**, 107–123.
- 250 Applied Nanotech Holdings, Inc., [http://www.appliednanotech.net/news/130103\\_Solexel\\_Achievement.php](http://www.appliednanotech.net/news/130103_Solexel_Achievement.php), accessed June 30 2014.
- 251 Solexel, Inc., <http://www.solexel.com/IntersolarNA2012.php>, accessed June 30 2014.
- 252 I. Gordon, F. Dross, V. Depauw, A. Masolin, Y. Qiu, J. Vaes, D. Van Gestel and J. Poortmans, *Sol. Energy Mater. Sol. Cells*, 2011, **95**(Suppl. 1), S2–S7.
- 253 H. Mei, C. Wang, J. Yao, Y. C. Chang, J. Cheng, Y. Zhu, S. Yin and C. Luo, *Opt. Commun.*, 2011, **284**, 1072–1075.
- 254 W. Wei, Y. Zhu, N. Wang, H. Mei and S. Yin, *Int. J. Thermophys.*, 2012, **33**, 2179–2184.
- 255 M. Hassen, A. Ben Jaballah, M. Hajji, N. Khedher, B. Bessais, H. Ezzaouia, H. Rahmouni, F. Rzigla Ouaja and A. Selmi, *Sol. Energy Mater. Sol. Cells*, 2005, **87**, 493–499.
- 256 N. Khedher, M. Hajji, M. Hassen, A. Ben Jaballah, B. Ouertani, H. Ezzaouia, B. Bessais, A. Selmi and R. Bennaceur, *Sol. Energy Mater. Sol. Cells*, 2005, **87**, 605–611.



- 257 H. Nouri, M. Bouaïcha and B. Bessaïs, *Sol. Energy Mater. Sol. Cells*, 2009, **93**, 1823–1826.
- 258 W. Dimassi, M. Bouaïcha, M. Kharroubi, M. Lajnef, H. Ezzaouia and B. Bessaïs, *Sol. Energy Mater. Sol. Cells*, 2008, **92**, 1421–1424.
- 259 H. S. Radhakrishnan, C. Ahn, J. Van Hoeymissen, F. Dross, N. Cowern, K. Van Nieuwenhuysen, I. Gordon, R. Mertens and J. Poortmans, *Phys. Status Solidi A*, 2012, **209**, 1866–1871.
- 260 H. S. Radhakrishnan, F. Dross, M. Debucquoy, P. Rosenits, K. Van Nieuwenhuysen, I. Gordon, J. Poortmans and R. Mertens, *Prog. Photovolt. Res. Appl.*, 2013.
- 261 M. A. Green, *Prog. Photovolt. Res. Appl.*, 2009, **17**, 183–189.
- 262 A. G. Aberle, *Sol. Energy Mater. Sol. Cells*, 2001, **65**, 239–248.
- 263 J. Schmidt, M. Kerr and A. Cuevas, *Semicond. Sci. Technol.*, 2001, **16**, 164.
- 264 G. Dingemans and E. Kessels, *J. Vac. Sci. Technol., A*, 2012, **30**, 040802.
- 265 B. Hoex, J. Gielis, M. Van de Sanden and W. Kessels, *J. Appl. Phys.*, 2008, **104**, 113703.
- 266 B. Hoex, S. Heil, E. Langereis, M. Van de Sanden and W. Kessels, *Appl. Phys. Lett.*, 2006, **89**, 042112.
- 267 J. Schmidt and M. Kerr, *Sol. Energy Mater. Sol. Cells*, 2001, **65**, 585–591.
- 268 M. J. Kerr and A. Cuevas, *Semicond. Sci. Technol.*, 2002, **17**, 166.
- 269 T. Lauinger, J. Schmidt, A. G. Aberle and R. Hezel, *Appl. Phys. Lett.*, 1996, **68**, 1232–1234.
- 270 B. Liu, S. Zhong, J. Liu, Y. Xia and C. Li, *Int. J. Photoenergy*, 2012, **2012**, 971093.
- 271 S. De Wolf and G. Beaucarne, *Appl. Phys. Lett.*, 2006, **88**, 022104.
- 272 J. Elmiger, R. Schieck and M. Kunst, *J. Vac. Sci. Technol., A*, 1997, **15**, 2418–2425.
- 273 S. Dauwe, J. Schmidt and R. Hezel, *Proceedings of the 29th IEEE Photovoltaic Specialists Conference*, New Orleans, 2002, pp. 1246–1249.
- 274 M. Taguchi, K. Kawamoto, S. Tsuge, T. Baba, H. Sakata, M. Morizane, K. Uchihashi, N. Nakamura, S. Kiyama and O. Oota, *Prog. Photovolt. Res. Appl.*, 2000, **8**, 503–514.
- 275 M. Garin, U. Rau, W. Brendle, I. Martin and R. Alcubilla, *J. Appl. Phys.*, 2005, **98**, 093711.
- 276 S. Olibet, E. Vallat-Sauvain and C. Ballif, *Phys. Rev. B: Condens. Matter Mater. Phys.*, 2007, **76**, 035326.
- 277 B. Stegemann, J. Kegel, M. Mews, E. Conrad, L. Korte, U. Stürzebecher and H. Angermann, *Energy Procedia*, 2013, **38**, 881–889.
- 278 H. Jin, K. Weber, N. Dang and W. Jellett, *Appl. Phys. Lett.*, 2007, **90**, 262109.
- 279 M. J. Kerr and A. Cuevas, *Semicond. Sci. Technol.*, 2002, **17**, 35.
- 280 J. Zhao, A. Wang, P. P. Altermatt, S. R. Wenham and M. A. Green, *Sol. Energy Mater. Sol. Cells*, 1996, **41**, 87–99.
- 281 B. Hoex, J. Schmidt, P. Pohl, M. Van de Sanden and W. Kessels, *J. Appl. Phys.*, 2008, **104**, 044903.
- 282 O. Schultz, S. Glunz and G. Willeke, *Prog. Photovolt. Res. Appl.*, 2004, **12**, 553–558.
- 283 M. B. Rabha, M. Salem, M. A. El Khakani, B. Bessais and M. Gaidi, *Mater. Sci. Eng., B*, 2013, **178**, 695–697.
- 284 V. Naumann, M. Otto, R. B. Wehrspohn and C. Hagendorf, *J. Vac. Sci. Technol., A*, 2012, **30**, 04D106.
- 285 G. Dingemans, W. Beyer, M. C. M. van de Sanden and W. M. M. Kessels, *Appl. Phys. Lett.*, 2010, **97**, 152106.
- 286 D. Lei, X. Yu, L. Song, X. Gu, G. Li and D. Yang, *Appl. Phys. Lett.*, 2011, **99**, 052103.
- 287 J. Schmidt, A. Merkle, R. Brendel, B. Hoex, M. v. de Sanden and W. Kessels, *Prog. Photovolt. Res. Appl.*, 2008, **16**, 461–466.
- 288 B. Hoex, J. Schmidt, R. Bock, P. Altermatt, M. Van de Sanden and W. Kessels, *Appl. Phys. Lett.*, 2007, **91**, 112107.
- 289 J. Benick, B. Hoex, M. Van de Sanden, W. Kessels, O. Schultz and S. W. Glunz, *Appl. Phys. Lett.*, 2008, **92**, 253504.
- 290 L. E. Black, T. Allen, K. R. McIntosh and A. Cuevas, *J. Appl. Phys.*, 2014, **115**, 093707.
- 291 B. Hoex, M. C. M. van de Sanden, J. Schmidt, R. Brendel and W. M. M. Kessels, *Phys. Status Solidi RRL*, 2012, **6**, 4–6.
- 292 L. Q. Zhu, Y. H. Liu, H. L. Zhang, H. Xiao and L. Q. Guo, *Appl. Surf. Sci.*, 2014, **288**, 430–434.
- 293 M. Otto, M. Kroll, T. Kšebier, J. Ziegler, A. N. Sprafke and R. B. Wehrspohn, *Energy Procedia*, 2013, **38**, 862–865.
- 294 P. Repo, A. Haarahiltunen, L. Sainiemi, M. Yli-Koski, H. Talvitie, M. C. Schubert and H. Savin, *IEEE Journal of Photovoltaics*, 2013, **3**, 90–94.
- 295 P. Repo, J. Benick, G. v. Gastrow, V. Vähänissi, F. D. Heinz, J. Schön, M. C. Schubert and H. Savin, *Phys. Status Solidi RRL*, 2013, **7**, 950–954.
- 296 G. Dingemans, M. Mandoc, S. Bordihn, M. Van de Sanden and W. Kessels, *Appl. Phys. Lett.*, 2011, **98**, 222102.
- 297 S. Duttagupta, F.-J. Ma, B. Hoex and A. G. Aberle, *Sol. Energy Mater. Sol. Cells*, 2014, **120**, 204–208.
- 298 L. E. Black and K. R. McIntosh, *IEEE Trans. Electron Devices*, 2010, **57**, 1996–2004.
- 299 S. Duttagupta, F. Lin, K. D. Shetty, A. G. Aberle and B. Hoex, *Prog. Photovolt. Res. Appl.*, 2013, **21**, 760–764.
- 300 J. Gjessing and E. S. Marstein, *Energy Procedia*, 2013, **38**, 348–354.
- 301 Y. Xiu, Y. Liu, D. W. Hess and C. Wong, *Nanotechnology*, 2010, **21**, 155705.
- 302 G. Sun, T. Gao, X. Zhao and H. Zhang, *J. Micromech. Microeng.*, 2010, **20**, 075028.
- 303 X. Zhang, Q. Di, F. Zhu, G. Sun and H. Zhang, *Micro Nano Lett.*, 2011, **6**, 947–950.
- 304 A. Y. Vorobyev and C. Guo, *Appl. Surf. Sci.*, 2011, **257**, 7291–7294.
- 305 K. X. Wang, Z. Yu, V. Liu, Y. Cui and S. Fan, *Nano Lett.*, 2012, **12**, 1616–1619.
- 306 J. Yoon, A. J. Baca, S.-I. Park, P. Elvikis, J. B. Geddes, L. Li, R. H. Kim, J. Xiao, S. Wang and T.-H. Kim, *Nat. Mater.*, 2008, **7**, 907–915.
- 307 A. J. Baca, K. J. Yu, J. Xiao, S. Wang, J. Yoon, J. H. Ryu, D. Stevenson, R. G. Nuzzo, A. A. Rockett and Y. Huang, *Energy Environ. Sci.*, 2010, **3**, 208–211.





- 308 J. Yoon, L. Li, A. V. Semichaevsky, J. H. Ryu, H. T. Johnson, R. G. Nuzzo and J. A. Rogers, *Nat. Commun.*, 2011, **2**, 343.
- 309 A. Mavrokefalos, S. E. Han, S. Yerci, M. S. Branham and G. Chen, *Nano Lett.*, 2012, **12**, 2792–2796.
- 310 R. Woehl, J. Krause, F. Granek and D. Biro, *IEEE Electron Device Lett.*, 2011, **32**, 345–347.
- 311 P. J. Cousins, D. D. Smith, L. Hsin-Chiao, J. Manning, T. D. Dennis, A. Waldhauer, K. E. Wilson, G. Harley and W. P. Mulligan, *Proceedings of the 35th Photovoltaic Specialists Conference*, Honolulu, 2010, pp. 000275–000278.
- 312 C. Gong, E. Van Kerschaver, J. Robbelein, T. Janssens, N. Posthuma, J. Poortmans and R. Mertens, *IEEE Electron Device Lett.*, 2010, **31**, 576–578.
- 313 R. Bock, S. Mau, J. Schmidt and R. Brendel, *Appl. Phys. Lett.*, 2010, **96**, 263507.
- 314 S. Jeong, M. D. McGehee and Y. Cui, *Nat. Commun.*, 2013, **4**, 3950.
- 315 F. Granek, M. Hermle, D. M. Huljić, O. Schultz-Wittmann and S. W. Glunz, *Prog. Photovolt. Res. Appl.*, 2009, **17**, 47–56.
- 316 M. Hermle, F. Granek, O. Schultz and S. W. Glunz, *J. Appl. Phys.*, 2008, **103**, 054507.
- 317 F. Granek and C. Reichel, *Sol. Energy Mater. Sol. Cells*, 2010, **94**, 1734–1740.
- 318 C. Trompoukis, O. El Daif, V. Depauw, I. Gordon and J. Poortmans, *Appl. Phys. Lett.*, 2012, **101**, 103901.
- 319 M. Peters, M. Rüdiger, H. Hauser, M. Hermle and B. Bläsi, *Prog. Photovolt. Res. Appl.*, 2012, **20**, 862–873.
- 320 X. Meng, V. Depauw, G. Gomard, O. El Daif, C. Trompoukis, E. Drouard, C. Jamois, A. Fave, F. Dross, I. Gordon and C. Seassal, *Opt. Express*, 2012, **20**, A465–A475.
- 321 S. B. Mallick, M. Agrawal and P. Peumans, *Opt. Express*, 2010, **18**, 5691–5706.
- 322 A. Bozzola, M. Liscidini and L. C. Andreani, *Prog. Photovolt. Res. Appl.*, 2013, DOI: 10.1002/pip.2385.

